Doctoral Dissertation

Imidazolium based and pyrrolidinium based poly(ionic liquid) binders for hard carbon anode in sodium ion secondary batteries

Zhang Yuanhao

Supervisor: Noriyoshi Matsumi

Graduate School of Advanced Science and Technology

Japan Advanced Institute of Science and Technology

Materials Science

March 2026

Imidazolium based and pyrrolidinium based poly(ionic liquid) binders for hard carbon anode in sodium ion secondary batteries

This study systematically evaluated the electrochemical performance of 3 poly(ionic liquid) binders—PEVIFSI, PDADMAFSI, and PDADMATFSI with PVDF as control in sodium-ion batteries (SIBs) with hard carbon anodes. Figure 1 shows the synthesis routine of these binders, among them, PEVITFSI has low glass transformation temperature and exhibits viscoelasticity at room temperature, therefore excluded as a candidate for binder.

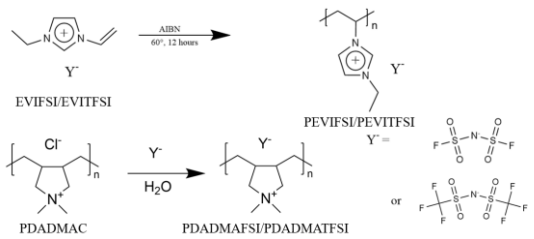

Figure 1 Synthesis routine of PEVIFSI, PEVITFSI, PDADMAFSI, PDADMATFSI binders

Figure 2 and Table 1 shows the result of Cyclic voltammetry (CV) test and overpotential. In CV test, PDADMAFSI and PDADMATFSI binders exhibited lower overpotentials (0.1402 V and 0.1367 V) and lower desodiation potentials compared to PVDF and PEVIFSI. Figure 3 shows the result of long cycle study, in half-cells using hard carbon anodes and assembled with PDADMATFSI as the binder, superior cycling stability and higher capacity retention (80.9%) were observed at a current density of 50 mA/g, compared to 77.8% for PVDF. PDADMAFSI also exhibited excellent cycling stability, though with a slightly lower capacity retention (67.7%).

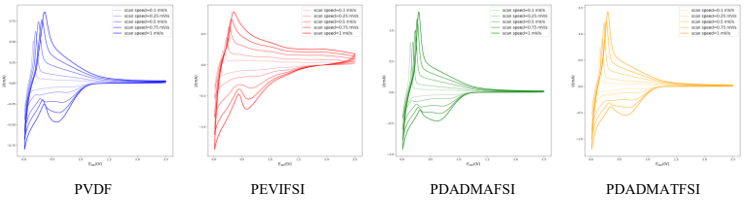

Figure 2 Cyclic voltammetry (CV) test of hard carbon based half cell (sodium ion battery) fabricated by using different binders

Scan speed	PVDF	PEVIFSI	PDADMAFSI	PDADMATFSI
0.1	0.169	0.163	0.1488	0.1563
0.25	0.2056	0.2197	0.1855	0.1929
0.5	0.2556	0.2696	0.2322	0.2263
0.75	0.3023	0.3129	0.2624	0.2596
1	0.3559	0.3462	0.289	0.293
overpotential	0.1869	0.1832	0.1402	0.1367

Table 1 overpotential of all half cell fabricated by different binders

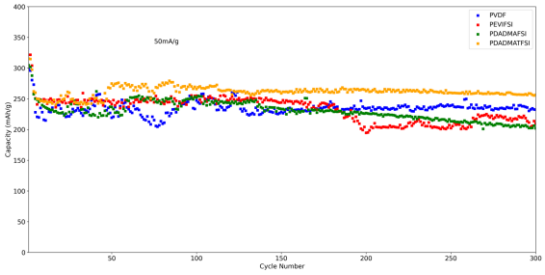

Figure 3 long cycle study of all half cell fabricated by using different binders

These binders also significantly reduced the solid electrolyte interphase (SEI) impedance, In Electrochemical Impedence Spectra(EIS) test and the simulation based on equivalent circuit, we found the SEI impedance shows values of 0.9147 Ω for PDADMAFSI, 0.4668 Ω for PDADMATFSI, and 4.564 Ω for PVDF. These results highlight the advantages of PDADMATFSI binder in sodium-ion batteries, showcasing their potential for improving electrochemical performance through enhanced stability and reduced resistance. Additionally, half-cells assembled with PEVIFSI as the binder exhibited significantly higher solid electrolyte interphase impedance after cycling, with a value of 13.07 Ω, compared to other binders.

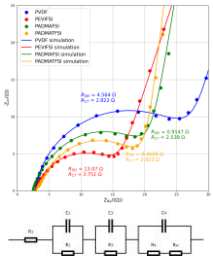

Figure 4 Electrochemical Impedence Spectra of hard carbon based half-cells with different binders after cycling and its equivalent simulation circuit

Morphological analysis via SEM further corroborated these findings. Figure 5 shows the image of the electrode surface before and after 300 cycle. The electrodes with PEVIFSI exhibited grooves and voids after cycling, confirming degradation, while the other binders maintained more uniform electrode surfaces.

In conclusion, PDADMA cation based binders, especially PDADMATFSI binder outperformed other binders in terms of electrochemical stability, cycling performance, and SEI properties, making it promising candidates for SIB applications. The poor performance of PEVIFSI highlights the limitations of imidazolium-based ionic liquid binders due to solubility issues and SEI instability.

Chapter 1 provides a comprehensive overview of sodium-ion batteries (SIBs) and their binder systems, highlighting their critical

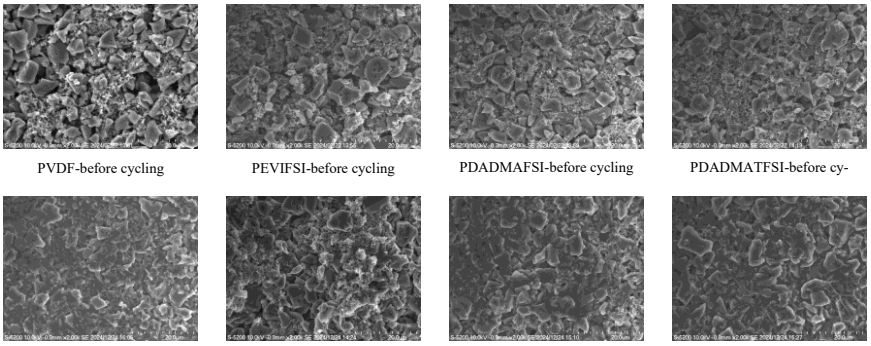

Figure 5 SEM image before and after cycling of the hard carbon half-cell fabricated by using PVDF, PEVIFSI, PDADMAFSI, PDADMATFSI as binder respectively.

roles in determining the electrochemical performance of SIBs. Chapter 2 introduces the synthesis and characterization of newly developed pyrrolidinium-based binders-PDADMAFSI and PDADMATFSI. Chapter 3 presents a detailed analysis of imidazolium-based binders-PEVIFSI and pyrrolidinium-based binders-PDADMAFSI and PDADMATFSI, chapter 4 is the conclusion.

Keywords: Sodium ion battery, hard carbon anode, poly(ionic liquids), binder, ion exchange

Preface

This dissertation reports the doctoral research I conducted from 2022 to 2025 at the Graduate School of Advanced Science and Technology, Japan Advanced Institute of Science and Technology (JAIST), under the supervision of Professor Noriyoshi Matsumi. The research focuses on the development of high-performance polymer binders for hard carbon anodes in sodium-ion batteries (SIBs), aiming to overcome the limitations of the conventional poly(vinylidene fluoride) (PVDF) binder in terms of electrochemical stability and electrode integrity.

In this work, poly(ionic liquid)s (PILs) were explored as alternative binders, with two types of PILs synthesized: an imidazolium-based PIL, poly(1-ethyl-3-vinylimidazolium bis(fluorosulfonyl)imide) (PEVIFSI), prepared by radical polymerization, and two pyrrolidinium-based PILs, Poly(diallyldimethylammonium bis(fluorosulfonyl)imide) (PDADMAFSI) and poly(diallyldimethylammonium bis(trifluoromethanesulfonyl)imide) (PDADMATFSI), synthesized via ion exchange.

The results demonstrate that the pyrrolidinium-based PDADMATFSI binder significantly outperforms both conventional PVDF and the imidazolium-based PEVIFSI in terms of cycling stability, rate performance, and charge transfer resistance. PDADMATFSI exhibited excellent electrochemical stability, better interaction with active materials and conductive additives, and facilitated uniform slurry coating and robust electrode architecture. In contrast, PEVIFSI underwent severe degradation due to its lower LUMO level during electrochemical reactions, resulting in uncontrolled SEI growth and rapid capacity fading.

Furthermore, It was discovered that during electrochemical cycling, the TFSI anions in PDADMATFSI participated in an ion exchange process with Cl^- generated from the decomposition of $NaClO_4$ in the electrolyte, contributing to the formation of a more stable SEI film.

This study not only confirms the great potential of pyrrolidinium-based PILs as novel binders for SIBs, but also highlights the limitations of imidazolium-based PILs in anode applications. The findings provide new insights into the design of next-generation high-performance binders for batteries and deepen the understanding of polymer–electrode interfacial interactions.

Zhang Yuanhao

Graduate School of Advanced Science and Technology

Japan Advanced Institute of Science and Technology

March 2024.

Acknowledgements

The research presented in this thesis was carried out under the supervision of Professor Noriyoshi Matsumi at the Graduate School of Advanced Science and Technology, Japan Advanced Institute of Science and Technology (JAIST), during the period from 2022 to 2025. The author expresses sincere gratitude to Prof. Matsumi for his constant support, insightful guidance, and encouragement throughout this academic journey.

During the course of this work at JAIST, the author also gratefully acknowledges Associate Professor Bharat Srimitra Mantripragada for his motivation, constructive suggestions, and continuous encouragement, which were instrumental in shaping the progress of this research.

The author further extends heartfelt thanks to all former and current members of the Matsumi Laboratory, whose collaboration, technical assistance, and stimulating scientific discussions greatly enriched this work and created a supportive research environment.

Finally, the author wishes to thank his parents, family, friends, and mentors for their unwavering emotional and intellectual support, which provided the foundation for perseverance and success throughout this academic pursuit.

contents

Chapter 1 Introduction

1.1 Overview of Battery Development

The development of battery technology has undergone a long evolution, from the earliest chemical batteries to modern high-energy-density lithium-ion batteries. Each technological advancement has revolutionized energy storage and application. This section reviews the history of battery development, focusing on the transition from lead-acid batteries to modern batteries and the rise of lithium-ion batteries.

1.1.1 Early Battery Technologies

The earliest known battery dates back to the Baghdad Battery (as shown in Figure 1), an ancient artifact whose purpose remains debated. However, it suggests early human exploration of electrical energy. In the late 18th century, Italian scientist Alessandro Volta invented the Voltaic Pile, the first device capable of continuously supplying an electric current, marking the beginning of modern battery technology.

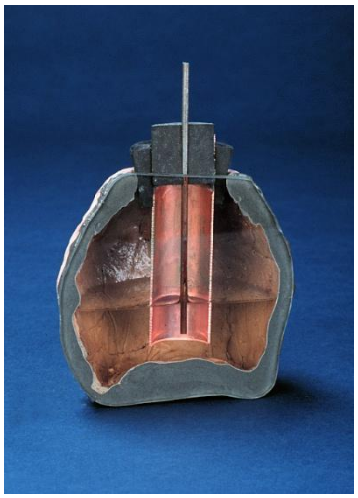

Figure 1. Battery, Baghdad, 250 BCE

by Dennielle Downs

As battery research progressed, the mid-19th century saw significant developments by scientists such as Hans Christian Ørsted and Michael Faraday, who contributed to the advancement of electrochemical theory. French chemist Georges Leclanché invented the Leclanché cell in 1866, a wet cell that was simple and cost-effective, serving as the precursor to modern dry batteries.

1.1.2 Evolution from Lead-Acid to Modern Batteries

The invention of the lead-acid battery in the late 19th century marked the advent of rechargeable batteries. As, shown in Figure 2[1], in 1859, French physicist Gaston

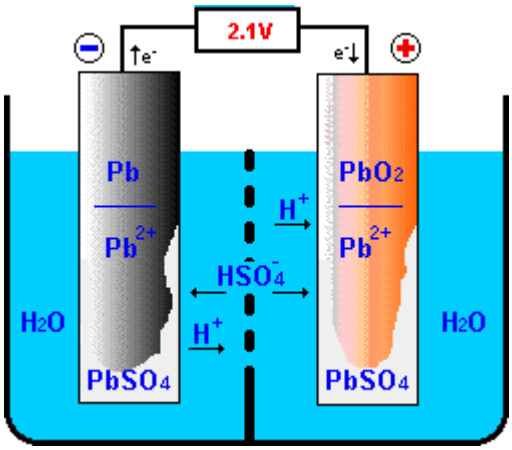

Figure 2. Schematic diagram of lead-acid battery

Planté developed the first rechargeable lead-acid battery, which became widely used in automobile starter batteries, uninterruptible power supplies (UPS), and energy storage systems due to its low cost and long cycle life.

In the 20th century, nickel-cadmium (Ni-Cd) and nickel-metal hydride (Ni-MH) batteries emerged. Ni-Cd batteries gained popularity due to their excellent charge-discharge performance, but environmental concerns over toxic cadmium led to the development of more eco-friendly alternatives. Ni-MH batteries improved energy density while reducing environmental impact.

1.1.3 The Rise of Lithium-Ion Batteries

The development of lithium-ion batteries (LIBs) began in the 1970s. Lithium metal was considered an ideal battery material due to its high energy density and low weight. However, early lithium-metal batteries faced safety issues, such as dendrite formation leading to short circuits.

In the 1980s, John B. Goodenough and his team introduced lithium cobalt oxide ($LiCoO_2$) as a cathode material, enhancing battery safety and energy density. In 1991, Sony successfully commercialized the lithium-ion battery, marking a significant milestone in battery technology.

Compared to traditional batteries, lithium-ion batteries offer high energy density, long cycle life, and low self-discharge rates. As a result, they quickly became dominant in consumer electronics, electric vehicles, and energy storage systems. Recent advancements in cathode materials, such as lithium iron phosphate ($LiFePO_4$) and nickel-cobalt-manganese (NCM/NCA), have further improved battery safety and performance, solidifying lithium-ion technology as the mainstream choice.

1.2 Introduction to Lithium-Ion Batteries (LIBs)

Lithium-ion batteries (LIBs) have become the dominant energy storage technology in modern applications, ranging from portable electronics to electric vehicles and grid-scale energy storage. Their high energy density, lightweight design, and rechargeable capabilities have revolutionized power sources for numerous industries. This section explores the working principles, advantages, limitations, and sustainability challenges associated with LIBs.

1.2.1 Working Principles of LIBs

A lithium-ion battery consists of a cathode, an anode, an electrolyte, and a separator. During discharge, lithium ions move from the anode (typically graphite) to the cathode (such as $LiCoO_2$, NMC, or LFP) through the electrolyte, while electrons flow through an external circuit to provide power. The process is reversed during charging, as lithium ions migrate back to the anode.

Figure 3 shows the fundamental reaction mechanism of a LFP-type lithium ion battery, which is based on intercalation, where lithium ions are stored within the structures of the electrode materials rather than undergoing chemical decomposition. This reversible process enables LIBs to achieve high efficiency and long cycle life compared to older battery technologies.

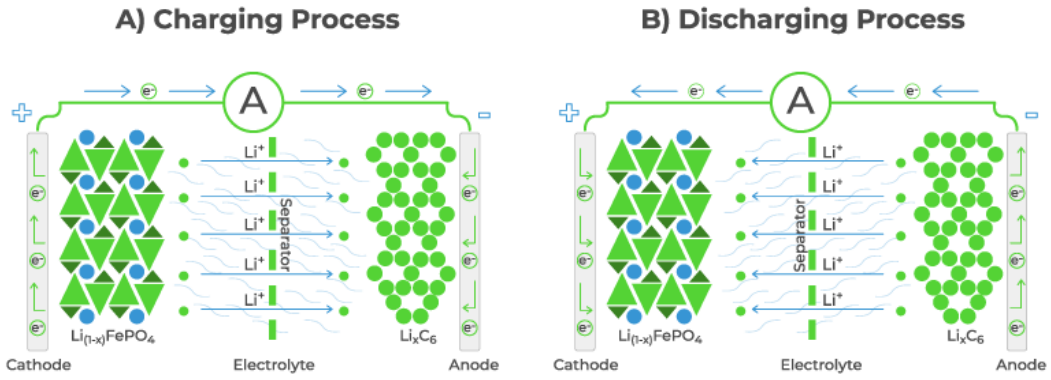

Figure 3. Schematic diagram of LFP-type lithium-ion battery

1.2.2 Advantages and Limitations of LIBs

Figure 4 provides the comparison of 6 major type of lithium-ion battery, lithium-ion batteries offer several advantages over traditional battery chemistries. They provide a significantly higher energy density, making them ideal for compact and

lightweight applications. Their long cycle life allows them to withstand hundreds to thousands of charge-discharge cycles with minimal capacity degradation. Additionally, LIBs have a low self-discharge rate, enabling them to retain charge longer than many other rechargeable batteries. They also support fast charging without significantly impacting longevity and do not suffer from the memory effect, which was a drawback of nickel-cadmium batteries.

Despite these advantages, lithium-ion batteries have some limitations. Safety concerns remain a significant issue, as they are susceptible to thermal runaway, which can lead to overheating, fire, or explosion if not properly managed. The high cost of production, driven by expensive raw materials such as lithium, cobalt, and nickel, also poses challenges. Furthermore, the limited availability of these materials raises concerns about supply chain stability and environmental impact. Improper disposal and mining practices associated with LIB production can contribute to ecological degradation, making sustainability an ongoing challenge for the industry.

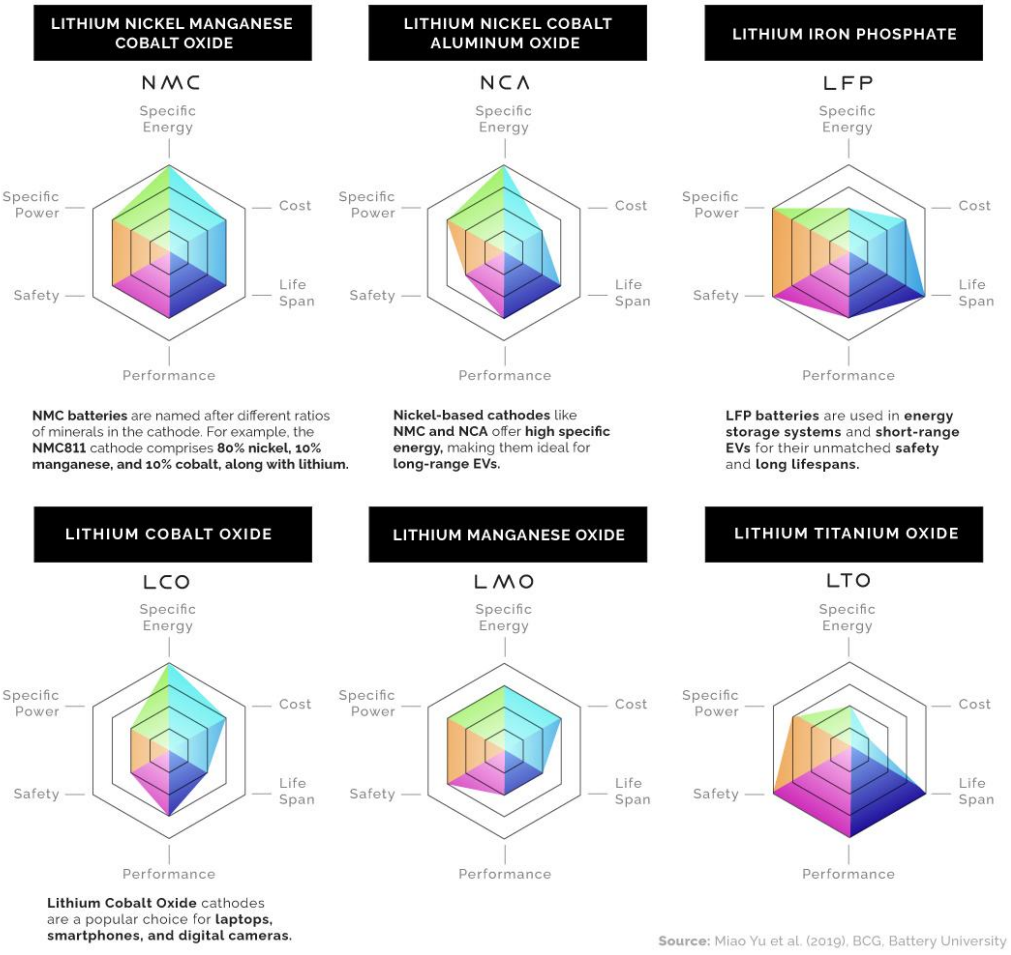

Figure 4. Comparison of six major types of Lithium-ion Batteries

1.2.3 Sustainability and Resource Challenges

The increasing demand for lithium-ion batteries raises concerns regarding sustainability and resource availability. The extraction of key raw materials such as lithium, cobalt, and nickel requires substantial energy and water consumption, often leading to environmental degradation and ethical concerns regarding labor practices. Addressing these issues necessitates the development of efficient recycling technologies to recover valuable materials and minimize waste. Additionally, second-life applications, such as repurposing used EV batteries for grid storage, can extend battery lifespan and reduce environmental impact. Research into alternative battery chemistries, such as sodium-ion and solid-state batteries, aims to mitigate dependence on scarce and costly materials while enhancing performance and safety. Moreover, effective policies and regulations are crucial for establishing sustainable supply chains, promoting ethical mining practices, and encouraging battery recycling programs. By integrating these solutions, the long-term sustainability of lithium-ion battery technology can be ensured while minimizing environmental and social challenges.

1.3 The Emergence of Sodium-Ion Batteries (SIBs)

Sodium-ion batteries (SIBs) have garnered significant attention as a promising alternative to lithium-ion batteries (LIBs) in recent years. Although LIBs dominate the current market, there is a growing interest in SIBs due to the abundance of sodium, lower material costs, and the potential for sustainable large-scale energy storage applications. This section details the factors driving the emergence of SIBs, compares them with LIBs, and explores the challenges and opportunities that lie ahead for this technology.

1.3.1 Advantage of sodium ion battery

One of the primary reasons for the surge in interest in sodium-ion batteries is the abundance of sodium in the Earth’s crust. Unlike lithium, which is relatively scarce and concentrated in specific geographic regions, sodium is widely distributed and can be extracted from seawater, salt lakes, and various minerals. This plentiful supply not only makes sodium more accessible but also results in considerably lower raw material costs.

Figure 5 shows the cost prediction of sodium ion battery compared with other type of battery, economically, the use of sodium could drastically reduce the overall cost of battery production. Since battery manufacturing is sensitive to raw material costs, a transition to sodium-based systems could lead to more affordable energy storage solutions. This is especially important for applications that require large-scale deployment, such as grid storage for renewable energy integration, where the cost per kilowatt-hour is a critical metric.

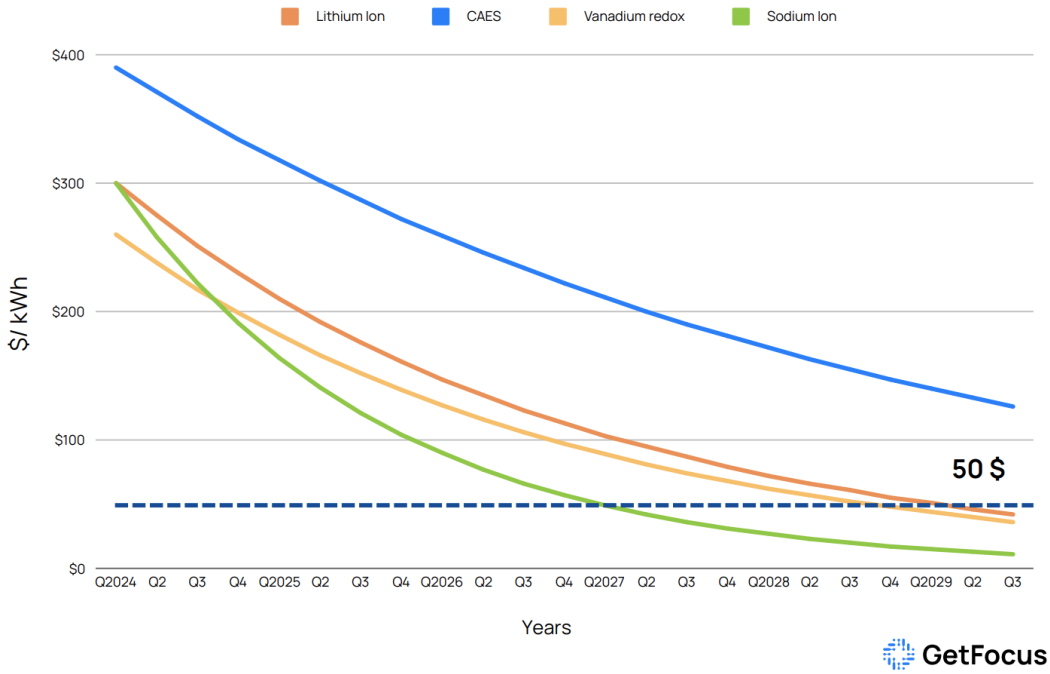

Figure 5. Cost predication of sodium ion battery compared with other battery.

Furthermore, sodium extraction and processing involve mature technologies that are well understood in the chemical and metallurgical industries. The existing infrastructure for salt processing can be leveraged to support the production of SIBs, thereby lowering the technological barrier for commercialization. While sodium-ion technology is still in the developmental stage compared to the highly optimized LIB systems, its potential for low-cost manufacturing makes it a promising candidate for future energy storage applications.

Recent studies have highlighted the strategic importance of diversifying battery chemistries, not only to meet the increasing demand for energy storage but also to mitigate supply chain risks associated with critical materials. By incorporating sodium into battery designs, industries and governments can reduce dependence on scarce resources and buffer against geopolitical supply uncertainties. Moreover, the environmental footprint of sodium extraction is generally lower than that of lithium mining, providing an additional incentive to develop SIBs under sustainable frameworks.

1.3.2 Comparisons Between LIBs and SIBs

When comparing sodium-ion batteries to their lithium-ion counterparts, several key differences become apparent. LIBs have long been favored due to their high energy density, excellent cycle life, and mature technology base. However, SIBs offer a unique set of characteristics that make them competitive in certain applications, especially where cost and sustainability are paramount.

Energy Density and Voltage: Lithium-ion batteries are renowned for their high energy density, typically ranging from 150 to 250 Wh/kg, which makes them ideal for portable electronics and electric vehicles. In contrast, SIBs generally exhibit a lower energy density. The larger ionic radius of sodium compared to lithium leads to less efficient packing in electrode materials, which reduces the theoretical capacity and operating voltage of SIBs. Despite this inherent limitation, ongoing research into new cathode and anode materials is gradually closing the performance gap between LIBs and SIBs.

Cycle Life and Stability: LIBs are well-known for their long cycle life, with many commercial systems achieving several thousand cycles before significant degradation occurs. SIBs, on the other hand, have historically suffered from shorter cycle life due to issues such as electrode instability and larger volume changes during charge/discharge cycles. However, advancements in material science and cell engineering have significantly improved the cyclability and long-term stability of SIBs. Novel electrode architectures and electrolyte formulations are being developed to mitigate the adverse effects of sodium's larger ionic size, thereby enhancing the durability of SIB systems.

Cost and Material Availability: One of the most compelling advantages of SIBs is their cost-effectiveness. The raw materials for sodium-ion batteries are inexpensive and widely available, which could translate into lower manufacturing costs. While the performance metrics of SIBs have not yet reached the level of state-of-the-art LIBs, the cost benefit could be decisive for large-scale and stationary applications where energy density is a secondary concern. Furthermore, by reducing reliance on critical materials such as cobalt and nickel, SIBs offer a more sustainable and geopolitically stable alternative for energy storage.

Environmental Impact and Sustainability: Environmental sustainability is becoming a critical factor in battery technology selection. The mining and processing of lithium and cobalt have raised significant environmental and ethical concerns.

Sodium, being abundant and less environmentally damaging to extract, presents a more sustainable option. Additionally, the potential for recycling and reusing sodium-based materials is promising, given the existing knowledge base in salt and chemical processing industries. Therefore, while LIBs currently offer superior performance for mobile applications, SIBs could be more advantageous for stationary storage where long-term environmental and economic considerations are paramount.

Application Suitability: Due to their lower energy density, sodium-ion batteries may not immediately replace LIBs in high-energy-demand applications such as electric vehicles. However, for grid storage, load leveling, and backup power systems, the cost-effectiveness and abundant material supply make SIBs an attractive option. The lower energy density is less critical in stationary applications where weight and size are less of a concern compared to cost and sustainability. In addition, the ability to operate at a wide range of temperatures makes SIBs suitable for environments where LIB performance might be compromised.

In summary, while lithium-ion batteries remain the standard in high-performance, portable applications, sodium-ion batteries offer unique advantages in terms of cost, resource availability, and environmental impact. These factors are driving significant research and development efforts aimed at overcoming the technical challenges of SIBs and unlocking their full potential for a broad range of energy storage applications.

1.3.3 Challenges and Opportunities for SIBs

Despite their promising attributes, sodium-ion batteries face several technical and commercial challenges that must be addressed before they can achieve widespread adoption. The primary technical challenges include improving energy density, enhancing cycle life, and developing robust electrode materials that can accommodate the larger sodium ions. Researchers are actively investigating new cathode materials—such as layered oxides, polyanionic compounds, and Prussian Blue analogues—as well as advanced anode materials that can better tolerate volume changes and maintain structural integrity over many cycles.

The formation of a stable solid electrolyte interphase (SEI) is another critical challenge for SIBs. In lithium-ion batteries, the SEI plays a crucial role in protecting the electrodes and ensuring long-term stability. However, the chemistry of sodium-based SEI formation is different, and achieving a stable and ionically conductive SEI on both the cathode and anode surfaces remains a key research focus. The

development of advanced electrolyte formulations and additives is essential to enhance the SEI stability and improve the overall safety of SIB systems.

From a commercialization perspective, scaling up sodium-ion battery production involves overcoming hurdles related to manufacturing processes and quality control. Current laboratory-scale prototypes must be translated into large-scale production lines without compromising performance or reliability. This scaling challenge is compounded by the need to establish standardized testing and certification protocols for SIBs, which are still in the early stages of development compared to LIBs.

On the opportunity side, the emergence of SIBs opens up new markets, particularly in areas where the cost and environmental impact of LIBs are prohibitive. For instance, large-scale grid storage systems and renewable energy integration projects stand to benefit from the lower cost and abundant supply of sodium-based systems. Additionally, SIBs could play a pivotal role in off-grid and remote energy applications, where local availability of raw materials and ease of recycling are significant advantages.

There is also a growing interest in hybrid systems that combine the best features of different battery chemistries. For example, research into dual-ion systems that integrate both sodium and lithium components is underway, aiming to leverage the high energy density of LIBs with the cost advantages of SIBs. Such hybrid systems could provide a transitional technology that addresses current limitations while paving the way for future advancements.

Government policies and industry collaborations are increasingly focusing on diversifying battery technologies to enhance energy security and promote sustainability. Incentives for research into alternative chemistries, such as sodium-ion batteries, are being introduced worldwide. These initiatives are expected to accelerate innovation, reduce costs through economies of scale, and ultimately make SIBs a competitive option in the global energy storage market.

The emergence of sodium-ion batteries represents a significant opportunity to diversify energy storage technologies and address critical issues of cost, material availability, and environmental sustainability. While technical challenges remain, ongoing research and collaborative efforts are steadily advancing the performance of SIBs, positioning them as a viable alternative to lithium-ion systems in various applications. With continued investment and innovation, sodium-ion batteries could become a cornerstone of future energy storage solutions, especially in large-scale and stationary applications.

1.4 Key Components of Sodium-Ion Batteries

The performance, safety, and longevity of sodium-ion batteries are determined by the careful design and integration of several key components. Each component, from the electrode materials to the binders, electrolytes, and additives, plays a vital role in the overall behavior of the battery system. In this section, detailed analysis of the primary components that constitute a sodium-ion battery is provided, discussing the current state of research, material properties, and the challenges and opportunities for each component.

1.4.1 Cathode Materials

The cathode is a critical component in sodium-ion batteries, as it largely determines the battery's voltage, capacity, and cycle life. Researchers have focused on several classes of cathode materials, each with its unique structural and electrochemical properties.

Layered Oxides

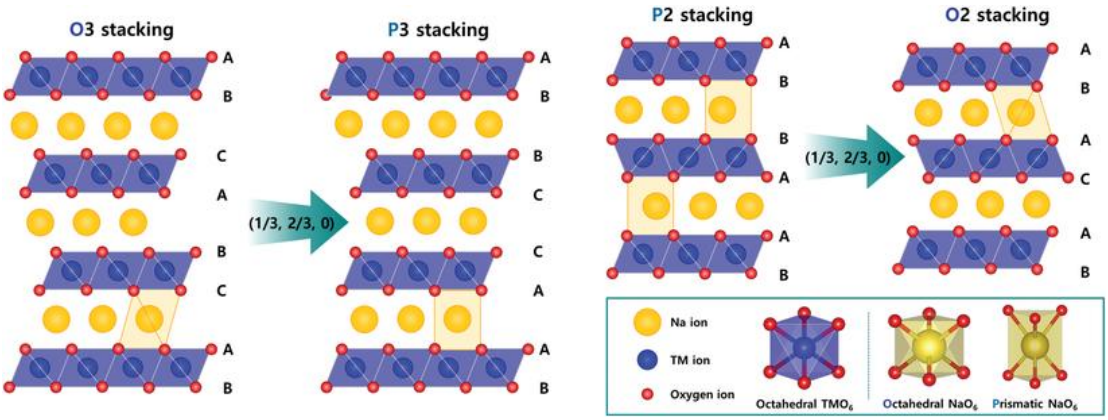

Figure 6. Schematic representation showing the classification of sodium layered oxide.

As shown in Figure 6[2], layered oxide cathodes, such as sodium manganese oxide (Na_xMnO_2) and sodium nickel manganese cobalt oxide (NaNMC), have attracted significant attention due to their high energy density and favorable electrochemical performance. These materials typically possess a layered structure that facilitates the intercalation and deintercalation of sodium ions. The layered arrangement allows for relatively fast ion transport and can be optimized by adjusting the transition metal composition to balance capacity, stability, and cost. Challenges with layered oxides

include phase transitions during cycling, which can lead to capacity fading, and sensitivity to moisture and atmospheric exposure during synthesis and processing. Advanced synthesis techniques, such as sol–gel methods and controlled thermal treatments, are being explored to improve the crystallinity and stability of layered oxides.

Polyanionic Compounds

Polyanionic cathodes incorporate structural units such as phosphate, sulfate, or silicate groups into their framework. Examples include sodium iron phosphate ($NaFePO_4$) and sodium vanadium phosphate $(Na_3V_2(PO_4)_3)^3$ (as shown in Figure 7). The presence of strongly bonded anionic groups in the crystal lattice imparts excellent thermal and chemical stability. This enhanced stability is beneficial for high-temperature applications and contributes to a longer cycle life. Although polyanionic compounds typically offer lower theoretical capacities compared to layered oxides, their stability and safety profile make them attractive for stationary and grid-scale energy storage. Moreover, the ability to fine-tune the redox potential through chemical substitution provides an avenue to optimize both capacity and operating voltage.

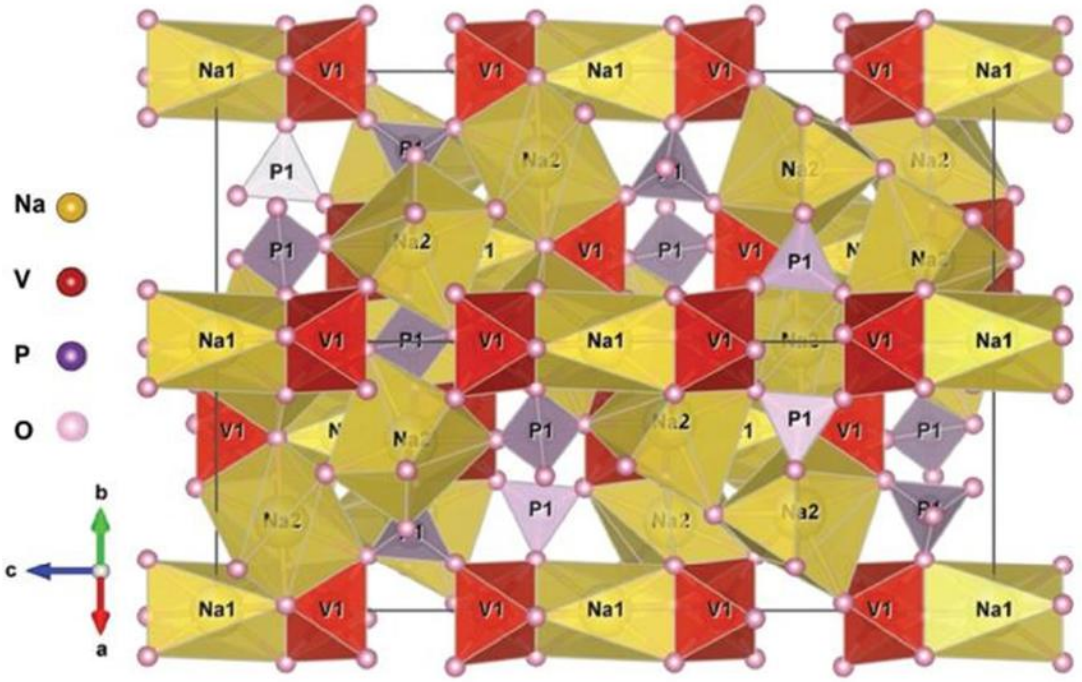

Figure 7. Structure scheme of $Na_3V_2(PO_4)_3$.

Prussian Blue Analogues

As shown in Figure 8, Prussian Blue analogues (PBAs) are a class of open-

framework compounds characterized by a three-dimensional structure and the presence of cyanide bridges between metal centers.[4] PBAs, such as sodium iron hexacyanoferrate, offer several advantages, including high ionic conductivity, facile synthesis from aqueous solutions, and inherent structural stability. The open-framework structure not only provides abundant interstitial sites for sodium ion storage but also allows for rapid ion diffusion, making PBAs promising candidates for high-power applications. However, PBAs can be sensitive to structural defects and water content, which may affect their long-term cycling performance. Ongoing research focuses on improving the material's stoichiometry and reducing the presence of vacancies to enhance its electrochemical stability.

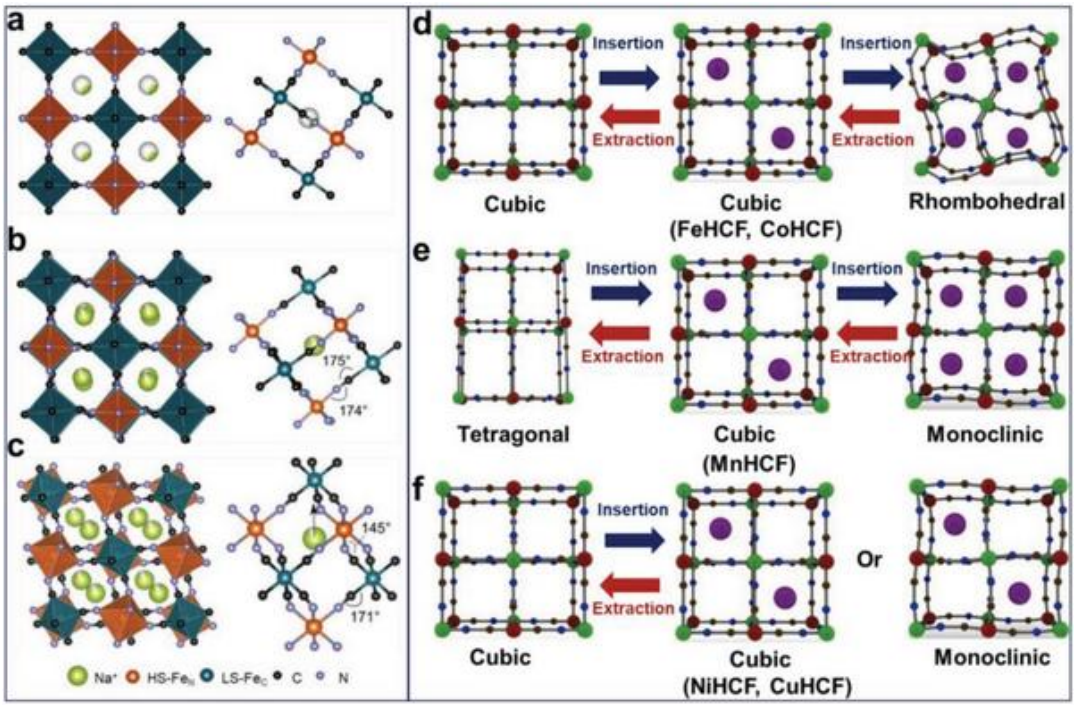

Figure 8. Local structures of PB with a) cubic, b) monoclinic, and c) rhombohedral phase. Structure evolution of d) FeHCF and CoHCF, e) MnHCF, and f) CuHCF and NiHCF induced by guest cations insertion/extraction.

1.4.2 Anode Materials

The anode in a sodium-ion battery must accommodate the insertion and extraction of sodium ions while maintaining structural integrity and electrical conductivity over many cycles. A variety of anode materials are under investigation to meet these demands.

Carbon-Based Materials

Carbon-based anodes, particularly hard carbon, have emerged as the most promising candidates for sodium-ion batteries. Hard carbon is characterized by its disordered structure, which creates numerous defects and microvoids that can serve as active sites for sodium ion storage.[5] Figure 9 shows the different mechanisms of sodium storage in hard carbon, this structure allows for a relatively high sodium storage capacity despite the larger ionic radius of sodium compared to lithium. Researchers have also investigated soft carbon and other graphitic materials, though these tend to offer lower capacities due to their more ordered structures, which are less accommodating for sodium ions. Advances in synthesis and structural modification of carbon materials, such as doping with heteroatoms (e.g., nitrogen or sulfur), have further improved the storage capabilities and conductivity of these anodes.

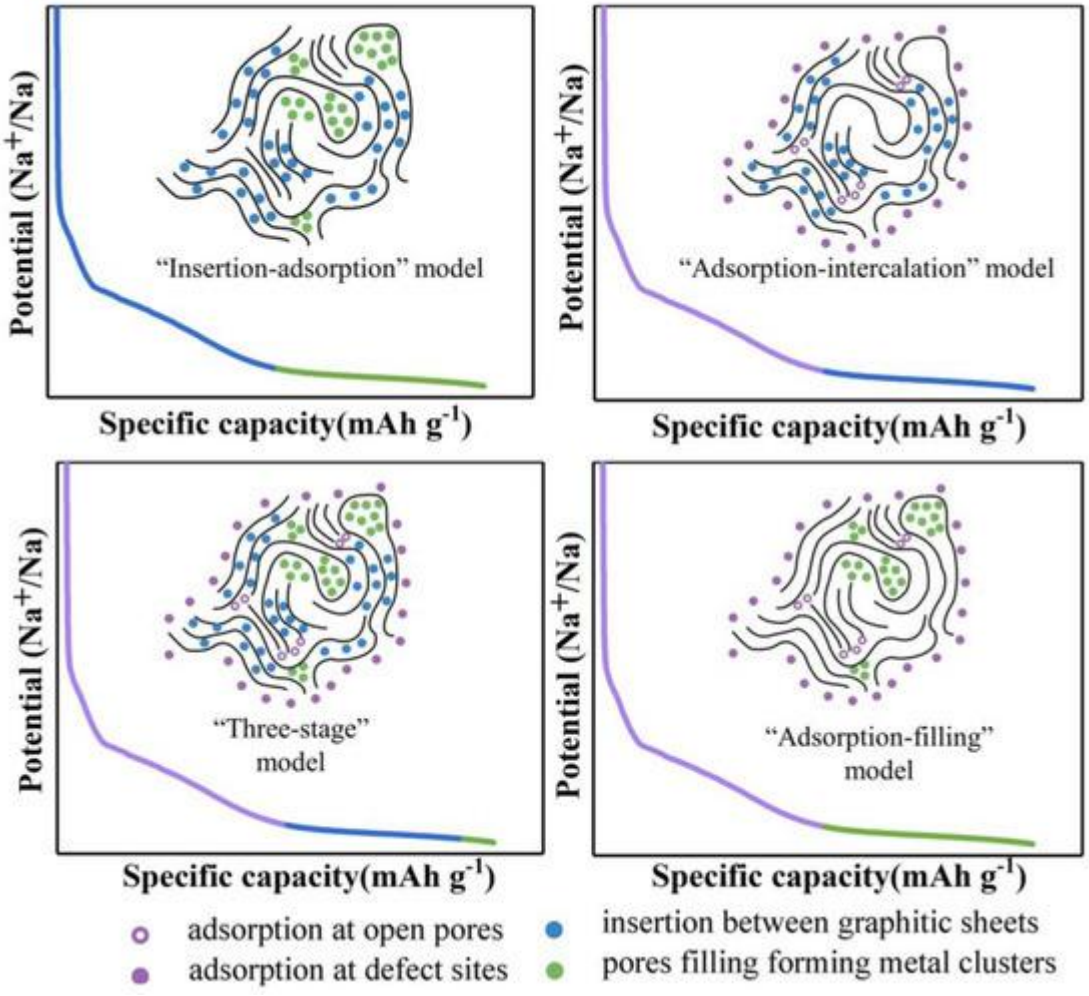

Figure 9. Four different mechanisms of sodium storage in hard carbon

Alloy-Based Materials

As shown in Figure 10, alloy-based anodes, such as those made from tin (Sn)[6], antimony (Sb), and phosphorus (P), operate on a different mechanism, forming alloys with sodium during the discharge process. These materials can offer very high theoretical capacities; however, they often suffer from large volume changes during alloying and dealloying reactions. The repeated expansion and contraction can lead to mechanical degradation and loss of electrical contact, thereby reducing the cycle life of the battery. Strategies to mitigate these issues include nanostructuring the alloy particles, embedding them in conductive matrices, or creating composite materials that can buffer the volume changes and maintain structural integrity.

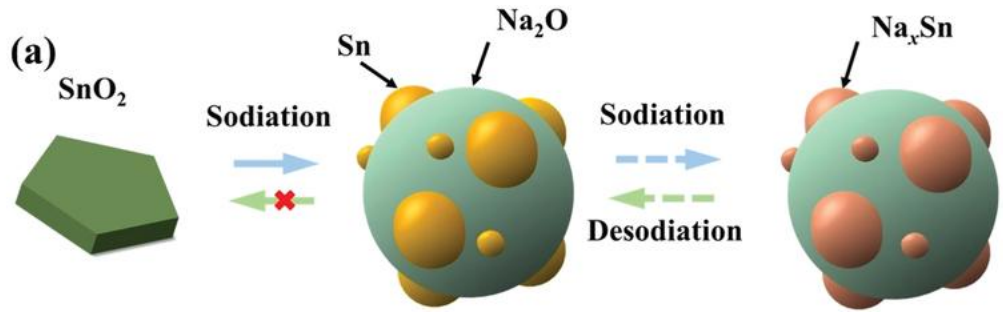

Figure 10. Schematic diagram of sodium storage for SnO_2

Conversion-Type Anodes

Conversion-type anodes involve a redox reaction that converts the initial compound into new phases during the sodiation process. These materials, such as metal oxides and sulfides, can deliver high capacities due to the complete conversion of the active material. However, the conversion reaction is often accompanied by significant structural changes and a high degree of irreversibility, which can lead to rapid capacity fading. Research efforts are directed towards engineering nanostructured materials and optimizing the reaction pathways to enhance reversibility and improve cycle life.

1.4.3 Binders

Binders play a critical role in the fabrication of battery electrodes, ensuring the mechanical stability of the electrode composite and maintaining electrical contact among active materials, conductive additives, and current collectors. In sodium-ion batteries, the choice of binder can significantly impact electrochemical performance

and cycle stability.

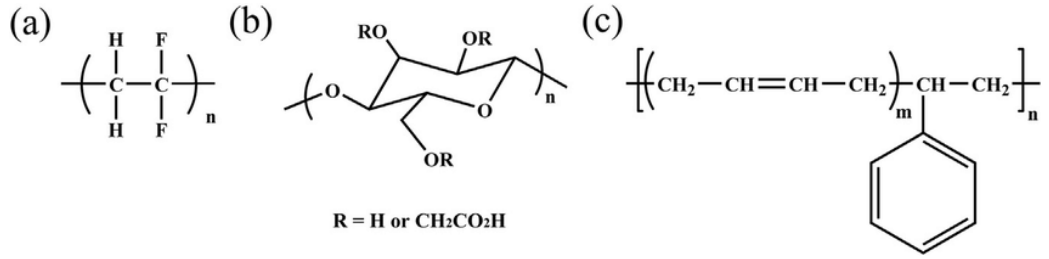

Figure 11. Molecular structures of (a) PVDF, (b) CMC and (c) SBR.

Traditional vs. Novel Binders

Figure 11 shows the commonly used binder in sodium ion battery[7], traditionally, poly(vinylidene fluoride) (PVDF) has been used as a binder in lithium-ion batteries; however, its application in SIBs is limited due to solubility issues and environmental concerns related to the use of toxic solvents like N-methyl-2-pyrrolidone (NMP). Novel binders, including water-soluble polymers such as carboxymethyl cellulose (CMC), sodium alginate, and styrene-butadiene rubber (SBR), have been explored as alternatives. These binders not only provide strong adhesion but also offer improved processability and environmental compatibility. The development of novel binder systems is a key area of research, as these materials can be engineered to enhance ion transport within the electrode, improve electrode flexibility, and reduce mechanical degradation during cycling.

Impact on Electrochemical Performance

The binder's interaction with the active materials and conductive additives is crucial for the overall electrode performance. A well-chosen binder can minimize the formation of micro-cracks during cycling, reduce the resistance at the electrode–electrolyte interface, and improve the longevity of the battery. Researchers are investigating various binder formulations to optimize the electrode architecture, balancing the need for mechanical strength with the requirement for efficient ionic conductivity. In many cases, the binder also plays a role in the formation and stability of the solid electrolyte interphase (SEI), further influencing the long-term electrochemical performance of the cell.

1.4.4 Electrolytes and Salts

The electrolyte in a sodium-ion battery serves as the medium for ion transport

between the anode and cathode. The choice of electrolyte is critical for achieving high ionic conductivity, chemical stability, and a wide electrochemical window.

Organic and Aqueous Electrolytes

Organic electrolytes, typically composed of a sodium salt dissolved in a mixture of organic solvents, have been widely used in SIB research. Figure 12 shows the commonly used organic electrolytes,[8] these electrolytes offer a broad electrochemical window, which is essential for achieving high cell voltages and preventing electrolyte decomposition. Common solvents include propylene carbonate (PC), ethylene carbonate (EC), and dimethyl carbonate (DMC). In contrast, aqueous electrolytes offer advantages such as improved safety, lower cost, and environmental friendliness. However, aqueous systems are limited by a narrower electrochemical stability window due to the decomposition of water at high voltages. Ongoing research focuses on developing novel solvent systems and optimizing electrolyte formulations to strike a balance between performance, safety, and environmental impact.

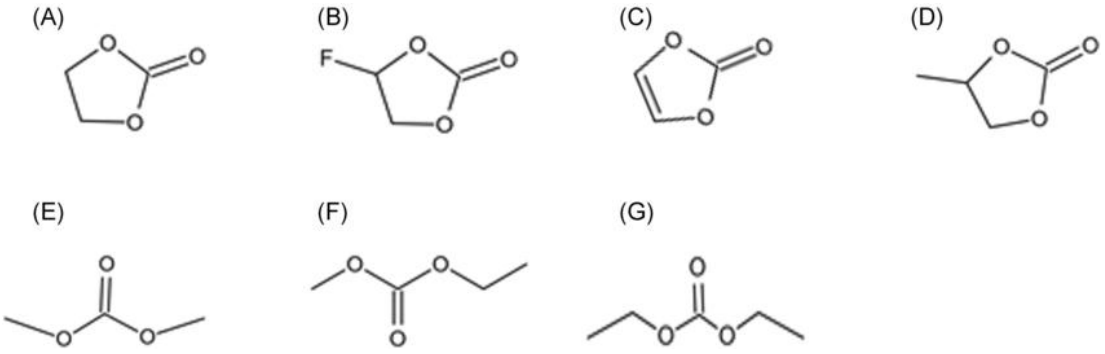

Figure 12. The molecular structures of carbonate esters. (A) Ethylene carbonate; (B) Fluoroethylene carbonate; (C) vinylene carbonate; (D) propylene carbonate; (E) dimethyl carbonate; (F) ethyl methyl carbonate; (G) diethyl carbonate

Common Sodium Salts ($NaPF_6$, NaTFSI, etc.)

The sodium salt in the electrolyte is responsible for providing sodium ions for the charge–discharge process. Figure 13 provides the commonly used sodium salts in electrolyte, salts such as sodium hexafluorophosphate ($NaPF_6$) and sodium bis(trifluoromethanesulfonyl)imide (NaTFSI) are commonly used due to their high ionic conductivity and chemical stability.[9] Each salt has its unique characteristics; for example, NaTFSI generally offers better thermal stability and a wider electrochemical window compared to $NaPF_6$. The choice of salt also influences the formation and composition

of the SEI, which in turn affects the long-term cycling stability and safety of the battery. Researchers continue to explore new sodium salts and salt mixtures to optimize ion transport and enhance overall cell performance.

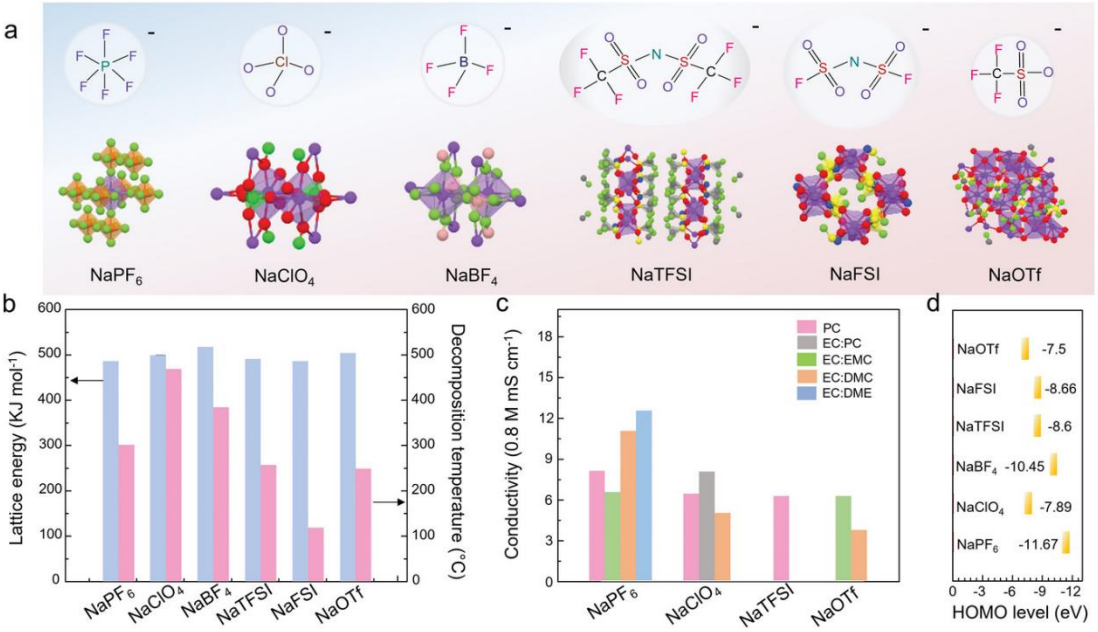

Figure 13. Chemical and physical properties of common sodium salts. a) Geometric configuration. The 3D structure is originated from Material Project database. b) Lattice energy and decomposition temperature. c) Ionic conductivity. d) HOMO level (Purple: Na; orange: P; red: O; pink: B; blue: N; grey: C; yellow: S; for $NaPF_6$, $NaBF_4$, NaTFSI, NaFSI, and NaOTf, the green color is F; for $NaClO_4$, green is Cl) (NaTFSI, sodium bis(trifluoromethanesulfonate) imide; NaFSI, sodium bis(fluorosulfonyl)imide; NaOTf: sodium trifluoromethanesulfonate).

1.4.5 Additives

Additives are incorporated into the electrolyte or electrode formulation to enhance the performance and stability of sodium-ion batteries. Even in small quantities, these substances can have a significant impact on cell behavior, especially in terms of SEI formation and electrolyte stability.

SEI-Forming Additives

The solid electrolyte interphase (SEI) is a thin layer that forms on the surface of the electrode during the initial charge–discharge cycles. This layer is crucial for stabilizing the interface between the electrolyte and the electrode, preventing continuous electrolyte decomposition. SEI-forming additives, such as fluoroethylene carbonate (FEC) and vinylene carbonate (VC) (as shown in Figure 14[10]), are often added to the

electrolyte to promote the formation of a robust and ionically conductive SEI. These additives help reduce irreversible capacity loss during the initial cycles and improve the long-term stability of the battery. The precise chemistry of the SEI can be tailored by adjusting the type and concentration of additives, thereby enhancing the performance and safety of sodium-ion batteries.

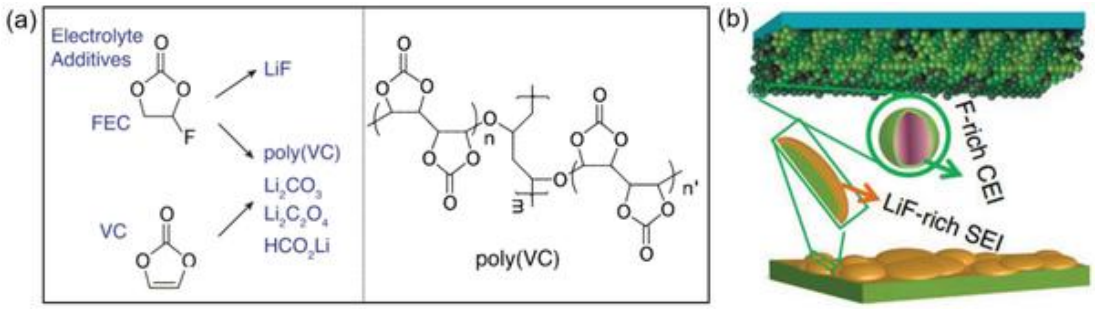

Figure 14. Schematic illustration of reduction pathway of fluoroethylene carbonate (FEC) and VC. Reproduced with permission

Borate-based additives have been extensively studied in lithium-ion batteries due to their unique chemical structures and high electron affinity. In recent years, such additives have been gradually introduced into sodium-ion battery systems and have demonstrated promising interfacial regulation capabilities. Among them, sodium bis(oxalato)borate (NaBOB) and sodium difluoro(oxalato)borate (NaDFOB) have attracted increasing attention as representative borate additives.[11-12]

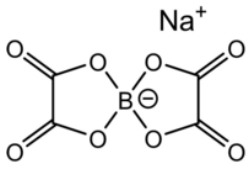

Figure 15. Structure of NaBOB

As shown in Figure 15, NaBOB is a fluorine-free boron-based sodium salt composed of two oxalate ligands coordinated to a trivalent boron center, forming a stable tridentate complex. It is readily soluble in carbonate-based electrolytes. Its main advantage lies in its ability to induce the formation of SEI layers rich in B–O and C=O bonds on the anode surface, effectively suppressing electrolyte decomposition and sodium dendrite growth, thereby significantly improving cycling stability. Furthermore, as it does not contain fluorine, it poses less environmental risk, making it a green and environmentally friendly additive.

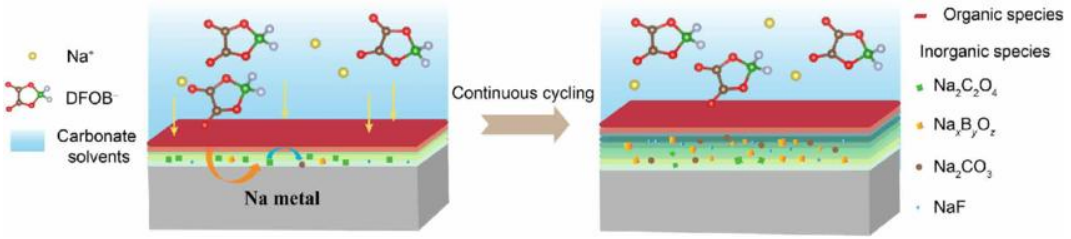

Figure 16. Schematic illustrations of the NaDFOB-derived SEI structure at the initial cycle and continuous cycles.

In contrast, NaDFOB is a fluorinated derivative of NaBOB, in which two fluorine atoms are introduced into the structure. The incorporation of fluorine greatly enhances its electron-withdrawing ability and chemical stability, making it more favorable for forming dense SEI layers with a higher inorganic content on the anode surface. Figure 16 shows the basic mechanism of NaDFOB-derived SEI formation at the initial cycle and continuous cycles. These SEI films typically contain components such as NaF, BF_x, and CO_x, which possess strong mechanical integrity and excellent electronic insulation properties. These features help isolate the sodium metal from continuous reactions with the electrolyte, ensuring good capacity retention even under high-rate cycling conditions. Moreover, NaDFOB has also shown good CEI-forming capabilities in high-voltage cathode systems, helping to mitigate electrolyte oxidation and decomposition at high potentials, thereby supporting the development of high-energy-density sodium-ion batteries.

Electrolyte Stability Enhancers

In addition to SEI-forming additives, electrolyte stability enhancers are employed to prevent undesirable side reactions and to extend the electrochemical stability window of the electrolyte. These enhancers work by scavenging reactive species, such as free radicals or dissolved oxygen, that may otherwise lead to electrolyte degradation. By improving the chemical stability of the electrolyte, these additives help maintain high ionic conductivity and prolong the operational life of the cell. Researchers are actively investigating new additive formulations to further optimize the electrolyte performance under various operating conditions, such as high temperature or rapid cycling.

Sodium-ion batteries represent a promising and sustainable alternative to lithium-ion systems, particularly for applications where cost and material abundance are critical. The emergence of SIBs is driven by the plentiful availability of sodium, lower production costs, and a reduced environmental impact. Despite facing challenges in energy density, cycle life, and electrode stability, ongoing research is steadily

improving the performance of SIBs. By addressing technical hurdles related to electrode material optimization, SEI formation, and electrolyte formulation, researchers are paving the way for the next generation of energy storage systems.

The key components of sodium-ion batteries—including cathode materials (layered oxides, polyanionic compounds, and Prussian Blue analogues), anode materials (carbon-based, alloy-based, and conversion-type), binders, electrolytes and salts, and critical additives—are integral to achieving the desired performance, safety, and longevity. Each component is the subject of intense research, with efforts focused on material innovation, improved processing techniques, and advanced cell engineering. Together, these advancements promise to transform sodium-ion battery technology from a laboratory curiosity into a commercially viable, large-scale energy storage solution.

Looking ahead, the development of SIBs holds significant promise for addressing global energy challenges, particularly in the context of renewable energy integration and grid stability. With continued collaboration between academia, industry, and government, sodium-ion batteries could play a crucial role in diversifying the energy storage landscape, reducing dependency on critical materials, and providing an environmentally sustainable solution for the future.

Chapter 2 Imidazolium based and pyrrolidinium based poly(ionic liquid) binders for hard carbon anode in sodium ion battery

2.1 Introduction

The rising demand for cost-effective and sustainable energy storage solutions has accelerated research in alternative battery technologies beyond lithium-ion batteries (LIBs). Sodium-ion batteries (SIBs) have emerged as a promising candidate due to the abundance, low cost, and environmental friendliness of sodium compared to lithium.[13-15] This makes SIBs particularly attractive for large-scale applications such as electric vehicles (EVs) and grid energy storage systems. However, despite their potential, the commercial viability of SIBs is still limited by the lack of suitable electrode materials that can deliver high performance and long-term stability.[16-18] Among the various anode materials explored, hard carbon has been identified as the most promising anode material for SIBs due to its high reversible capacity, low cost, good rate capability, and stable cycling performance.[19-20]

Hard carbon, which consists of a disordered structure with both graphitic and amorphous domains, provides ample sites for sodium-ion intercalation and storage.[21] This unique microstructure enables the material to exhibit high and stable capacity over extended cycles.[22] However, the performance of hard carbon anodes is not solely determined by the active material itself but is also significantly influenced by the choice of binder.[23] The binder, although only a small fraction of the electrode composition, plays a critical role in maintaining the structural integrity of the electrode, ensuring good contact between the active material, conductive additives, and the current collector, and facilitating efficient ion and electron transport during charge-discharge cycles.[24]

Currently, poly(vinylidene fluoride) (PVDF) is the most widely used binder in LIBs and SIBs due to its excellent chemical, thermal, and electrochemical stability.[25-26] Despite these advantages, PVDF still has some limitations when used with hard carbon anodes in SIBs. Its dissolution in organic solvents can lead to electrode performance degradation and capacity decay during long-term cycling.[27] In addition, the fluorine solvent in PVDF accepts electrons at low potentials and is reduced.[28] This phenomenon has been demonstrated in lithium-ion batteries, where fluorine accepts electrons and generates lithium fluoride, forming a thicker SEI layer.[29] Since the reduction potential of sodium is also very low (Li/Li^+: -3.04 V vs. SHE, Na/Na^+: -2.71 V vs. SHE),

it is also very easy to generate sodium fluoride. In addition, sodium fluoride (NaF) has a looser structure and lower crystallinity than lithium fluoride (LiF).[30] The SEI layer composed of NaF is more conductive and thicker, which is also demonstrated by the fact that FEC additives are not as effective in sodium-ion batteries as in lithium-ion batteries.[31-32] These drawbacks have stimulated interest in developing alternative adhesives that can provide better adhesion, electrochemical stability, and mechanical properties.

Poly(ionic liquid)s (PILs) have emerged as a new class of materials that combine the properties of ionic liquids and polymers, offering unique advantages as binders in battery electrodes.[33-35] PILs consist of a polymeric backbone with ionic liquid moieties attached, which can be tailored by choosing different cations and anions to optimize their chemical, thermal, and electrochemical properties. Their inherent ionic conductivity might enhance the ion transport within the electrode, leading to improved rate capability and cycling stability. Moreover, the flexible nature, excellent mechanical properties and moderate swelling in electrolyte of PILs allows them to maintain the structural integrity of the electrode. Recent studies have demonstrated the potential of PIL-based binders in enhancing the performance of various battery systems, including LIBs.[36-38] However, the effect and mechanism of PILs in hard carbon anodes are still unclear.

Poly(diallyldimethylammonium)(PDADMA)-based polyionic liquid polymer is a typical pyrrolidinium-based polymer, among which PDADMAC itself is a widely used polymer flocculant with a strong cat-ionic effect and can adsorb a large number of anions.[39] The aliphetic nitrogen ions on the main chain of PDADMA provide a large number of sites for anion binding, which can effectively bind to various anions in the electrolyte and accelerate the desolvation of carriers. At the same time, as a polymer of pyrrolidinium-based ionic liquids, pyrrolidinium-based ionic liquids have been widely proven to have excellent electrochemical stability in lithium-ion batteries.[41] Literature reports that the electrochemical window of lithium-ion battery electrolytes composed of pyrroli-dinium ionic liquids can exceed 5V.[40-42] It is foreseeable that this is very helpful for the long-cycle stability of sodium-ion batteries.

The same mechanism can also be applied to imidazolium-based liquids. There were literature reports that lithium-ion battery electrolytes prepared by imidazolium-based ionic liquids would degrade on the anode surface and have low electrochemical stability.[44-46] A certain degree of degradation is helpful for forming a thin and low-resistance SEI layer, but excessive degradation will reduce its mechanical properties. This may also limit its potential as a binder.

In this study, binder properties of imidazolium-based cation PEVI and pyrrolidinium-based PDADMA with fluorinated anions (FSI^-, $TFSI^-$) were analyzed as anode binders in sodium-ion batteries. Subsequently, the synthesized PILs were used as binders and the traditional binder PVDF was used as a control to prepare hard carbon anode electrode sheets and assemble sodium-ion half cells.

Our research first focuses on the distribution of active materials under electrostatic action in slurry and electrode sheet and its influence on electrode internal resistance, then focuses on the electrochemical stability of the two binders, and finally on the effect of their reduction products at low potential on SEI formation. Through these three aspects of analysis, we can make a preliminary judgment on the applicability of these two types of PILs as binders and serve as a guide for further research in the future.

2.2 Experiment method

2.2.1 Materials

Poly(diallyldimethylammonium chloride) (PDADMAC, Mw ≈400,000 - 500,000) molecular weight, 20 wt% in water, Aldrich), potassium bis(fluorosulfonyl)imide (KFSI, 99.0%, Piotrek), potassium bis(trifluoro-methylsulfonyl)imide (KTFSI, 98.0%, TCI), 1-ethtyl-3-vinylimidazolium bis(fluorosulfonyl)imide (EVIFSI, 99.0%, Piotrek) and 1-ethtyl-3-vinylimidazolium bis(trifluoromethylsulfonyl)imide (EVITFSI, 99.0%, Piotrek), 1-methyl-2-pyrrolidone (NMP, 99.0%, TCI), 1-methyl-2-pyrrolidone super dehydrated(NMP, 99.0%, Wako), poly(vinylidene fluoride) (PVDF Mw ~534000, Aldrich), hard carbon(HC, 5μm, kuraray), chloroform(99%, wako), acetylene black (battery grade, Denka), 2,2'-azobis(isobutyronitrile) (AIBN, 98.0%, Aldrich), sodium perchlorate ($NaClO_4$, wako), propylene carbonate and ethylene carbonate(PC, EC, TCI), copper foil (thickness = 20 μm, Nilaco) were used as received.

Characterization. FT-IR spectra for the polymers were recorded on a PerkinElmer 100 FT-IR spectrometer. The spectra were recorded at a resolution of 2 cm^{-1} for 10 scans in ATR mode. Field emission SEM (FESEM) images for the electrodes were obtained using a Hitachi S-5200 instrument at an accelerating voltage of 10 kV. Energy-dispersive spectroscopy (EDS) image were obtained by using a Hitachi TM3030Plus Miniscope. X-ray photoelectron spectroscopy (XPS) measurements were carried out on a Fisons instruments S-probe TM 2803 device. The coin cells were de-crimped at OCV, and the extracted electrodes were washed with dried EC:PC to remove any adsorbed salt residues before carrying out the XPS measurements. DFT calculations

were performed to optimize the structure and calculate the electronic levels using Dmol3 with the GAA functional and PBE basis set.

2.2.2 Synthesis

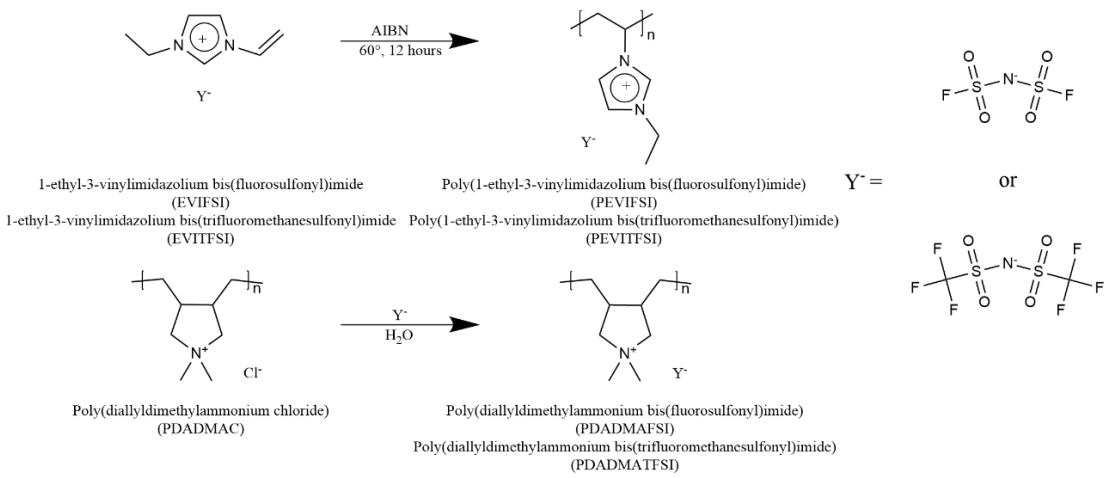

Figure 17. Reaction Scheme for the Synthesis of PEVIFSI, PEVITFSI, PDADMAFSI and PDADMATFSI.

As illustrated in Figure 17, two imidazolium-based poly(ionic liquids) were prepared via radical polymerization, following protocols adapted from previously published studies. [47] Specifically, 3.15 mmol of 1-ethyl-3-vinylimidazolium bis(fluorosulfonyl)imide (EVIFSI) was first dissolved in 25 mL of anhydrous 1-methyl-2-pyrrolidone (NMP). This solution was stirred at 80 °C, after which 0.0315 mmol of 2,2′-azobis(isobutyronitrile) (AIBN) dissolved in 1 mL of NMP was introduced. The reaction was maintained under reflux at 80 °C for 24 hours. Afterwards, most of the solvent was removed by rotary evaporation, and the resulting viscous yellow product was washed three times with 50 mL of chloroform. The final polymer was collected as a yellow solid after drying under vacuum at 80 °C for 24 hours, then transferred into an argon-filled glovebox. The isolated yield was 0.653 g, corresponding to 65.3%.

A similar approach was applied for synthesizing PEVITFSI, in which the monomer EVITFSI (3.15 mmol) replaced EVIFSI. After drying, a soft dark brown material was obtained with a yield of 1.75 g (69.7%).

Figure 17 also shows the synthesis of two pyrrolidinium-based poly(ionic liquids), prepared through salt metathesis reactions as reported in prior literature. [48] In a typical procedure, 12.38 mmol of potassium bis(fluorosulfonyl)imide (KFSI) was dissolved in 5 mL of deionized water and slowly added to a stirred aqueous solution of 6.19

mmol of poly(diallyldimethylammonium chloride) (PDADMAC) monomer units in 50 mL of distilled water at room temperature. After 8 hours of stirring, the resulting solid was collected by vacuum filtration, washed three times by redispersing in 200 mL of water under stirring for 2 hours at room temperature, and filtered again. The final white powder was dried in vacuum at 60 °C for 24 hours and transferred to a glovebox under inert atmosphere. Yield: 1.59 g (84.1%).

Using the same procedure, PDADMATFSI was synthesized by replacing KFSI with 12.38 mmol of potassium bis(trifluoromethanesulfonyl)imide (KTFSI). After drying, a white powder was obtained with a yield of 1.34 g (60.2%).

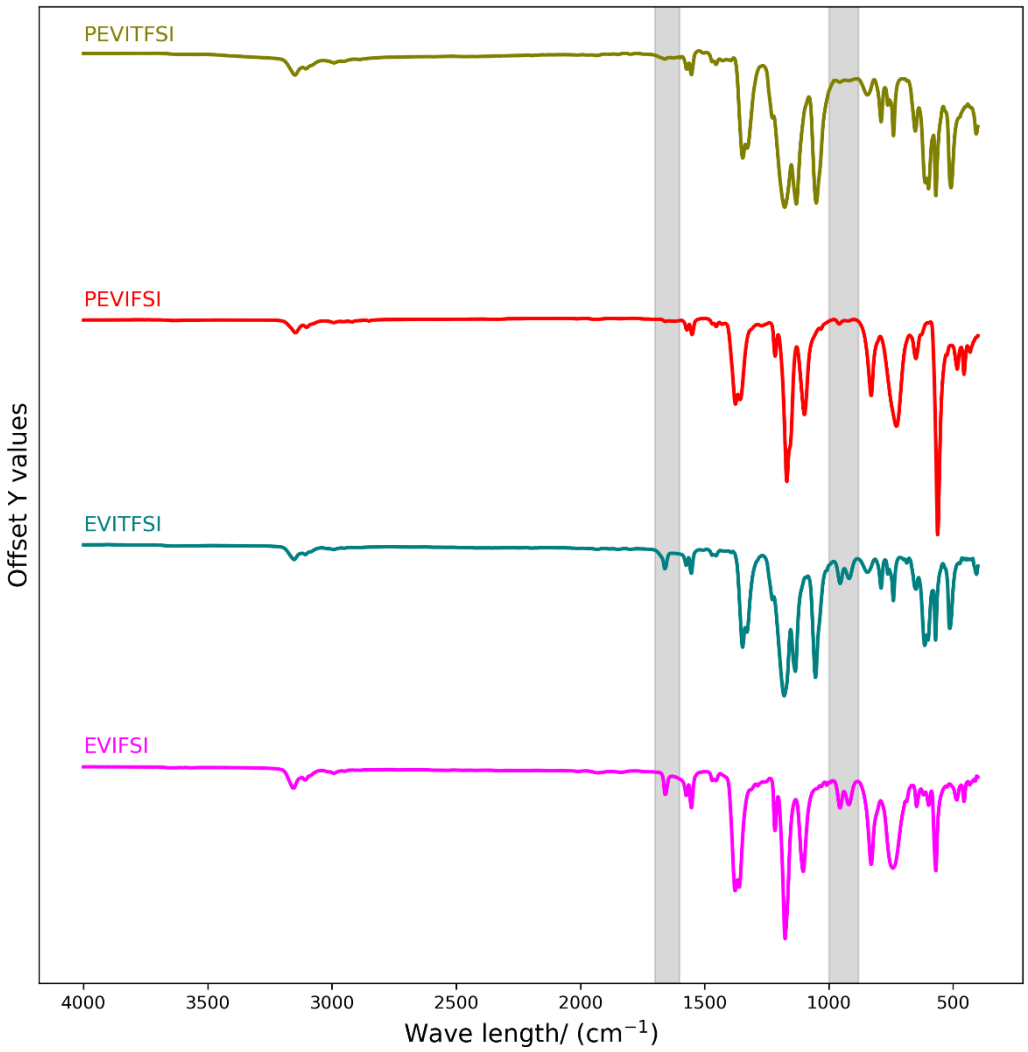

Figure 18. ATR-IR spectra of PEVIFSI, PEVITFSI, EVIFSI and EVITFSI.

Two imidazolium-based poly(ionic liquids) with FSI/TFSI anions, named PEVIFSI and PEVITFSI, were synthesized via radical polymerization.[47] The chemical structures were confirmed by FTIR, as well as by ^{1}H NMR. Figure 18 shows the FTIR spectra for EVIFSI, EVITFSI, PEVIFSI, and PE-VITFSI. When compared to the

EVIFSI and EVITFSI pre-cursors, two peaks between 1008 and 1236 cm^{-1}, attributed to the trans-asymmetric hydrogen on the car-bon-carbon double bond present in the monomers, disappeared for both PEVIFSI and PEVITFSI. Additionally, a peak at 1659 cm^{-1}, associated with the vibration of the carbon double bond outside the ring structure of the imidazolium, also disappeared. These results confirm that the carbon-carbon double bonds were completely consumed in the reaction. Since the glass transition temperature of PEVITFSI is lower than room temperature, it can hardly be used as a binder at room temperature and is therefore excluded from the binder candidate.

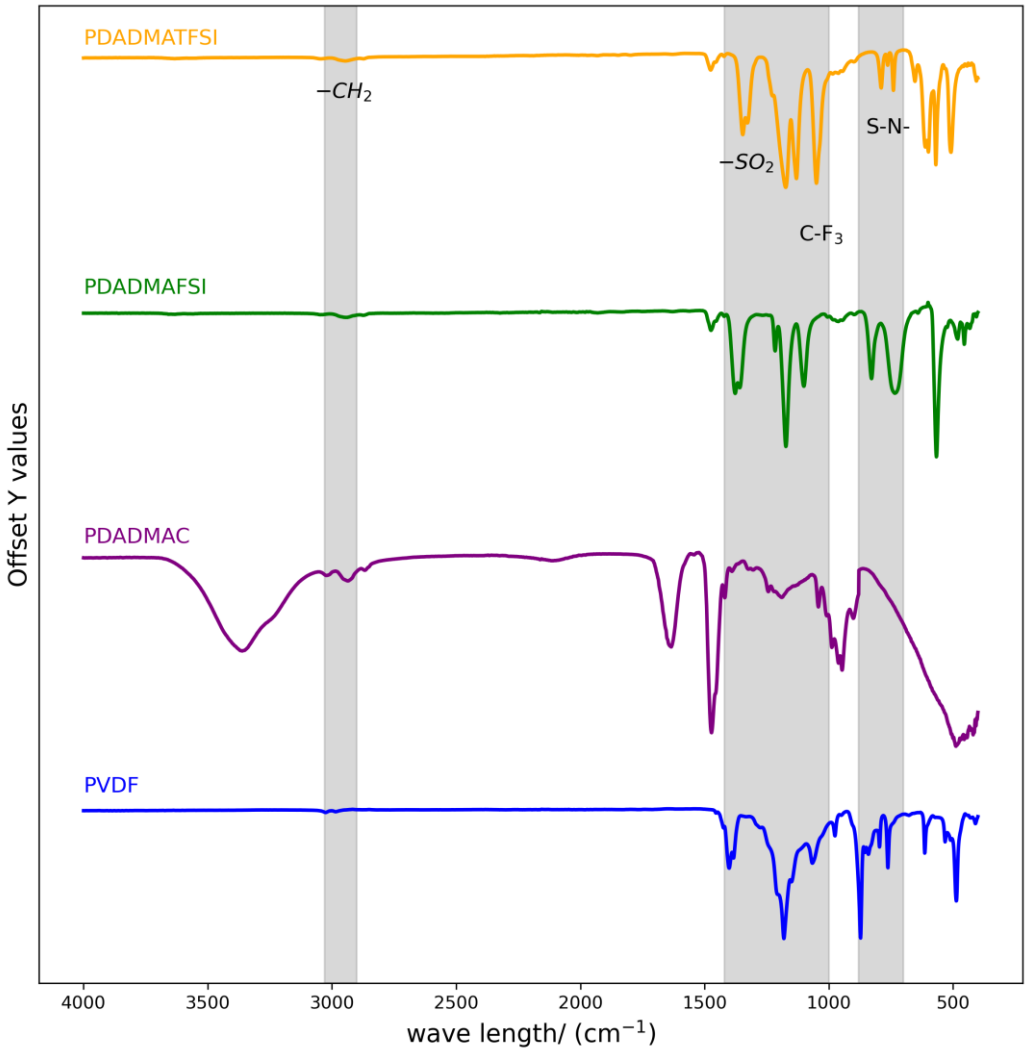

Figure 19. ATR-IR spectra of PDADMATFSI, PDADMAFSI, PDADMAC and PVDF.

Two pyrrolidinium-based poly(ionic liquids) with FSI/TFSI anions, named PDADMAFSI and PDADMATFSI, were synthesized through salt metathesis reactions. The chemical structures were confirmed by FTIR, as well as by ^{1}H NMR. Figure 19 shows the FTIR spectra for PVDF, PDADMAC, PDADMAFSI, and

PDADMATFSI. Characteristic peaks of the PDADMA cation were found at 2900–3100 cm^{-1} and 1472 cm^{-1} in all IR spectra. Compared to the PDADMAC precursor, two new peaks, related to the fluorinated anions, appeared at 669–861 cm^{-1} (attributed to symmetric and asymmetric S–N–S stretching) for both PDADMAFSI and PDADMATFSI. Additionally, two new peaks appeared at 1284–1410 cm^{-1} (attributed to -SO_2 asymmetric stretching), and a peak at 1450 cm^{-1} (at-tributed to C–F_3 asym-

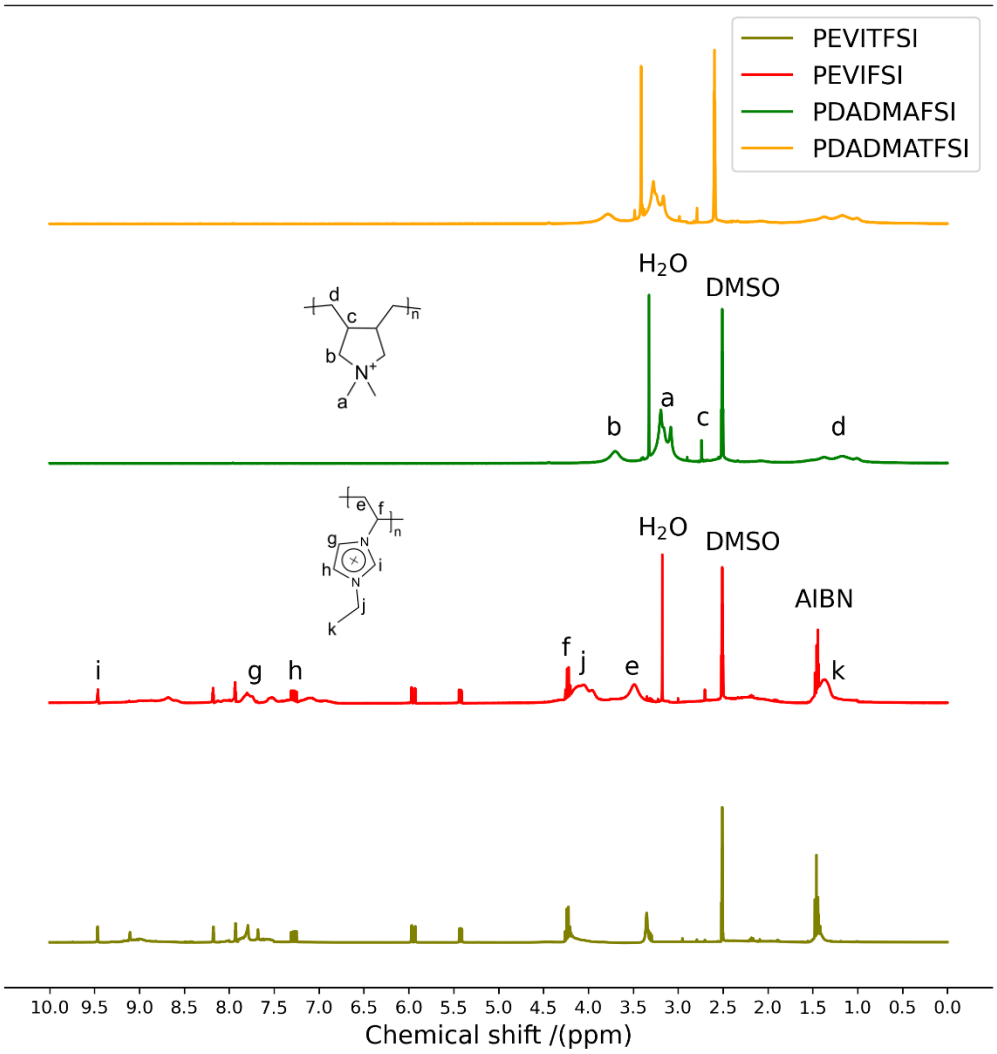

metric stretching) were observed for PDADMATFSI. These results are consistent with previously reported fluorinated PDADMA based poly(ionic liquid)s.[48]

Figure 20. ^{1}H NMR for PEVIFSI, PEVITFSI, PDADMAFSI and PDADMATFSI

The ^{1}H NMR spectra for all four PILs are presented in Figure 20, with peak assignments for PEVIFSI and PDADMAFSI provided as an example.

2.3 HOMO-LUMO calculation

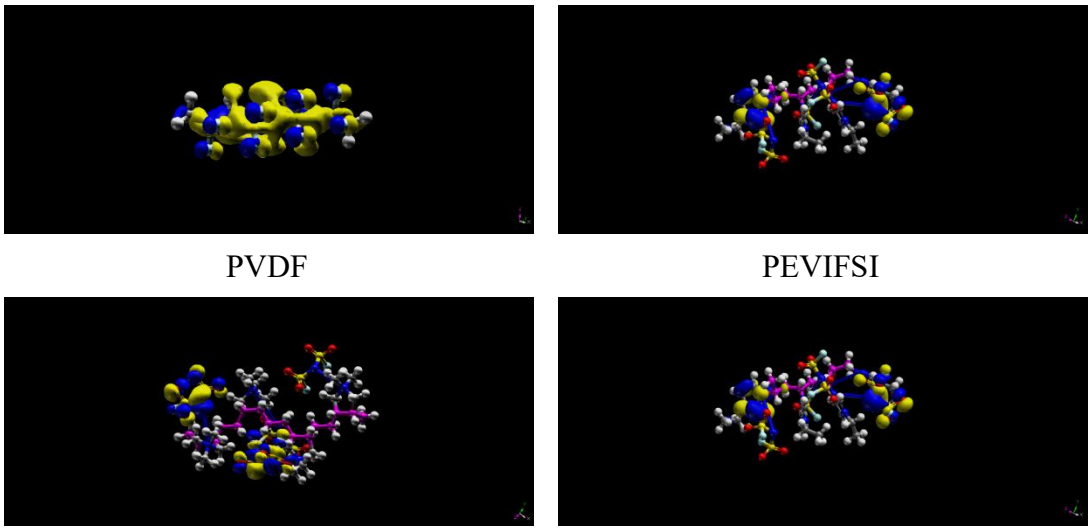

Figure 21. Frontier molecular orbital diagram for PVDF, PEVIFSI, PDADMAFSI, PDADMATFSI tetramer, calculated by dmol3.

The electronic structure parameters, including the highest occupied molecular orbital (HOMO) and lowest unoccupied molecular orbital (LUMO) energies, are critical indicators of the electrochemical stability and performance of polymer binders. The geometry structure of PVDF, PEVIFSI, PDADMAFSI, PDADMATFSI tetramer optimized by Dmol3 and their frontier molecular orbital diagram was shown in Figure 21. The HOMO-LUMO values obtained for the tetramer are given in Table 1. For PVDF, the HOMO energy(eV) is at -7.481 eV, and the LUMO energy is at -0.073 eV, reflecting its high stability. In comparison, the imidazolium-based PEVIFSI exhibits a HOMO energy of -6.936 eV and a lower LUMO energy at -2.904 eV. Previous research has shown that the imidazole group shows strong electro-chemical degradation. In contrast, the pyridinium-based PDADMAFSI and PDADMATFSI binders demonstrate more favorable electronic properties. PDADMAFSI shows a HOMO energy of -6.404 eV and a LUMO energy of -1.309 eV, while PDADMATFSI has a HOMO energy of -5.611 eV and a LUMO energy of -1.760 eV. In the anodic environment, lower LUMO value helps it to accept electrons at the anode, reduces the side reactions of the electrolyte at the anode, and helps to form a more stable solid electrolyte interface (SEI). Lower LUMO energy of PDADMAFSI and PDADMATFSI is caused by the FSI and TFSI anions. Previous studies showed the FSI and TFSI anions have lesser electrochemical degradation. This degradation will not destroy the main chain structure of the polymer, but helps forming a dense LiF containing SEI layer, so

this degradation should have limited effect on the stability of the electrode structure.

Table 1. Theoretical E_{LUMO}, E_{HOMO}, and Band Gap Values for PVDF, PEVIFSI, PDADMAFSI and PDADMATFSI.

Chemical moiety (tetrameric units)	E_{LUMO} (eV)	E_{HOMO} (eV)	Band gap (eV)
PVDF	-0.073	-7.481	7.408
PEVIFSI	-2.904	-6.936	4.032
PDADMAFSI	-1.309	-6.404	5.095
PDADMATFSI	-1.760	-5.611	3.851

2.4 Electrode preparation

Slurry was prepared by mixing 80 wt % of hard carbon, 10 wt % acetylene black, and 10 wt % binder in NMP. Electrodes were fabricated by casting as-prepared slurry onto copper foil using a doctor blade. Electrodes were dried overnight under vacuum at 80 °C to remove NMP. The dried electrodes were hot pressed at 80 °C for 6 h. The dried electrodes were punched into disks with area 1.72 cm^2 to be used for testing in coin cells. 2025-coin cells were assembled to carry out the electrochemical testing using the as-fabricated hard carbon electrodes as anodes, sodium foil as counter and reference electrodes with a microglass fibre separator (Whatman GF/C), and 1.0 M $NaClO_4$ in 1:1 EC:PC as electrolyte. The anodic half-cells were assembled inside an argon-filled glovebox (UNICO UN-650F) whose moisture and O_2 content was <0.1 ppm. The assembled cells were rested for 6 h for stabilization before carrying out the electrochemical characterization.

2.5 Peel test

Figure 22 shows the Scotch tape test or peel test carried out to qualitatively assess the adherence of the electrode material to the current collector. A Scotch tape was pasted onto the electrode affixed on a glass plate and was removed. The loss in the weight of electrode material was measured. Electrodes with PEVIFSI, PDADMAFSI, PDADMATFSI as binder showed 74%, 94% and 99% retention of the active material to the current collector respectively, compared to the 86% for PVDF-based electrodes.

Lower mechanical strength of electrode using PEVIFSI as binder may be due to its lower Degree of Polymerization (~520).

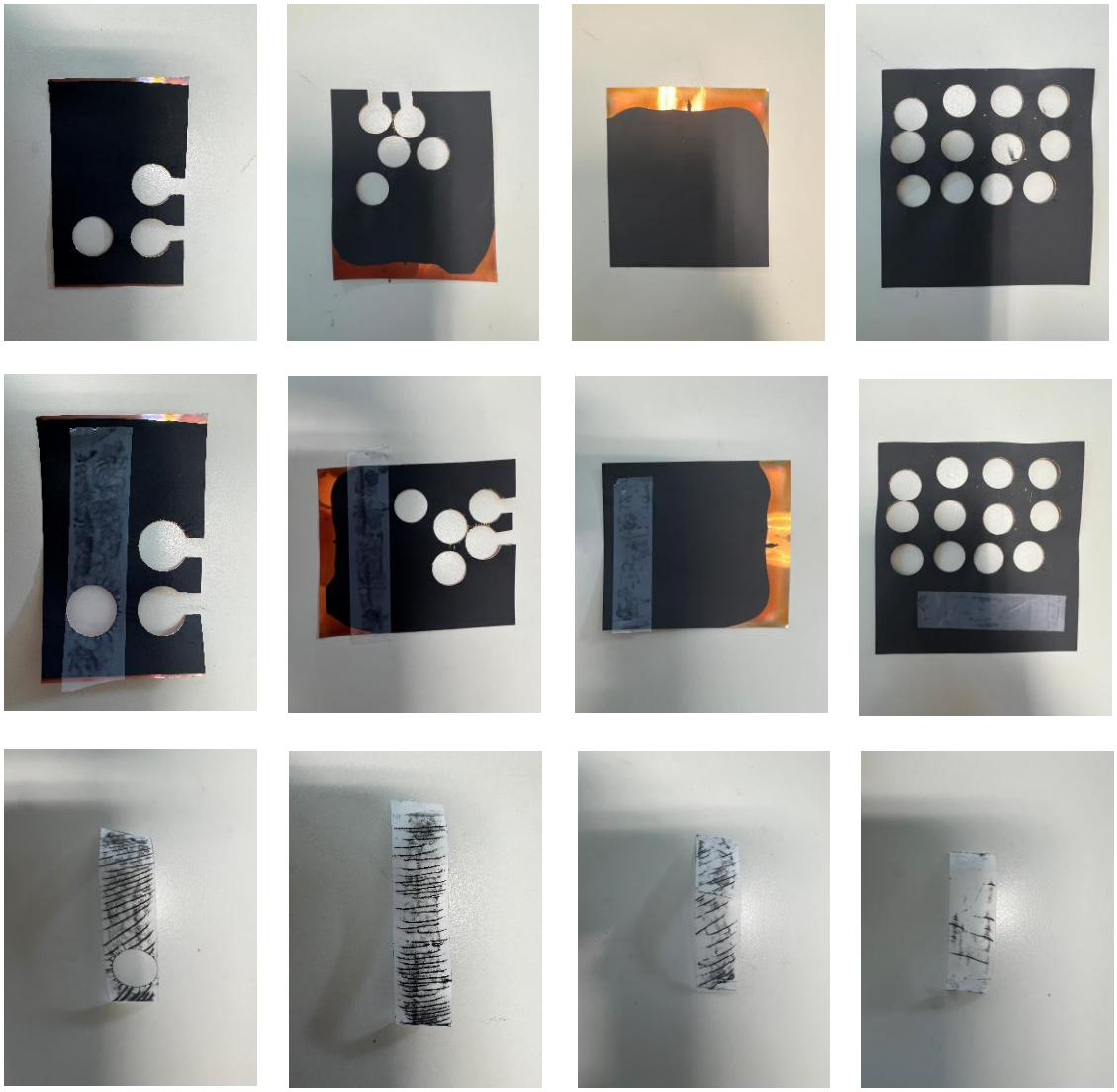

Figure 22. Scotch tape test to check the adherence of the electrode material to the current collector.

2.6 XPS test before cycling

Figure 23 shows the XPS survey test of the electrode by using PDADMAFSI and PDADMATFSI as biners, Similar tests were also conducted in SEM EDX. Table 2 shows the surface element ratio obtained by XPS test. The results show that the chlorine content on the electrode surface is beyond the lower limit of instrument detection. In addition, due to ion exchange, nitrogen content can be observed on the electrode surface, which can only be contributed by nitrogen in FSI^- and $TFSI^-$. These results

further prove that ion exchange is fully carried out.

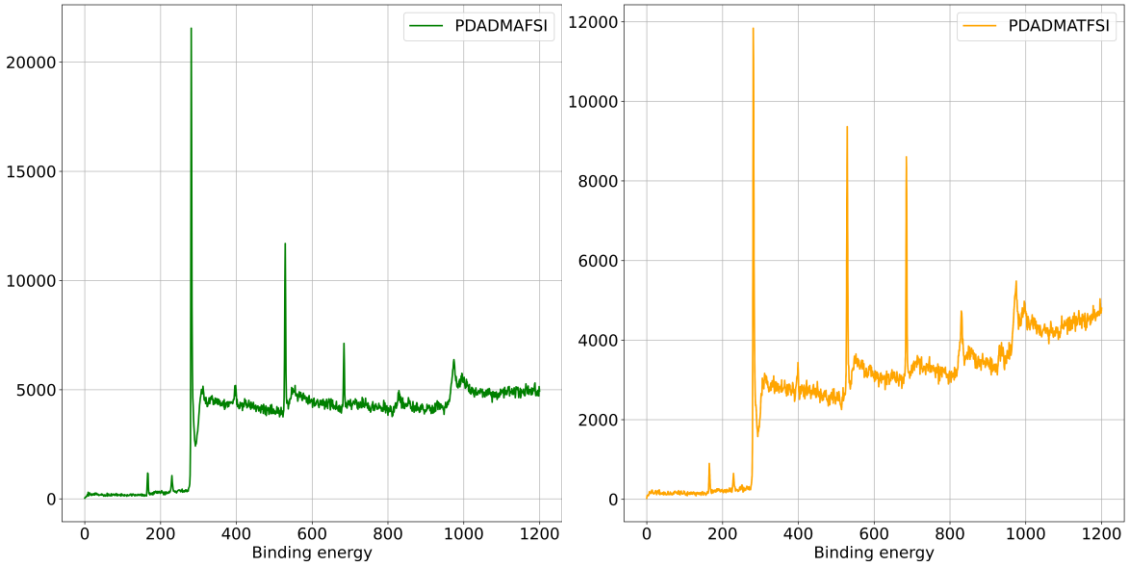

Figure 23. XPS survey test of the electrode by using PDADMAFSI (green) and PDADMATFSI (orange) as binder

Table 2. Element ratio in the surface of electrode by using PDADMAFSI and PDADMATFSI as binders from XPS test.

PDADMAFSI electrode		**PDADMATFSI electrode**	
Element	**Atomic %**	**Element**	**Atomic %**
C	94.19	C	93.47
Cl	0.00	Cl	0.00
S	0.61	S	0.51
O	4.26	O	3.97
F	0.89	F	2.04
Total	100.00	Total	100.00

Chapter 3 Electrochemical characterization and post-mortem studies

3.1 Test condition

The electrochemical impedance spectroscopy (EIS) and dynamic electrochemical impedance spectroscopy (DEIS) measurements were carried out on a VSP potentiostat electrochemical workstation equipped with a frequency response analyzer (FRA). The EIS measurements were carried out after stabilizing as-assembled cells and after charge−discharge cycling in the frequency range from 1 MHz to 100 mHz with a sinus amplitude of 10 mV. The cyclic voltammetry (CV) studies and linear scan voltammetry (LSV) were carried out on a VSP potentiostat electro-chemical workstation from Bio-Logic Science Instruments. The CV measurements were carried out in the potential range 10−2500 mV vs Na/Na+ at a scan rate of 0.1 mV/s. The scan rate studies using CV were carried out at scan speeds of 0.1 mV/s, 0.25 mV/s, 0.5 mV/s, 0.75 mV/s, and 1.0 mV/s. The charge−discharge measurements were carried out on the Electrofield ABE 1024 battery cycler using a CC-mode in the potential range 10−2500 mV vs Na/Na^{+}. Charge−discharge measurements at different rates (35 mA/g, 70 mA/g, 175 mA/g, 350 mA/g, 700 mA/g, 35 mA/g) were carried out to evaluate the stability of the electrodes. Long charge−discharge cycling for 300 cycles was carried out at 50 mA/g to evaluate the cyclability of the electrodes. The DEIS measurements were carried out on the cells after 5 cycles of CV test.

3.2 Cylic Voltammetry

The binder profoundly affects the formation process of SEI and thus affects other properties of the cell. Understanding the nature of the SEI (solid electrolyte interphase) formed provides valuable insights into the functioning and performance of binders in sodium-ion batteries (SIBs). In the current study, electrochemical techniques such as Cyclic Voltammetry (CV), Electrochemical Impedance Spectroscopy (EIS), and Dynamic Electrochemical Impedance Spectroscopy (DEIS) were employed to investigate the SEI properties and the performance of hard carbon anodes with different binders. Specifically, four binders—PDADMATFSI, PDADMAFSI, PVDF, and PEVIFSI—were evaluated to understand their impact on SEI behavior and sodium-ion intercalation-deintercalation dynamics.

Cyclic voltammetry (CV) is an essential electrochemical technique used to study

redox reactions and electron transfer kinetics of electroactive species. In CV, the potential of the working electrode is swept linearly versus time in a triangular waveform, typically within a defined range. As the potential scans forward and then reverses, the resulting current is measured, producing a characteristic cyclic voltammogram. The observed current originates from the oxidation or reduction of the analyte near the electrode surface and is controlled primarily by diffusion.

For a cyclic potential scan, the current–voltage response becomes more complex. For a reversible redox couple:

$$O + ne^- \leftrightarrow R$$

The peak current during the forward scan (reduction or oxidation) is given by the Randles–Sevcik equation:

$$i_p = (2.69 \times 10^5) \cdot n^{3/2} A D^{1/2} C^* \nu^{1/2}$$

where:

i_p: peak current (in amperes)

ν: scan rate (in V/s)

n: number of electrons transferred

A: electrode area

C^*: bulk concentration of the analyte

This relationship shows that the peak current is proportional to the square root of the scan rate, which can be experimentally verified. Moreover, the shape and position of the peaks provide insight into the reversibility of the redox system, the diffusion coefficients, and the electron transfer kinetics.

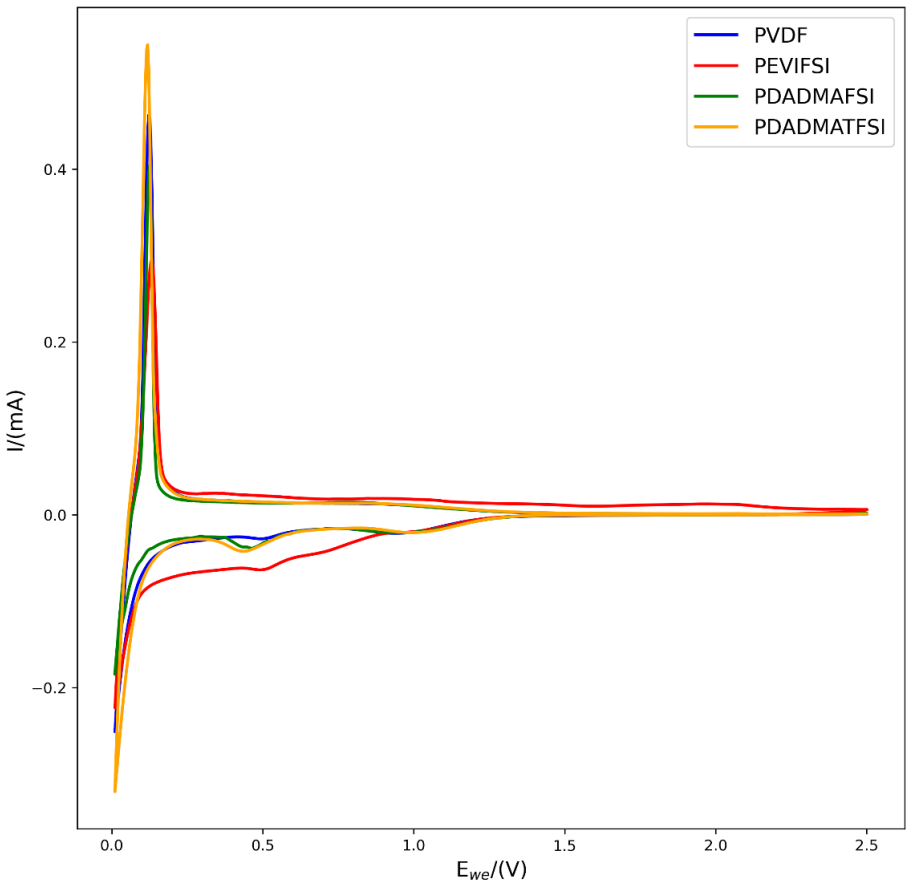

Figure 24　Cyclic volatmmograms of PVDF(blue), PEVIFSI(blue), PDADMAFSI(green) and PDADMATFSI(orange) as binders for the hard carbon anode in 1.0M $NaClO_4$/EC:PC in first cycle at a scan rate of 0.1mV/s.

Here, CV measurements were conducted to evaluate the nature of the SEI and sodium-ion storage behavior during the first several intercalation cycles. Figure 24 shows the CV test result of first electrochemical cycle. In first electrochemical cycle, the half cells assembled with PILs and PVDF as anode binders showed a typical intercalation−deintercalation profile of a hard carbon anode, in which sodiation peak was observed at 0.011V for every half cells, desodiation peak was observed at 0.12V, 0.11V, 0.13V, and 0.11V for the anodic half cells based on PVDF, PEVIFSI, PDADMAFSI, PDADMATFSI as binders, respectively.

On the other hand, anodic half cells based on PVDF, PEVIFSI, PDADMAFSI and PDADMATFSI showed different electrochemical behaviors between 0.3-0.5V vs Na/Na^+, which is widely considered to be the range of SEI formation. The intensity and the area under these peaks in the voltammogram correspond to the amount of electrolyte being reduced. Among them, the anodic half cells assembled with PVDF as a binder showed a very weak SEI reduction current, while the anodic half cells assembled with PDADMAFSI and PDADMATFSI as binders showed stronger and very

similar SEI formation peaks. The anodic half cells assembled with PEVIFSI as a binder showed electrochemical behaviors that were inconsistent with the other three binders. It showed a larger reduction current between 0.01-1V, suggesting that PE-VIFSI as a binder was degraded. Early studies have shown that the imidazole group will be reduced at low potentials, to first form carbene, and then carbene will continue to form a series of derivatives.[48] In summary, the results of the CV tests are in consistent with the results calculated in dmol3.

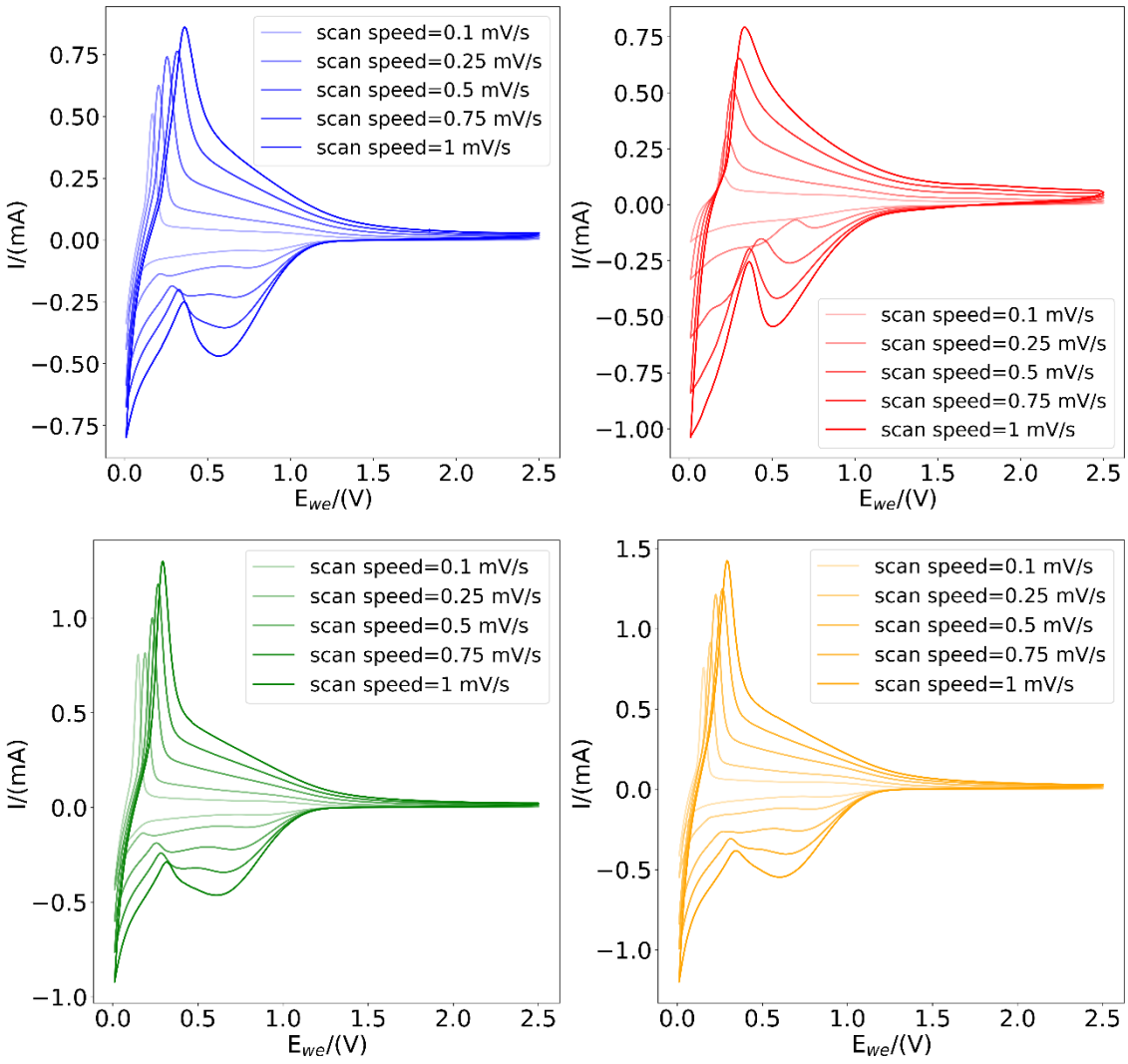

Figure 25. Cylic voltammograms at different scan rate with PVDF(blue), PEVIFSI(red), PDADMAFSI(green), PDADMATFSI(orange) as binders for the hard carbon anode in 1.0M $NaClO_4$/EC:PC.

Table 3. Overpotential of anodic half cells fabricated by using PVDF, PEVIFSI, PDADMAFSI and PDADMATFSI as binders and hard carbon as active material at different scan speed.

Scan speed (mV/s)	PVDF /HC	PE-VIFSI/HC	PDADMAFSI/ HC	PDADMAT-FSI/HC
0.1	0.169	0.209	0.149	0.156
0.25	0.206	0.229	0.186	0.193
0.5	0.256	0.262	0.232	0.226
0.75	0.302	0.302	0.262	0.26
1	0.356	0.336	0.29	0.293
Overpotential	0.187	0.127	0.14	0.137

To further investigate the sodiation-desodiation process, CV-based scan rate studies were performed. CV measurements were carried out on half-cells with hard carbon anodes based on PVDF, PEVIFSI, PDADMAFSI, PDADMATFSI binders at different scan rates. Figure 25 shows the cyclic voltammograms at scan rates ranging from 0.1 mV/s to 1 mV/s. A noticeable overpotential was observed for all materials as the scan rate increased, as summarized in Table 3. Half-cells using PILs as anode binders demonstrated significantly lower overpotentials compared to those using PVDF as binders (0.127V for PEVIFSI, 0.134V for PDADMAFSI, 0.137V for PDADMATFSI vs 0.187V for PVDF). Additionally, at the same scan rate, for example, at the scan speed of 0.1 mV/s, desodiation potentials of half-cells with PDADMAFSI and PDADMATFSI binders were lower than those with PVDF and PEVIFSI binders (0.149V and 0.156V vs. 0.169V and 0.209V, respectively). In addition to the highest oxidation potential of the anode half-cell using PEVIFSI as a binder, the higher R_{SEI} also causes the polarization brought about by the faster scanning speed, which makes the degradation peak of PEVIFSI clearer. Besides, the anode half-cell using PEVIFSI as a binder showed reduction current in the range of 0.01V-0.5V, especially at scanning speeds of 0.25 mV/s and 0.5mV/s. which further proved the electrochemical instability of the PEVIFSI binder itself.

3.3 Charge-Discharge Study

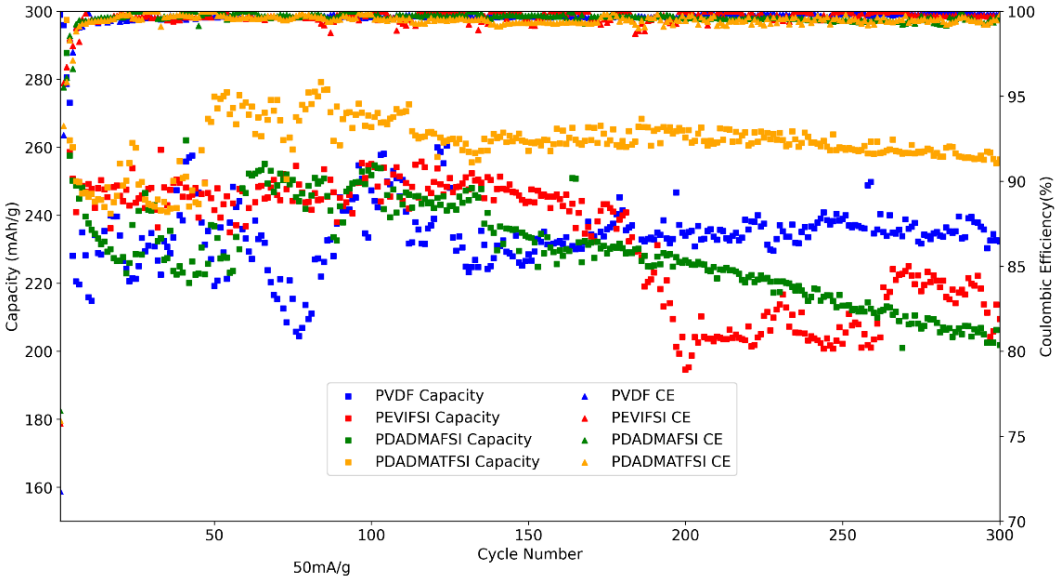

Figure 26. Long cycling performance of hard carbon anodes with PVDF(blue), PEVIFSI(red), PDADMFSI(green) and PDADMATFSI(orange) as binders with 1.0M $NaClO_4$/EC:PC electrolyte at current density of 50 mA/g.

Figure 26 shows the performance of half-cells assembled using 4 different polymers as anode binders under long-term cycle testing. The half cells assembled with three PILs: PEVIFSI, PDADMAFSI, and PDADMATFSI as binders showed the capacity values of 321.61 mAh/g, 304.58 mAh/g, 315.47 mAh/g and coulombic efficiencies of 75.8%, 76.5%, and 75.9% in the first cycle, respectively. However, the coulombic efficiency of the half cells assembled with PVDF as a binder was only 71.7% in the first cycle and the capacity value of the half cells assembled with PVDF as a binder was only 298.95 mAh/g in the first cycle. The higher first efficiency may be related to the uniformity of the electrode. In NMP, the positive charge in PIL causes mutual repulsion between the binder, helps to form a more homogeneous slurry, and contributes to the smooth morphology of the electrode. This allows the cell to be more fully activated in the first few cycles, and a higher proportion of active materials is allowed to participate in the electrochemical reaction. After 300 cycles of testing, the half-cells using PVDF and PDADMATFSI as binders have excellent capacity retention, 82.7% and 81.3%, respectively. In addition, the anodic half-cell using PDADAMTFSI as a binder maintains the highest capacity during the first two hundred cycles. At the same time, the capacity of the half-cell using PVDF as binder showed a sudden increase and a sudden decrease of capacity in some cycles, whereas the capacity of the half-cell using PDADMATFSI as a binder was more stable. Half-

cell using PEVIFSI and PDADMATFSI as binders showed capacity retention of only 65.7% and 66.3%. Among them, the anodic half-cell using PEVIFSI as a binder showed a rapid capacity decay after the 180th cycle, and the anodic half-cell using PDADMAFSI as a binder began to slowly decay in capacity after the 130th cycle. This may be caused by the depletion of the electrolyte. Since the results of CV and EIS tests in the half cell fabricated using PEVIFSI as anodic binder indicated its stronger degradation, this result of long cycle test is in line with those results. This also indicates that imidazolium-based PILs are not suitable as binders for use in the anodic environment of SIBs.

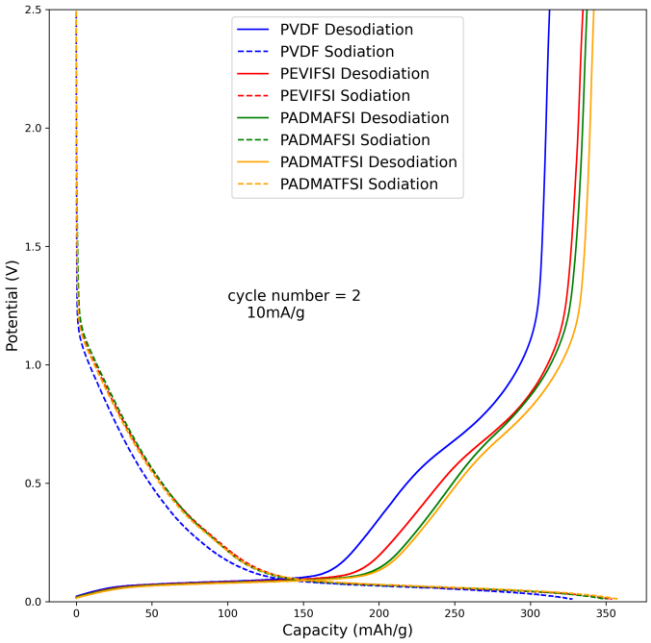

Figure 27. Charge-discharge profiles during the 2_{nd} cycle for hard carbon anodes with PVDF, PEVIFSI, PDADMAFSI and PDADMATFSI as binders.

Figure 27 shows the charge−discharge profiles for the half cells prepared by PILs and PVDF as anode binders. After the first cycle charge−discharge test, the half-cells were tested at a current of 10 mA/g. The results indicate that the half-cell using PVDF as the anode binder exhibited a lowest capacity of 327.2 mAh/g. In contrast, the half-cells using PEVIFSI, PDADMAFSI and PDADMATFSI as anode binders demonstrated significantly higher capacity, reaching 353.85 mAh/g, 350.24 mAh/g and 358.67 mAh/g, respectively.

3.4 Rate Study

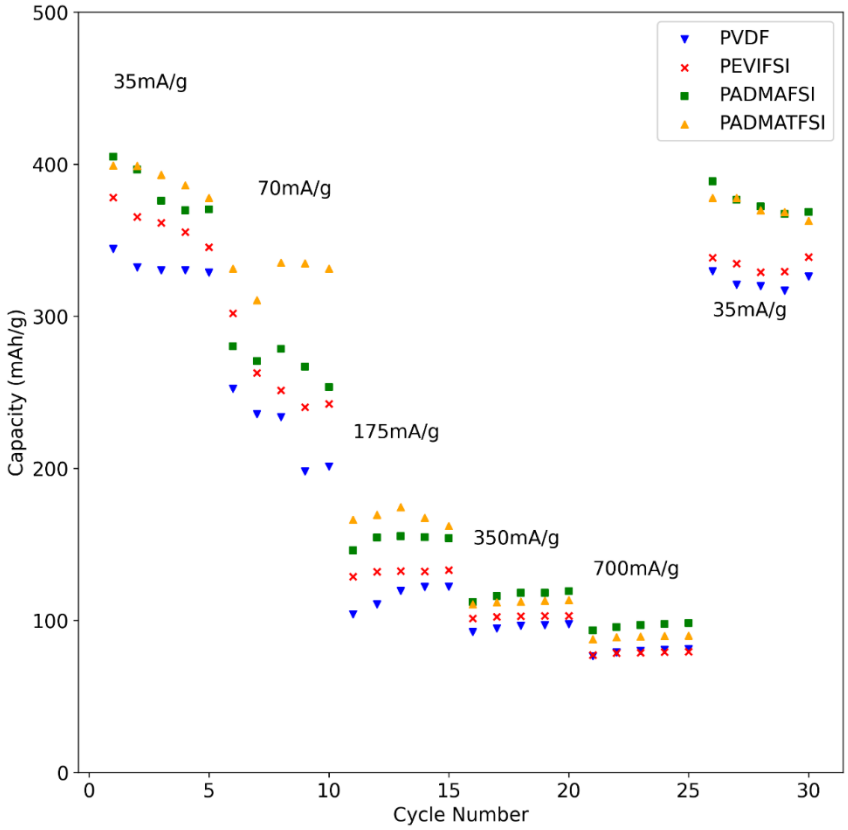

Figure 28. Rate performance of hard carbon anodes with PVDF, PEVIFSI, PDADMAFSI and PDADMATFSI as binders with 1.0M $NaClO_4$/EC:PC electrolyte.

Figure 28 gives the charge−discharge rate studies performed at different rates for half-cells with poly(ionic liquid) binders and PVDF binders. Result shows half-cells with the PILs as anode binders outperform those with PVDF at all current density. Table 4 summarize the average capacity of half cells fabricated by different binders at different current density. At the lower current densities of 35 mA/g and 70 mA/g, the average capacities of the half-cells using PDADMATFSI as anode binder were 391.1 mAh/g and 328.7 mAh/g, respectively, while the average capacities of the half-cells using PDADMAFSI and PEVIFSI as anode binders were 383.5 mAh/g, 361.2mAh/g at the current density of 35 mA/g, and 270 mAh/g, 259.8 mAh/g at the current density of 70 mA/g. The average capacity of the half-cells using PVDF as anode binder was only 333.3mAh/g and 224.3mAh/g. The capacity of the anodic half-cell using PDADMATFSI as a binder was increased by 17.34%, 8.44%, and 1.98% respectively at a current density of 35 mA/g compared to the anodic half-cell using PVDF, PE-VIFSI, and PDADMAFSI as a binder. The capacity of the half-cell using PDADMAT-FSI as the anode binder at a current density of 700 mA/g is 12.06% higher than that of

the half-cell using PVDF as the binder (89.2 mAh/g / 79.6 mAh/g). It is worth noting that higher current density means stronger electrochemical polarization and intensifies the decomposition of the binder. The half-cells using PDADMATFSI, PDADMAFSI, PVDF, and PEVIFSI as anode binders have capacities of 371.4 mAh/g, 374.8 mAh/g, 322.7 mAh/g, and 334.2 mAh/g at current density of 35 mA/g after the rate test. Compared with the average capacity of the first five cycles of 35 mA/g, capacity retention was 94.9%, 97.7%, 96.8% and 92.5%. For the PEVIFSI binder, the decomposition of the binder after the rate test may form a thicker SEI layer, this resulted in a lower recovery rate for PEVIFSI system. In contrast, the half-cell using PDADMATFSI as the anodic binder showed fast charging capability.

Table 4. Average capacity of half cells fabricated by PILs binders and PVDF at different current density.

	35 mAh/g	70 mAh/g	175 mAh/g	350 mAh/g	700 mAh/g	35 mAh/g (after rate study)
PVDF	333.3	224.3	115.7	95.7	79.6	322.7
PEVIFSI	361.2	259.8	131.7	102.6	78.7	334.2
PDADMAFSI	383.5	270	153	116.8	96.4	374.8
PDADMATFSI	391.1	328.7	168	112.3	89.2	371.4

3.5 Electrochemical impedance spectroscopy(EIS)

Electrochemical Impedance Spectroscopy (EIS) is a powerful technique used to characterize the frequency-dependent response of an electrochemical system. It is particularly useful in studying charge transfer processes, diffusion, double-layer capacitance, and the integrity of coatings or solid-electrolyte interfaces. In an EIS experiment, a small amplitude sinusoidal voltage perturbation $E(t)=E_0\sin(\omega t)$ is applied to the electrochemical cell, and the resulting current $I(t)$ is measured. The impedance $Z(\omega)$ is defined as the ratio of the voltage to current in the frequency domain:

$$Z(\omega)=E(\omega)/I(\omega)$$

For linear systems, the response current is also sinusoidal with the same frequency ω, but generally phase-shifted:

$$I(t)=I_0\sin(\omega t+\phi)$$

where ϕ is the phase angle between voltage and current. Using complex notation:

$$Z(\omega)=Z'(\omega)+jZ''(\omega)$$

where:

- Z' is the real part (resistive component)
- Z'' is the imaginary part (capacitive or inductive component)

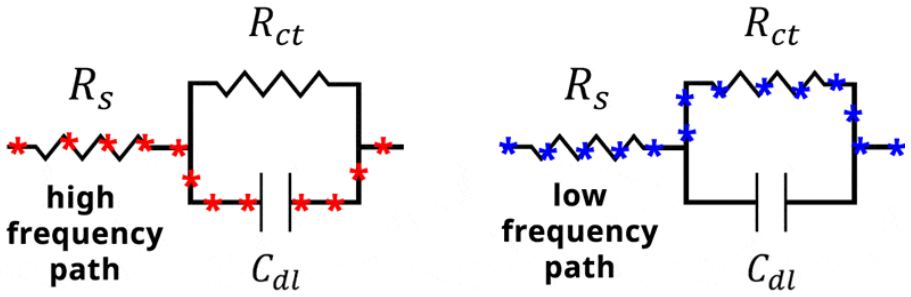

Figure 29. Randles circuit, a model for a semi-infinite diffusion-controlled faradaic reaction to a planar electrode.

As shown in Figure 29, the simplest model is a resistor-capacitor (RC) circuit, representing a charge transfer resistance R_{ct} in parallel with a double-layer capacitance C_{dl}, both in series with a solution resistance R_s. Its impedance is:

$$Z(\omega)=R_s+1/(1/R_{ct}+j\omega C_{dl} = R_s+R_{ct}/(1+j\omega R_{ct}C_{dl})$$

At high frequencies ($\omega\to\infty$), the capacitor acts as a short circuit, and $Z\to R_s$. At low frequencies ($\omega\to 0$), the capacitor becomes open, and $Z\to R_s + R_{ct}$

To incorporate mass transport (diffusion), the Warburg impedance is introduced:

$$Z_W(\omega) = \sigma(1-j)/\omega^{1/2}$$

where σ is the Warburg coefficient. It represents the impedance due to diffusion of species toward or away from the electrode surface and appears as a 45° line in a Nyquist plot.

The full EIS response is typically plotted in:

- **Nyquist plot**: Z'' vs. Z', showing semicircles and lines
- **Bode plot**: magnitude |Z| and phase angle vs. log frequency

We use EIS to evaluate the interfacial properties and resistance of the half-cells before and after the Linear Sweep Voltammetry (LSV) tests. This technique provides

insight into the SEI layer formation and charge transfer processes by simulating the experimental data using an equivalent circuit model (EECM) that we assumed. Figure 30 shows the EIS result of all half-cell before and after LSV test, simulations based on the EECM provided in Figure 31, yielded the SEI impedance and charge transfer resistance for each half-cell (as shown in Figure 31 and Table 5). After cycling, the anode half-cell using PVDF as a binder has a R_{SEI} of only 1.099 Ω and R_{ct} 103.8 Ω, much higher than PDADMAFSI's 13.31 Ω and PDADMATFSI's 16.93 Ω. The half-cell using PEVIFSI as an anode binder showed a R_{SEI} of up to 13.07 Ω and an R_{ct} of 1633 Ω, while the anode half-cells using PDADMAFSI and PDADMATFSI as binders had moderate R_{SEI}. These results are consistent with the indicated results in the CV test.

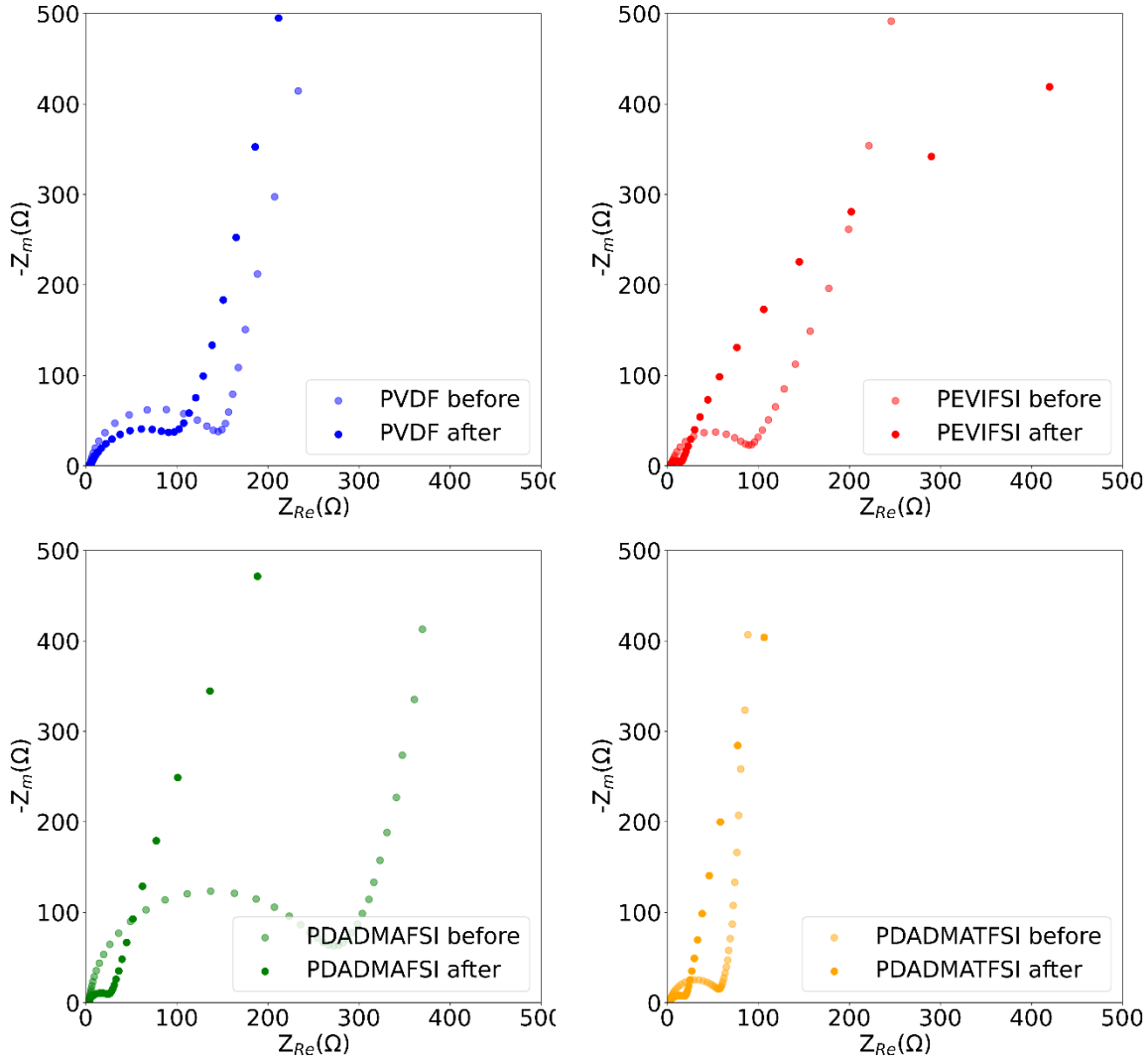

Figure 30. Nyquist plot of anodic half-cells with PVDF (blue), PEVIFSI (red), PDADMAFSI (green) and PDADMATFSI (orange) before and after cycling.

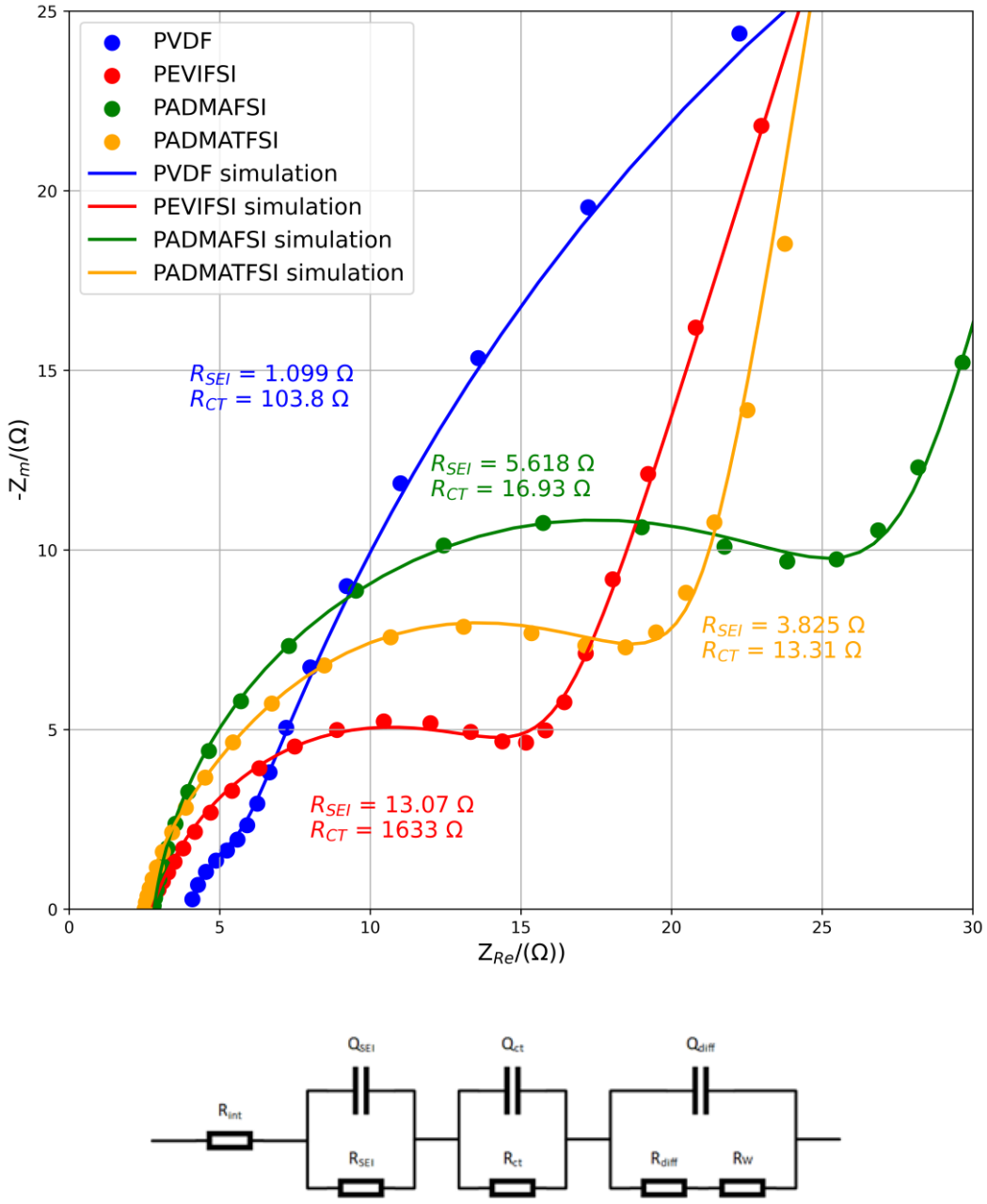

Figure 31. Nyquist plots of anodic half-cells with PVDF, PEVIFSI, PDADMAFSI, PDADMATFSI after cycling and Equivalent Circuit model used for simulation.

Dynamic Electrochemical Impedance Spectroscopy (DEIS) is an advanced electrochemical technique that extends classical Electrochemical Impedance Spectroscopy (EIS) to systems that are evolving in time. While traditional EIS assumes that the system is in a steady state during the entire measurement, DEIS enables the real-time tracking of time-dependent processes, such as degradation, adsorption, film formation, or redox reactions under non-stationary conditions. This is achieved by superimposing a multi-sine AC signal onto a time-varying DC potential (or current) and continuously monitoring the system's impedance as a function of time.

In DEIS, the applied potential can be described as:

$$E(t) = E_{DC}(t) + \sum_{k=1}^{N} \Delta E_k \sin(\omega_k t + \phi_k)$$

where $E_{DC}(t)$ is a slowly varying or modulated DC potential, and the summation represents the multi-sine AC perturbation composed of several sinusoidal components of different frequencies ω_k, amplitudes ΔE_k, and phases ϕ_k . The use of a broadband excitation allows for simultaneous probing of impedance at multiple frequencies.

The resulting current response $I(t)$ is processed using a time-resolved Fourier transform (TRFT) or sliding-window FFT, which enables extraction of instantaneous impedance values $Z(\omega,t)$. Thus, the impedance becomes a function of both frequency and time:

$$Z(\omega,t)=E(\omega,t)/I(\omega,t)$$

Mathematically, DEIS can be viewed as a non-stationary linear systems problem, where the impedance function is treated as a time-varying transfer function. To ensure accurate time-frequency resolution, the design of the excitation signal (orthogonality, frequency spacing, phase structure) and the signal-processing algorithm are critical.

The major advantage of DEIS is that it enables quasi-continuous monitoring of impedance changes in dynamic systems without interrupting or stopping the ongoing process, making it particularly valuable in studying electrocatalysis, corrosion under bias, battery charging/discharging, or sensor response during operation.

DEIS is used to investigate the impedance evolution of the electrode interface across various states of charge (SOC). By fitting the obtained impedance data to an equivalent circuit model (EECM), the impedance values of various processes can be separated, estimated, and understood. This process involves measuring the variable frequency response of an AC signal superimposed on a DC signal. DEIS measurements were performed on the half-cell after the overpotential test. Figure 32 shows the DEIS result of the half-cell using PILs and PVDF as binders during discharge (sodiation) cycle at various potentials. The obtained impedance data were fitted to the EECM, and the impedance values of various processes were obtained. Table 6-9 shows the SEI resistance (R_{SEI}), charge transfer resistance (R_{CT}), and diffusion resistance (R_{DIFF}) of PVDF, PEVIFSI, PDADMAFSI, and PDADMATFSI as binders. The R_{CT} value of PDADMATFSI is lower at all potentials compared to the other three binders. The significant reduction in R_{CT} can be attributed to the PDADMA

cation/ClO_4 interaction at the electrode interface, which helps the desolvation of sodium salt. It turns out that the ability of PILs to interact with anions is responsable for their strong performance.

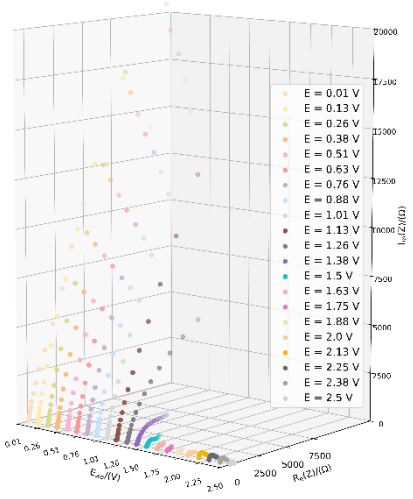

PVDF

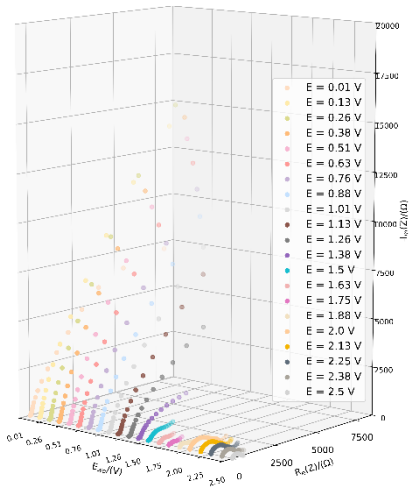

PEVIFSI

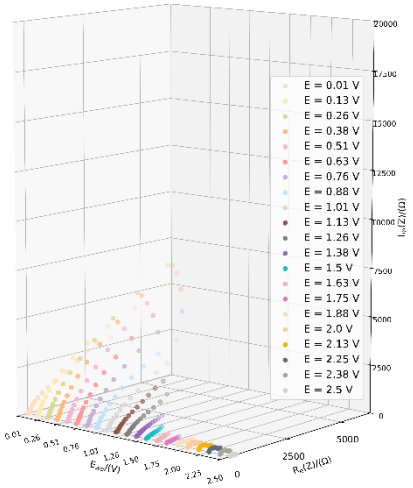

PDADMAFSI

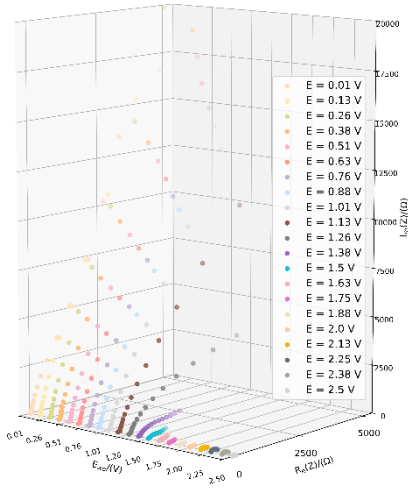

PDADMATFSI

Figure 32. DEIS profiles for the discharging cycle for PVDF, PEVIFSI, PDADMAFSI, PDADMATFSI as binders for the hard carbon anode after overpotential test.

Table 5. EIS circuit fitting values of PVDF/HC, PEVIFSI/HC, PDADMAFSI/HC, PDADMATFSI/HC after LSV test.

	R_{INT}	R_{SEI}	R_{CT}	R_{DIFF}	W	$\chi 2$	circuit
PVDF/HC	4.097	1.099	103.8	0.918	1.801E-18	5.68E-4	R(QR)(QR)((RW)Q)
PEVIFSI/HC	2.751	13.07	1633	361.3	3.402E-	2.74-3	R(QR)(QR)((RW)Q)

					6		
PDADMAFSI/HC	3.074	5.618	16.93	9010	0.0007542	2.58E-3	R(QR)(QR)((RW)Q)
PDADMATFSI/HC	2.799	3.825	13.31	15140	1188	3.12E-3	R(QR)(QR)((RW)Q)

Table 6. DEIS circuit fitting values of PVDF/HC after sodiation.

Potential	R_{INT}	R_{SEI}	R_{CT}	R_{DIFF}	W	$\chi 2$	circuit
0.01	2.126	2.06	25.49	3586	0.000167	0.00102	RL(QR)(QR)((CR)W)
0.13	2.469	2.578	33.31	93010	0.000461	0.000131	RL(QR)(QR)((CR)W)
0.26	2.656	2.262	39.7	18120	0.000496	0.00019 8	RL(QR)(QR)((CR)W)
0.38	2.671	2.572	43.19	2139	7.89E-05	0.000239	RL(QR)(QR)((CR)W)
0.51	2.667	3.789	48.79	18540	0.000451	0.000255	RL(QR)(QR)((CR)W)
0.63	2.636	13.2	51.21	53.66	8.62E-05	0.000342	RL(QR)(QR)((QR)W)
0.76	2.47	19.7	55.31	6640	9.67E-17	0.000571	RL(QR)(QR)((QR)W)
0.88	1.956	6.87	65.84	72.84	0.000173	0.00436	RL(QR)(QR)((CR)W)
1.01	2.638	12.06	64.44	2E+19	0.000119	0.000454	RL(QR)(QR)((QR)W)
1.13	2.606	9.409	68.77	67.62	0.000172	0.00051	RL(QR)(QR)((QR)W)
1.26	2.628	11.3	69.97	5867	0.000926	0.00063	RL(QR)(QR)((QR)W)
1.38	2.642	16.55	67.89	1873	0.003559	0.00079	RL(QR)(QR)((CR)W)
1.5	2.559	5.966	551.6	2312	0.005706	0.00125	RL(QR)(QR)((CR)W)
1.63	2.581	6.603	243.7	1894	0.009537	0.000945	RL(QR)(QR)((CR)W)
1.75	1.569	1.027	74.91	146.8	0.0125	0.000914	RL(QR)(QR)((QR)W)
1.88	2.599	7.103	96	458.7	0.009036	0.000764	RL(QR)(QR)((QR)W)
2	2.652	1.742	230.8	268	0.01204	0.000665	RL(QR)(QR)((QR)W)

2.13	2.707	1.602	199.8	439	0.0338	0.00054	RL(QR)(QR)((QR)W)
2.25	2.66	1.77	194.1	424.6	0.02966	0.00041 6	RL(QR)(QR)((CR)W)
2.38	2.57	1.077	145.2	394.7	0.01991	0.00054 5	RL(QR)(QR)((QR)W)
2.5	2.489	1.101	73.32	256.7	3.58E-14	0.00050 1	RL(QR)(QR)((QR)W)

Table 7. DEIS circuit fitting values of PEVIFSI/HC after sodiation.

Potential	R_{INT}	R_{SEI}	R_{CT}	R_{DIFF}	W	$\chi 2$	circuit
0.01	1.886	6.9	21.6	9036	0.00046 8	0.00073 7	RL(QR)(QR)((QR)W)
0.13	1.89	12	25.4	36100	0.00046 6	0.00054 2	RL(QR)(QR)((CR)W)
0.26	1.614	7.098	10.8	44.85	0.00011 4	0.00070 5	RL(QR)(QR)((QR)W)
0.38	1.832	19.5	31.93	43000	0.00044	0.00038 4	RL(QR)(QR)((CR)W)
0.51	2.16	9.9	47.6	55700	0.00028 8	0.00034 4	RL(QR)(QR)((QR)W)
0.63	1.811	22.6	40.68	31300	0.00043 2	0.00041 5	RL(QR)(QR)((CR)W)
0.76	1.811	23.4	45.6	24100	0.00043	0.00044 5	RL(QR)(QR)((CR)W)
0.88	2.099	13.7	59.8	35200	0.00021 2	0.00089 3	RL(QR)(QR)((QR)W)
1.01	1.8	26.9	51.9	11100	0.00042 3	0.00043 5	RL(QR)(QR)((CR)W)
1.13	1.792	28.2	54.1	6450	0.00042 2	0.00047 6	RL(QR)(QR)((CR)W)
1.26	2.037	18.1	64.2	13500	0.00014 5	0.00065 7	RL(QR)(QR)((CR)W)
1.38	2.005	19.8	58.5	3550	0.00090 4	0.00090 2	RL(QR)(QR)((QR)W)
1.5	1.755	33.1	50.9	1450	0.00041 1	0.00101	RL(QR)(QR)((CR)W)
1.63	1.713	39.3	46.3	352	0.00038 9	0.00104	RL(QR)(QR)((QR)W)
1.75	1.774	10.1	55.6	874	0.00024 6	0.00488	RL(QR)(QR)((QR)W)
1.88	1.885	258	496	633	0.00049	0.00942	RL(QR)(QR)((CR)W

					2		)
2	1.808	133	834	1010	0.000137	0.00242	RL(QR)(QR)((QR)W)
2.13	1.719	119	761	875	0.000284	0.00318	RL(QR)(QR)((QR)W)
2.25	1.657	113	677	841	3200000	0.00396	RL(QR)(QR)((QR)W)
2.38	1.876	38.1	562	630	1640000	0.00452	RL(QR)(QR)((CR)W)
2.5	2.335	10.46	165	437	0.00248	0.00134	RL(QR)(QR)((CR)W)

Table 8. DEIS circuit fitting values of PDADMAFSI/HC after sodiation.

Potential	R_{INT}	R_{SEI}	R_{CT}	R_{DIFF}	W	$\chi 2$	circuit
0.01	2.285	0.932	14.9	2480	0.00125	0.00156	RL(QR)(QR)((QR)W)
0.13	2.413	2.49	19.4	9080	0.00211	0.000286	RL(QR)(QR)((QR)W)
0.26	2.438	6.23	19.4	14600	0.00182	0.000231	RL(QR)(QR)((QR)W)
0.38	2.491	6.43	22.5	16600	0.00191	0.000214	RL(QR)(QR)((QR)W)
0.51	2.525	6.46	25.3	16400	0.00194	0.000233	RL(QR)(QR)((QR)W)
0.63	2.547	7.59	27.2	13500	0.00192	0.000239	RL(QR)(QR)((QR)W)
0.76	2.56	7.64	30.1	9770	0.00192	0.000246	RL(QR)(QR)((QR)W)
0.88	2.562	8.98	31.7	5820	0.00185	0.000262	RL(QR)(QR)((QR)W)
1.01	2.539	12.6	30.5	2890	0.00165	0.000344	RL(QR)(QR)((QR)W)
1.13	2.549	13.6	34.4	1130	0.0017	0.000318	RL(QR)(QR)((QR)W)
1.26	2.625	8.8	45.1	789	0.00246	0.000625	RL(QR)(QR)((CR)W)
1.38	2.538	9.82	36.5	856	0.00166	0.00071	RL(QR)(QR)((QR)W)
1.5	2.535	11.1	39.6	368	0.00163	0.000782	RL(QR)(QR)((QR)W)
1.63	2.639	14.1	31.2	327	0.00314	0.00106	RL(QR)(QR)((QR)W)

1.75	2.688	89.8	189	281	0.00305	0.00255	RL(QR)(QR)((QR)W)
1.88	2.583	117	254	278	0.00172	0.0014	RL(QR)(QR)((CR)W)
2	2.511	71.2	239	273	0.00144	0.00021	RL(QR)(QR)((QR)W)
2.13	2.371	1.68	119	362	0.00116	0.000497	RL(QR)(QR)((QR)W)
2.25	2.33	1.62	109	335	0.00119	0.000482	RL(QR)(QR)((QR)W)
2.38	2.48	152	269	2.9E+09	0.0019	0.00055	RL(QR)(QR)((CR)W)
2.5	2.292	1.55	49.9	191	0.00136	0.000313	RL(QR)(QR)((QR)W)

Table 9. DEIS circuit fitting values of PDADMATFSI/HC after sodiation.

Potential	R_{INT}	R_{SEI}	R_{CT}	R_{DIFF}	W	$\chi 2$	circuit
0.01	2.03	1.693	19.1	8.6E+13	0.000306	0.001	RL(QR)(QR)((CR)W)
0.13	2.466	0.0233	19.6	25	3.92E-05	0.000398	RL(QR)(QR)((CR)W)
0.26	2.088	1.9	29.4	62300	0.000612	0.000302	RL(QR)(QR)((CR)W)
0.38	1.9	2.125	33.4	21300	0.000661	0.000314	RL(QR)(QR)((CR)W)
0.51	1.88	2.135	37	183000	0.000668	0.000361	RL(QR)(QR)((CR)W)
0.63	2.24	0.0495	41.1	46.3	0.000135	0.00303	RL(QR)(QR)((CR)W)
0.76	1.85	2.154	43.2	135000	0.000703	0.000411	RL(QR)(QR)((CR)W)
0.88	1.89	2.171	45.3	123000	0.000736	0.000437	RL(QR)(QR)((CR)W)
1.01	1.94	2.187	47.2	102000	0.000771	0.00047	RL(QR)(QR)((CR)W)
1.13	2.14	2.17	49.3	40800	0.000745	0.00049	RL(QR)(QR)((CR)W)
1.26	2.345	2.52	49.9	3250	0.0011	0.000639	RL(QR)(QR)((CR)W)
1.38	2.33	2.85	46.7	1400	0.00108	0.00139	RL(QR)(QR)((CR)W)
1.5	2.395	3.65	41.7	521	0.0128	0.00243	RL(QR)(QR)((CR)W

							)
1.63	2.129	29.1	255	1680000	0.00368	0.00263	RL(QR)(QR)((CR)W)
1.75	2.319	25.9	32.3	162	0.0287	0.00117	RL(QR)(QR)((CR)W)
1.88	2.481	0.8	61.6	152	0.00831	0.00186	RL(QR)(QR)((CR)W)
2	2.393	1.07	73	112	0.00702	0.000814	RL(QR)(QR)((CR)W)
2.13	2.475	0.722	91.4	156	0.00444	0.000158	RL(QR)(QR)((CR)W)
2.25	2.473	0.773	56.5	189	0.00579	0.000147	RL(QR)(QR)((CR)W)
2.38	2.423	0.793	50.5	180	0.00659	0.00016	RL(QR)(QR)((CR)W)
2.5	1.803	1.71	43	79.3	0.000421	0.000644	RL(QR)(CR)((QR)W)

To further study the quality of the anode sheet fabricated by using different binders, the Na-ion diffusion coefficient values were calculated. Using the DEIS data in the Warburg region, the Na-ion diffusion coefficient can be calculated using the following formula

$$D_{Na^+}=\frac{R^2T^2}{2A^2n^4F^4C^2\sigma^2}$$

where R is the gas constant, T is the absolute temperature, A is the area of the electrode, n is the charge number of the electroactive species (n = 1), F is the Faraday constant, C is the concentration of sodium ions, and σ is the Warburg factor. The Warburg factor was obtained from the slope of the plots of Z' vs $\omega^{-1/2}$ (ω is the angular frequency) in the Warburg region. As shown in Figure 33, since the hard carbon anode with PVDF as a binder has a lower R_{SEI}, diffusion coefficient obtained from hard carbon anode with PVDF as a binder achieve a higher diffusion coefficient of $3.4*10^{-14}$ cm^2/s, while the hard carbon anode half-cell using PDADMATFSI as a binder is slightly inferior, achieving a diffusion coefficient of $2.8*10^{-14}$ cm^2/s. This gap is within an acceptable range.

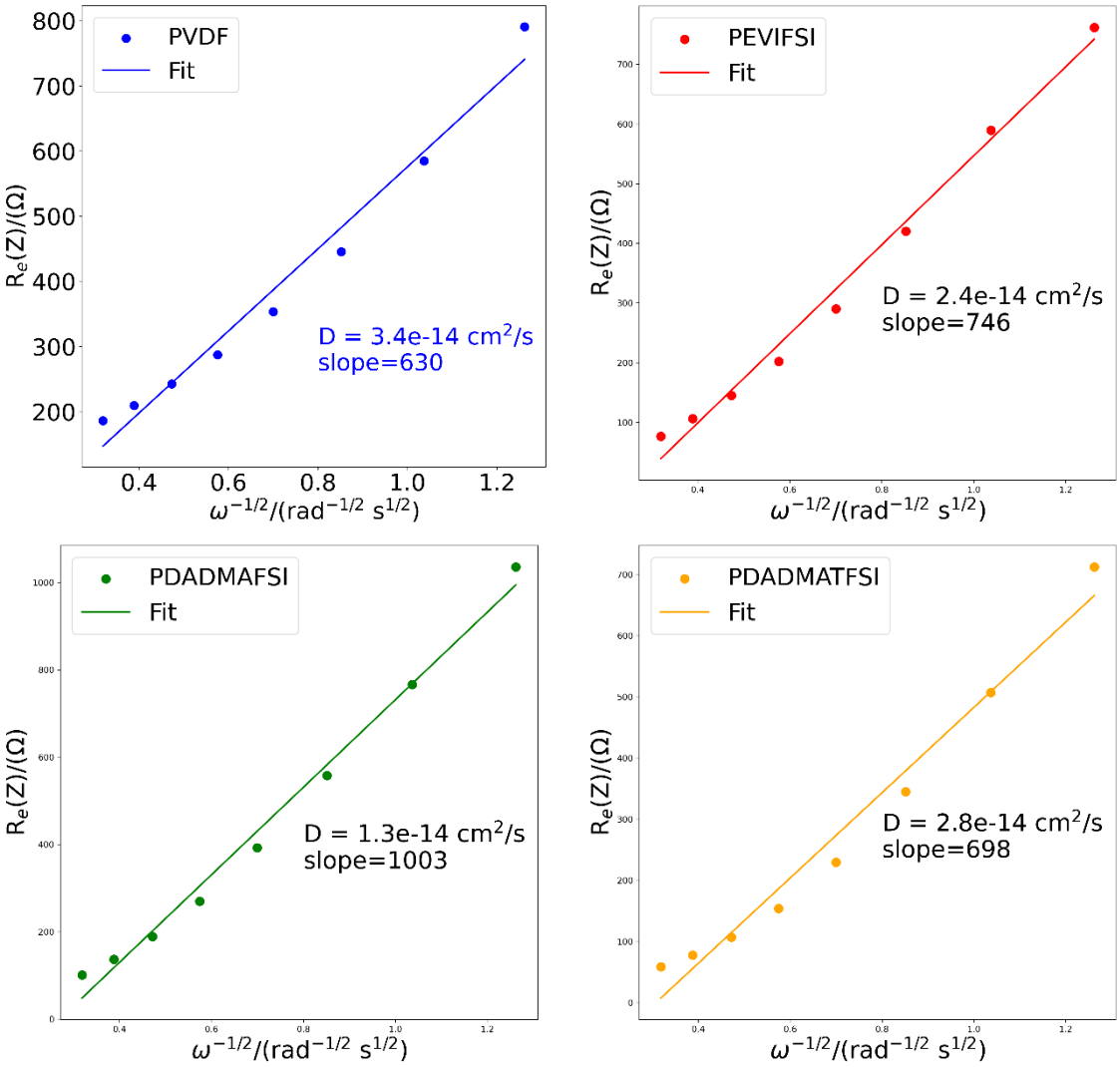

Figure 33. Nyquist plot of anodic half-cells with PVDF(blue), PEVIFSI(red), PDADMAFSI(green) and PDADMATFSI(orange) before and after cycling.

3.6 Post-mortem study

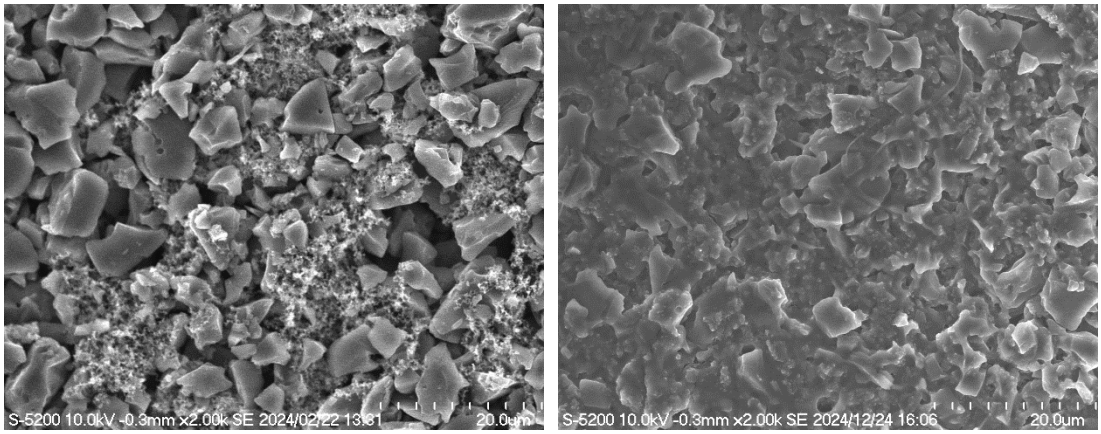

PVDF-pristine PVDF-cycled

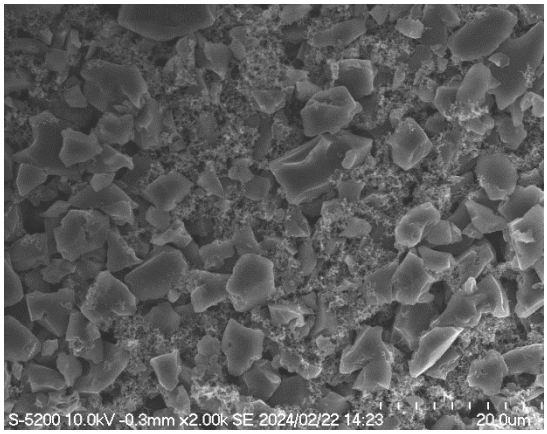

PEVIFSI-pristine

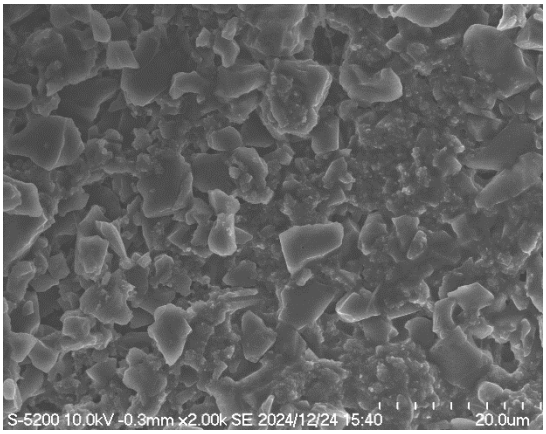

PEVIFSI-cycled

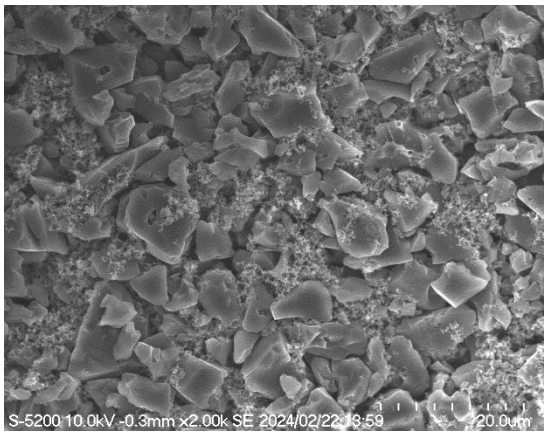

PDADMAFSI-pristine

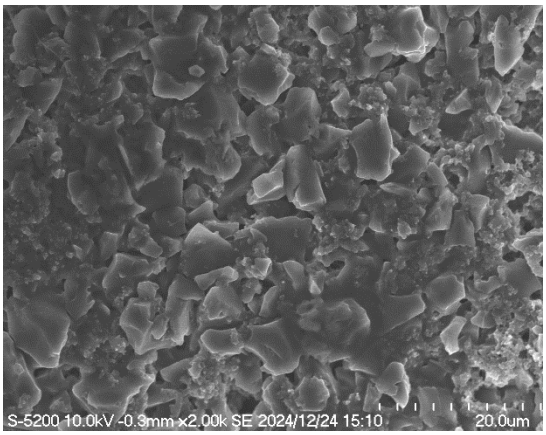

PDADMAFSI-cycled

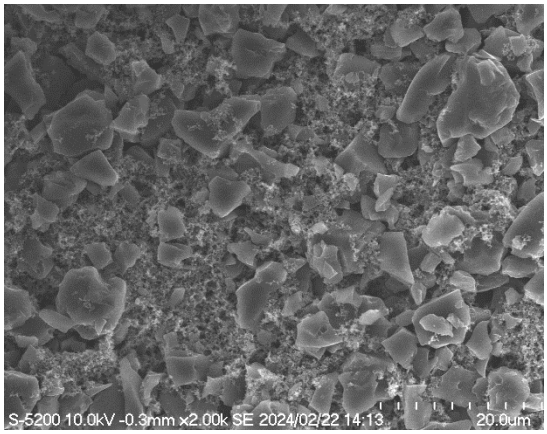

PDADMATFSI-pristine

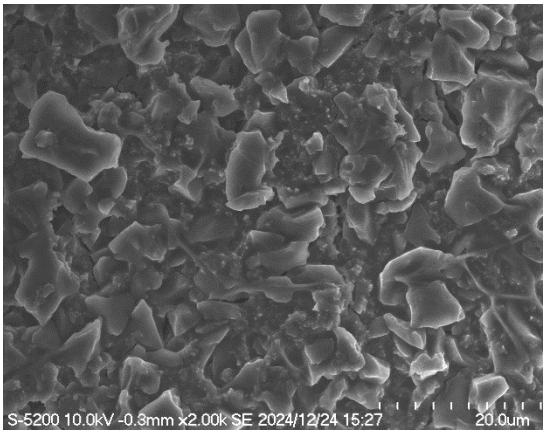

PDADMATFSI-cycled

Figure 34. SEM image of hard carbon anode surfaces before cycling and after cycling

The morphology of the anodes with PVDF, PEVIFSI, PDADMAFSI, and PDADMATFSI as binders was investigated using SEM before and after 300 charge-discharge cycles. Prior to cycling, all four electrodes exhibited a uniform distribution of active materials and conductive additives. After the cycle test, due to the continuous decomposition of the electrolyte, all electrode surfaces are adhered to the

separator. Figure 36a shows a typical area of separator residue in anode surface using PEVIFSI as a binder.

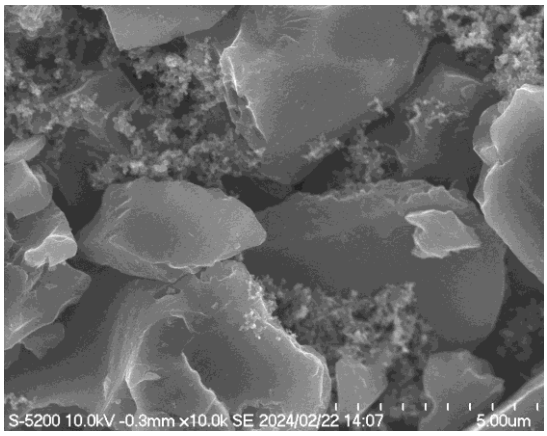

PDADMATFSI-pristine

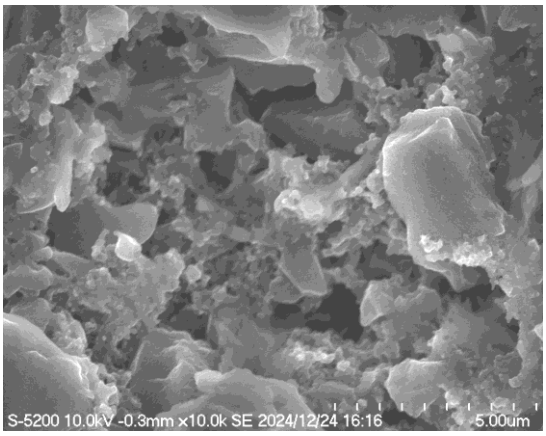

PVDF-cycled

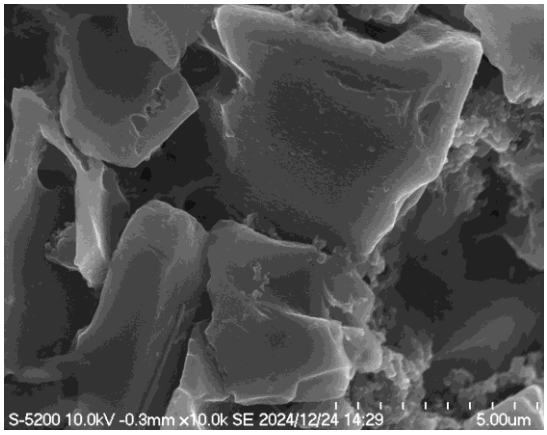

PEVIFSI-cycled

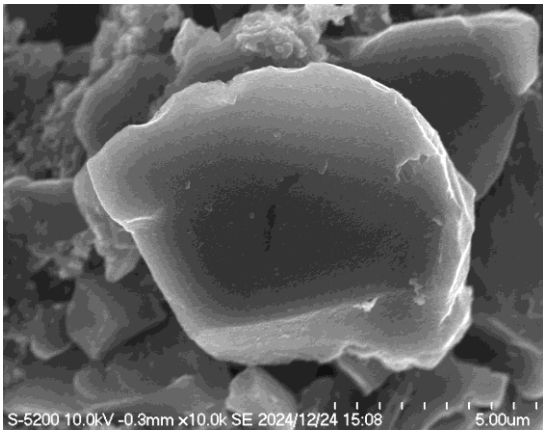

PDADMAFSI-cycled

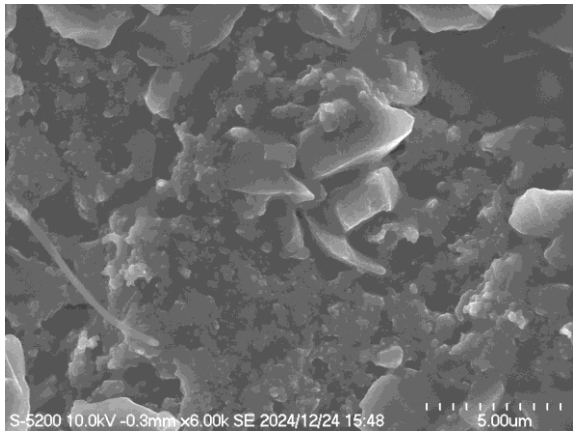

PDADMATFSI-cycled

Figure 35. SEM image of hard carbon anode surface with PDADMATFSI as binder before long cycling, a sharp surface could be observed. And hard carbon anode surface with PVDF, PEVIFSI, PDADMAFSI and PDADMATFSI as binder after long cycling, a rough surface could be observed.

As shown in Figure 34-35, a smoother surface could be observed in all electrode surface after cycling. Especially in Figure 35, Before the cycling, the sharp interface between the hard carbon particles and acetylene black could be observed. After the cycle, a smoother interface is formed, possibly due to the decomposition of the electrolyte. This conclusion can be proved by XPS test. In figure 42, it can be observed that electrode shows a large amount of carbon-oxygen double bond ratio after cycling, which are mainly formed by carbonates formed by the degradation of EC electrolyte.

Among the four electrode surfaces, the electrode using PDADMATFSI as a binder is more uniform and smoother after cycling, which may be an important reason for its better cell performance. Based on this, it can be inferred that more uniform degradation of the electrolyte on the electrode surface is the key to maintaining cell life.

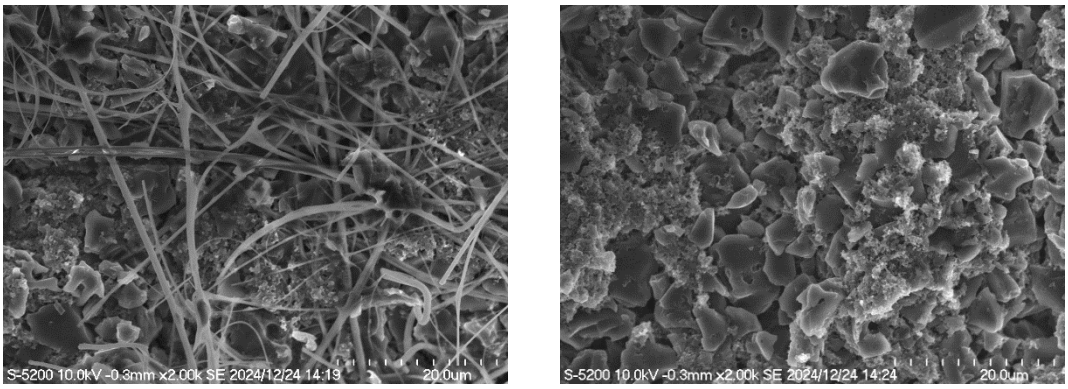

(a) (b)

Figure 36. SEM image of (a)hard carbon anode surface with PEVIFSI as binder after long cycling, a lot of glass fiber separator residue can be seen on the electrode surface. (b) hard carbon anode surface with PEVIFSI as binder after removing the glass fiber separator by using tape.

Due to the reduction and degradation of PEVIFSI itself, the anode fabricated with PEVIFSI as a binder had a lot of damage on the electrode surface during the process of removing the separator from anode sheet. Figure 36b shows a typical area after the separator is removed, and the crack on the electrode surface can be seen after the SEI in the surface is destroyed. The elemental composition of the electrode surface was further analyzed by EDX. Since fluorine exists only in the binder and chlorine exists only in the ClO_4^- anion of the electrolyte, both are selected as markers for the binder and the electrolyte. Figure 37-40 and Table 10-13 shows the element content on the anode surface before and after cycling. After 300 long cycle tests, the anode using PILs as a binder underwent ion exchange. FSI- and TFSI- anion were replaced by ClO_4^- anion which is originating from sodium salt. Because of ion exchange, fluorine

content is below detectable limit of the instrument. Instead, a higher chlorine content was observed in PILs binders. (4.16% for PEVIFSI, 4.42 for PDADMAFSI, 5.55 for PDADMATFSI, and 2.08% for PVDF)

Table 10. Element content on the anode surface of the half-cell assembled using PVDF as the anode binder before and after cycling.

	Pristine (%)	after cycling (%)
C	94.8	87.05
F	5.2	4.37
Cl	0	2.08
Na	0	6.5

Table 11. Element content on the anode surface of the half-cell assembled using PEVIFSI as the anode binder be-fore and after cycling.

	Pristine (%)	after cycling (%)
C	98.63	91.35
F	1.37	0
Cl	0	4.16
Na	0	4.48

Table 12. Element content on the anode surface of the half-cell assembled using PDADMAFSI as the anode binder before and after cycling.

	Pristine (%)	after cycling (%)
C	97.73	91.76
F	2.27	0
Cl	0	4.42
Na	0	3.82

Table 13. Element content on the anode surface of the half-cell assembled using

PDADMATFSI as the anode bind-er before and after cycling.

	Pristine (%)	after cycling (%)
C	98.53	90.9
F	1.37	0
Cl	0	5.55
Na	0	3.55

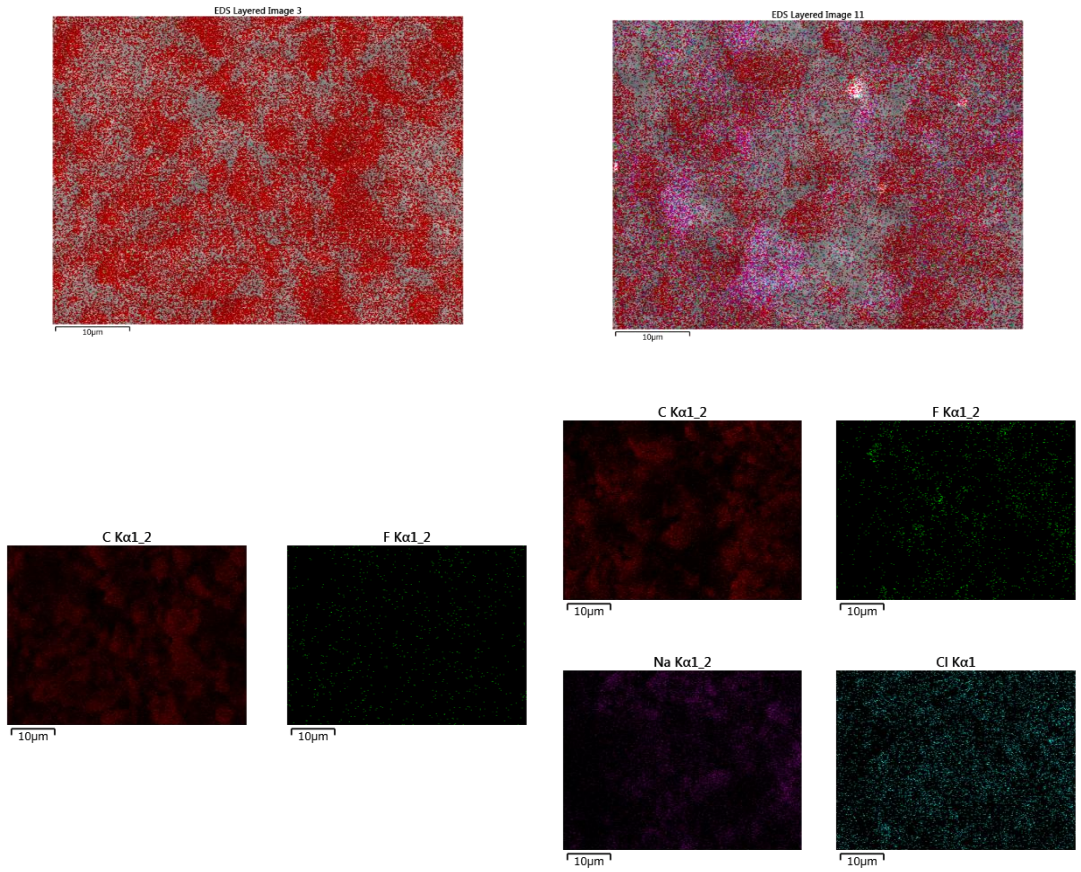

a b

Figure 37. SEM-EDS mapping for hard carbon anode with PVDF as binder (a) before and (b) after long cycling.

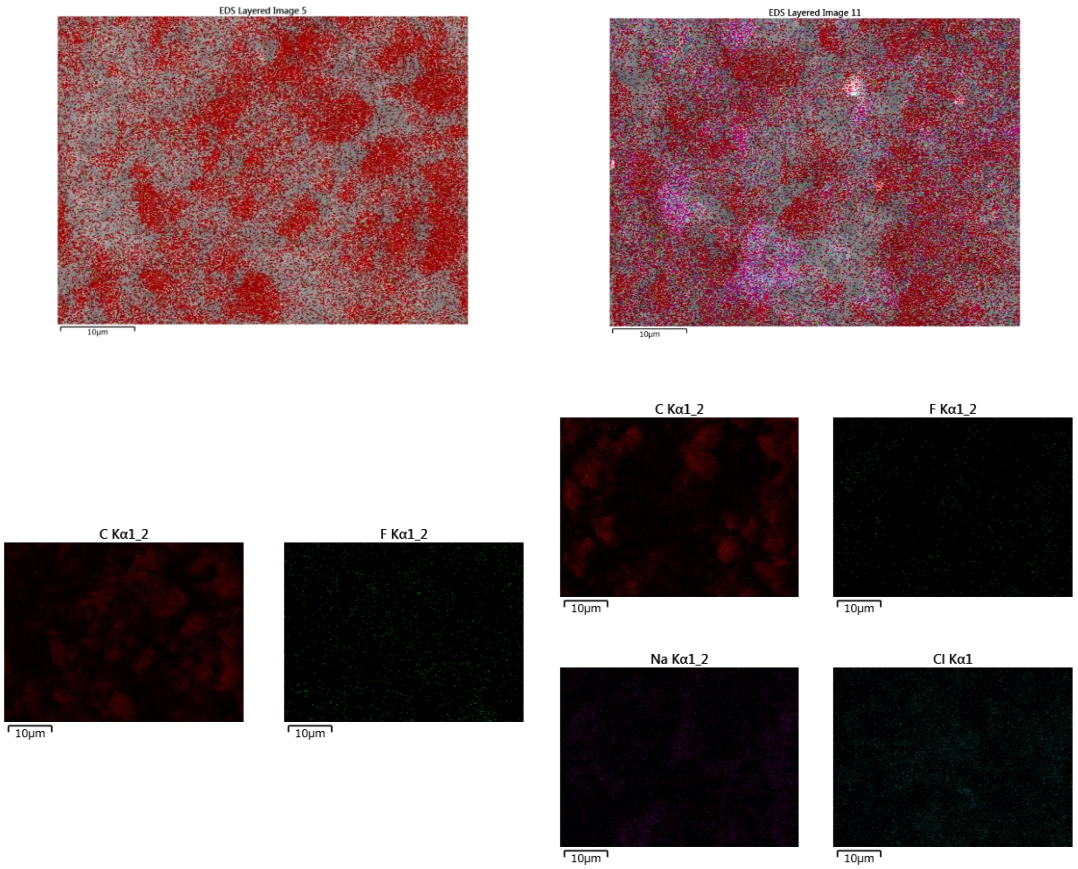

a b

Figure 38. SEM-EDS mapping for hard carbon anode with PEVIFSI as binder (a) before and (b) after long cycling.

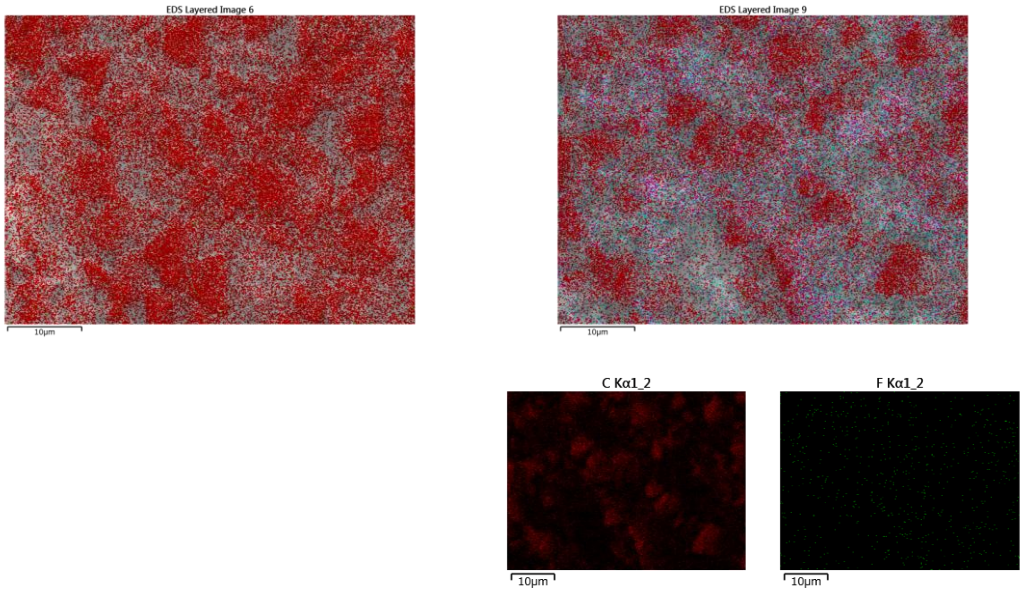

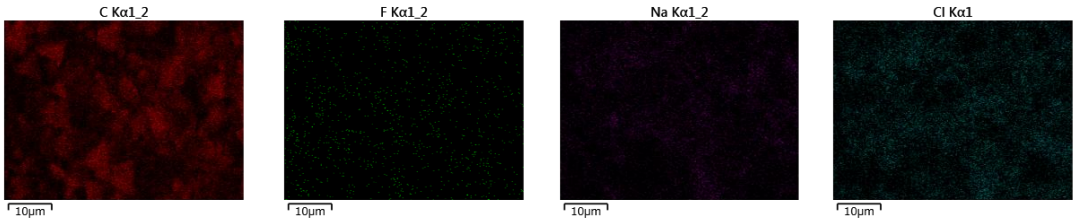

a b

Figure 39. SEM-EDS mapping for hard carbon anode with PDADMAFSI as binder (a) before and (b) after long cycling.

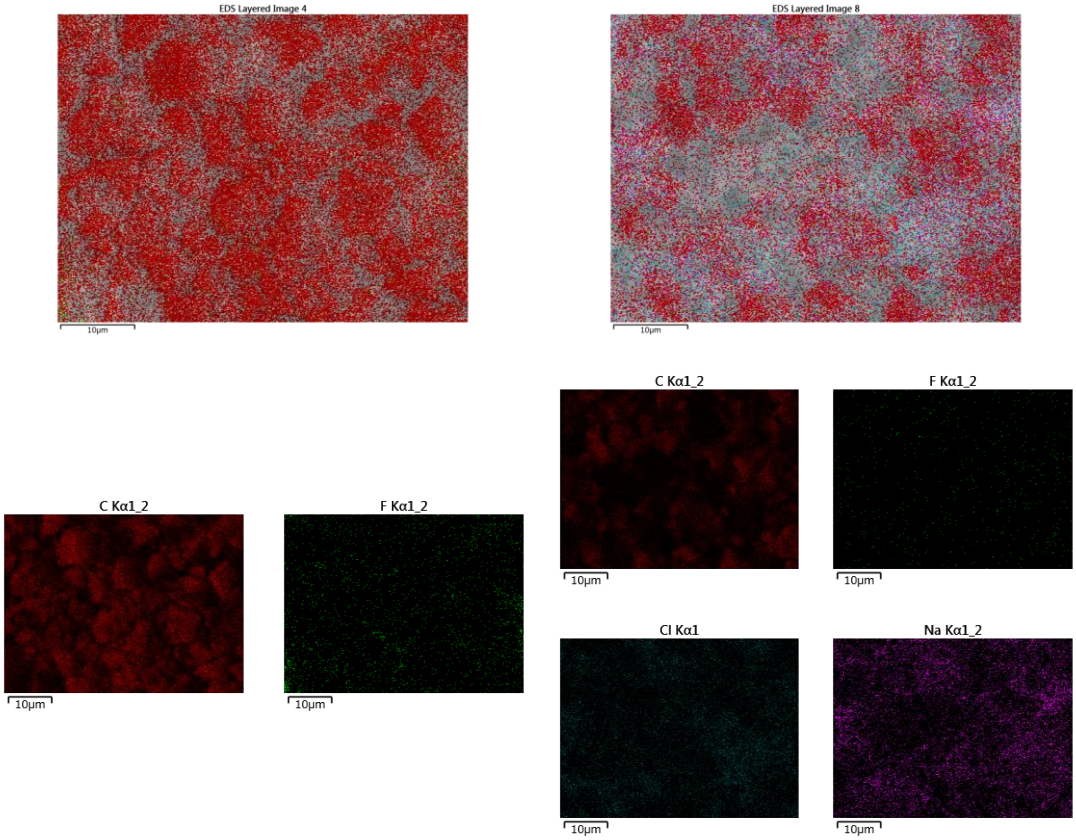

a b

Figure 40 SEM-EDS mapping for hard carbon anode with PDADMATFSI as binder (a) before and (b) after long cycling.

In order to further understand the SEI composition on the anode after cycling, we performed XPS tests on the an-ode half cells after cycling. Figure 41 shows the N_{1s} deconvoluted spectra of the anode half cells using PEVIFSI as a binder before and after the cycling test. Before cycling, it can be clearly seen that the N-C and N=C peaks

of the imidazole group appear at 396.9eV, and the N-S peak of FSI^- appears at 399.2eV. After cycling, due to ion exchange and degradation of the imidazole group, the original two nitrogen peaks are greatly weakened and covered by noise, indicating that the degradation of PEVIFSI is the main cause of the violent fluctuations in the half cell capacity. In addition, Figure 42 shows the chlorine 2p deconvoluted spectra of half cells fabricated by using PDADMAFSI and PDADMATFSI after cycling tests. Results show that the chlorine element in the electrode using PDADMAFSI as the anode binder exists mainly in the form of ClO_4^- after the cycling test, while the chlorine element in the electrode using PDADMATFSI as the anode binder exists mainly in the form of PDADMAC and NaCl after the cycling test. Figure 43 shows the C_{1s} deconvoluted spectra of the XPS test and Table 14-17 shows the peak position and ratio of the area of the C=O bond to the total area of the carbon peak after the cycling test. Anodic half cells using PDADMATFSI as a binder contains less C=O components, indicating that it generates a thinner Na_2CO_3 based SEI layer, which indicates that the SEI component composed of NaCl and PDADMAC significantly reduces the reduction of the electrolyte and helps to generate a thinner SEI layer. This explained why anodic half cells using PDADMATFSI as a binder could achieve better performance.

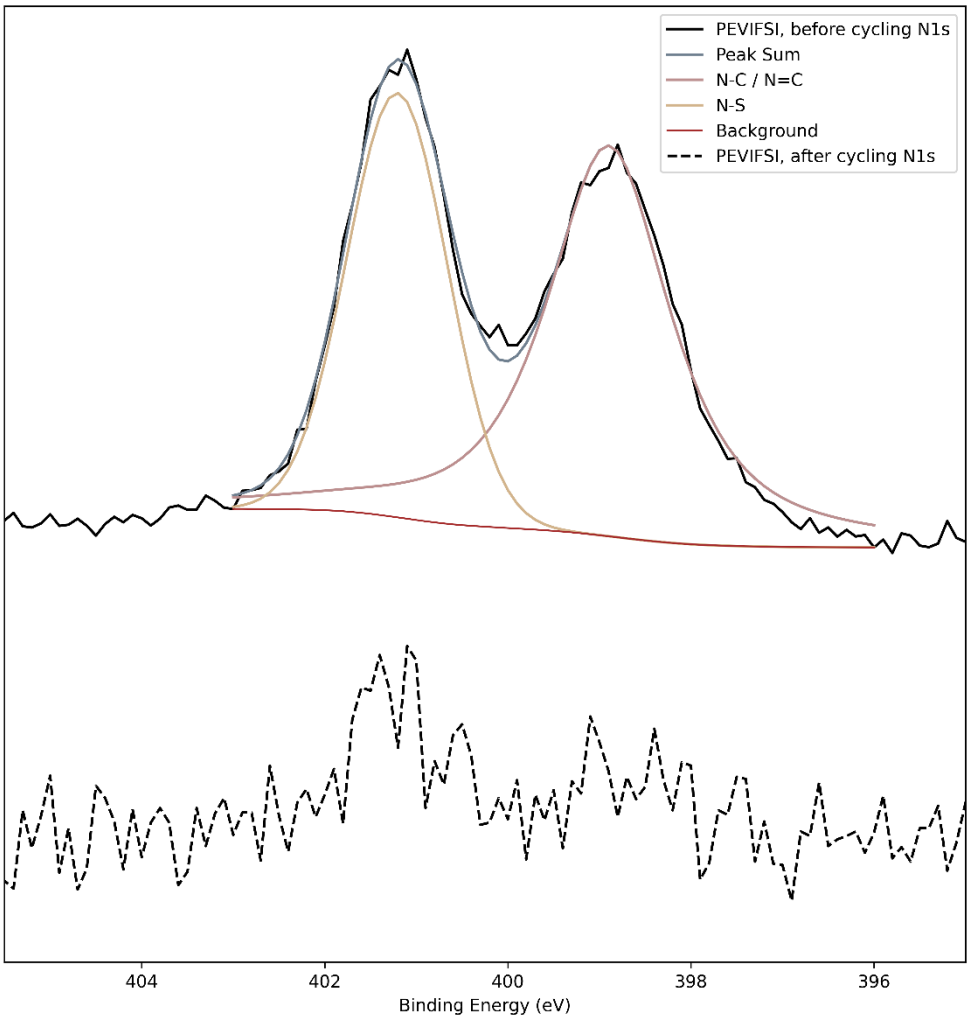

Figure 41 The deconvoluted XPS N_{1s} spectra for PEVIFSI based hard carbon anodes before and after cycling respectively explaining various components of SEI.

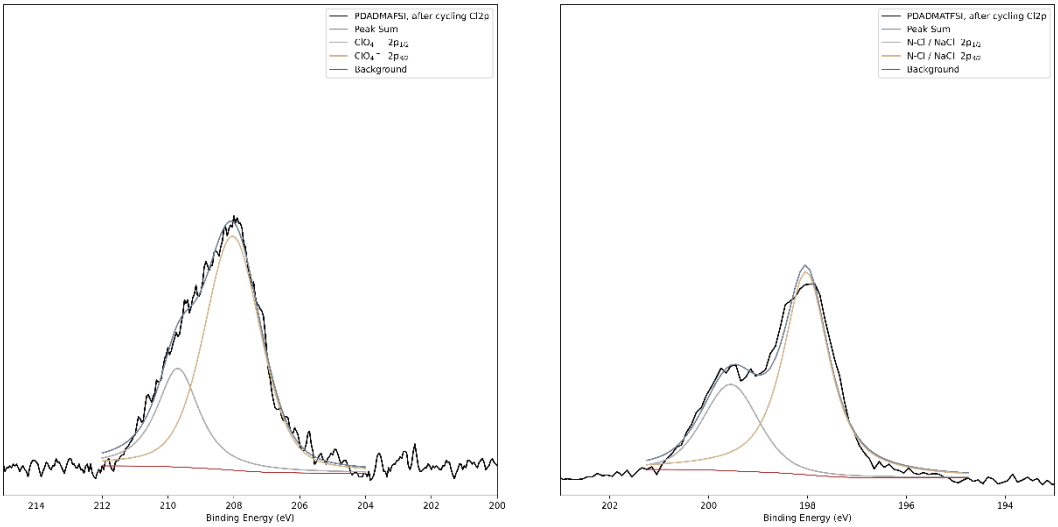

PDADMAFSI Cl_{2p}, after cycling PDADMATFSI Cl_{2p}, after cycling

Figure 42. The deconvoluted XPS Cl_{2p} spectra for PDADMAFSI and PDADMATFSI

based hard carbon anodes after cycling respectively.

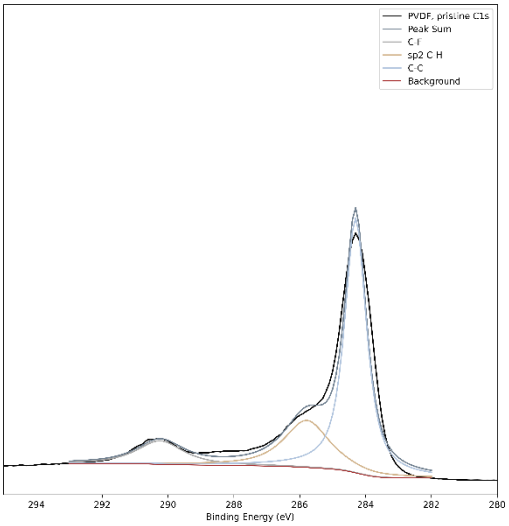

PVDF C_{1s}, pristine

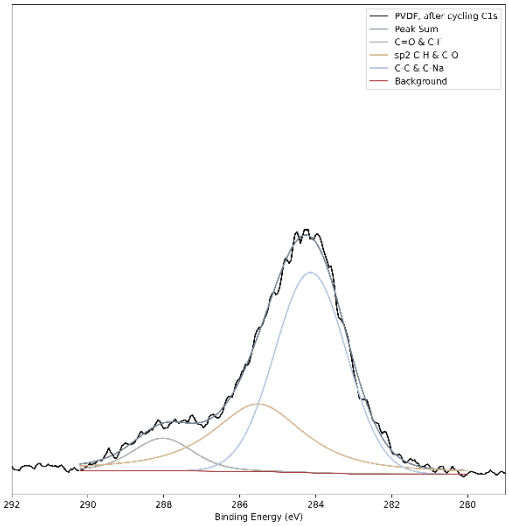

PVDF C_{1s}, after cycling

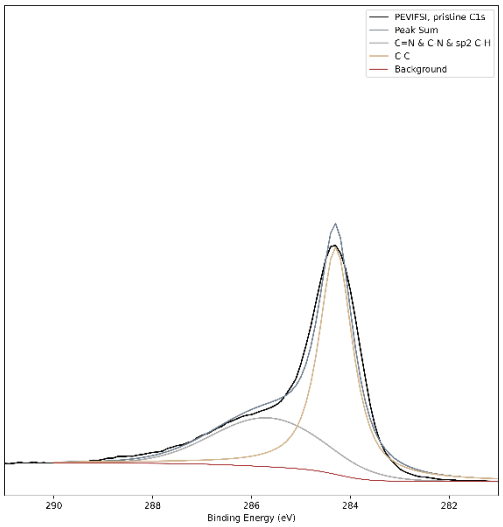

PEVIFSI C_{1s}, pristine

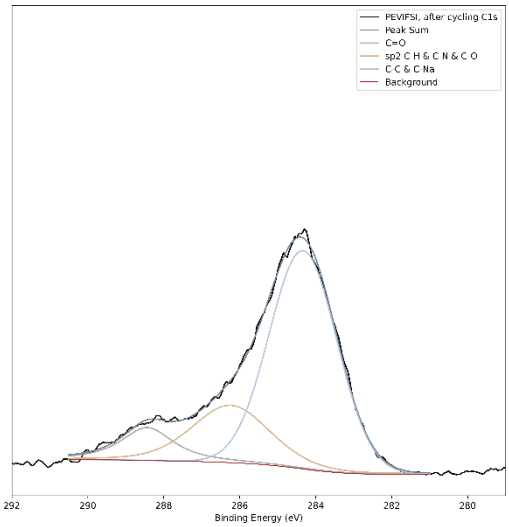

PEVIFSI C_{1s}, after cycling

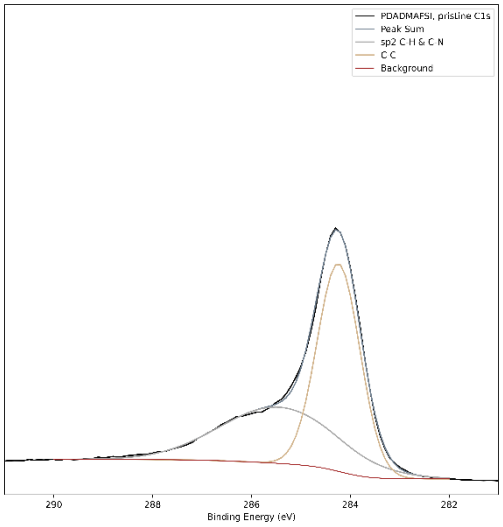

PDADMAFSI C_{1s}, pristine

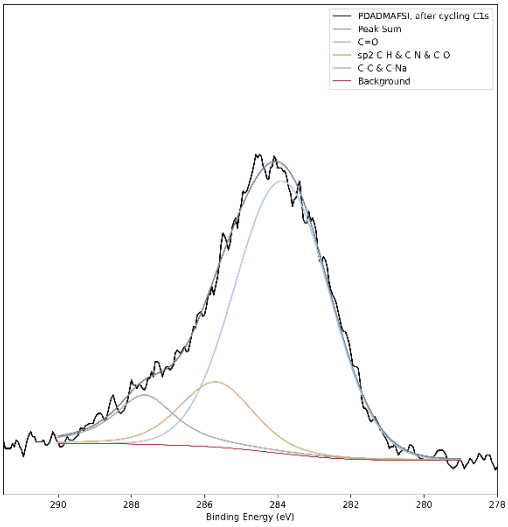

PDADMAFSI C_{1s}, after cycling

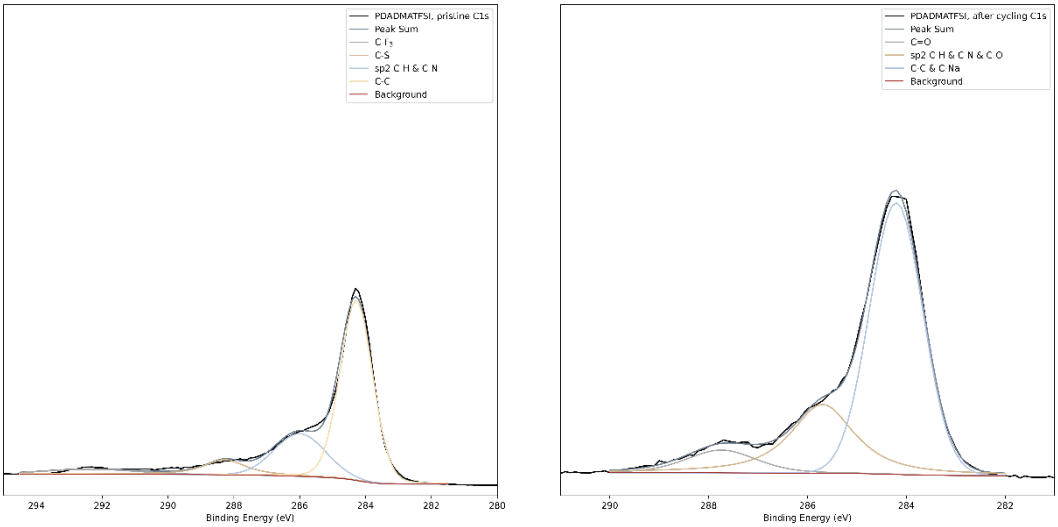

PDADMATFSI C_{1s}, pristine PDADMATFSI C_{1s}, after cycling

Figure 43. The deconvoluted XPS C_{1s} spectra for PVDF, PEVIFSI, PDADMAFSI, PDADMATFSI based hard carbon anodes before and after cycling respectively.

Table 14. Bonding type, Peak position, Area and Ratio of each peak in total area for PVDF based hard carbon anodes after cycling calculated from the deconvoluted XPS C_{1s} spectra

PVDF C_{1s}, after cycling	C=O & C-F	sp2 C-H & C-N & C-O	C-C & C-Na	Total
peak	288.02	285.51	284.13	-
Area	103.29	401.06	661.76	1166.11
Ratio	8.86%	34.39%	56.75%	100%

Table 15. Bonding type, Peak position, Area and Ratio of each peak in total area for PEVIFSI based hard carbon anodes after cycling calculated from the deconvoluted XPS C_{1s} spectra

PEVIFSI C_{1s}, after cycling	C=O	sp2 C-H & C-N & C-O	C-C & C-Na	Total
peak	288.43	286.24	284.33	-
Area	209.51	441.04	1290	1940.55
Ratio	10.8%	22.73%	66.47%	100%

Table 16. Bonding type, Peak position, Area and Ratio of each peak in total area for PDADMAFSI based hard carbon anodes after cycling calculated from the deconvoluted XPS C_{1s} spectra

PDADMAFSI C_{1s}, after	C=O	sp2 C-H & C-N	C-C & C-Na	Total

cycling		& C-O		
peak	287.64	285.68	283.87	-
Area	86.89	110.99	524.01	721.89
Ratio	12.04%	15.37%	72.59%	100%

Table 17. Bonding type, Peak position, Area and Ratio of each peak in total area for PDADMATFSI based hard carbon anodes after cycling calculated from the deconvoluted XPS C_{1s} spectra

PDADMATFSI C_{1s}, after cycling	C=O	sp2 C-H & C-N & C-O	C-C & C-Na	Total
peak	287.74	285.69	284.21	-
Area	558.7	2203.54	5268.04	8030.28
Ratio	6.96%	27.44%	65.6%	100%

3.7 High loading study

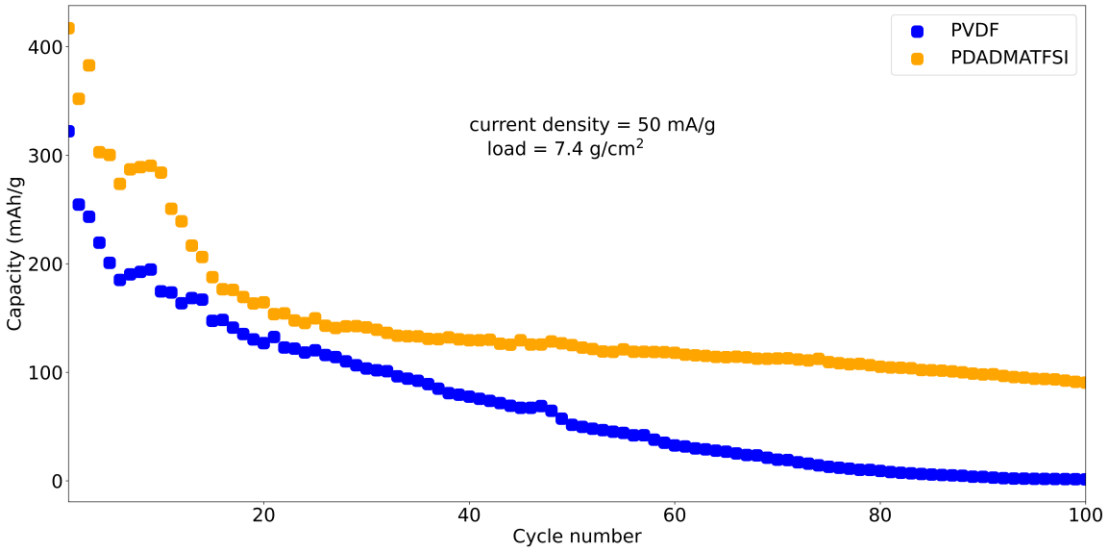

Figure 44. Long cycling performance of hard carbon anodes with PVDF(blue) and PDADMATFSI(orange) as binders with 1.0M $NaClO_4$/EC:PC electrolyte at current density of 50 mA/g. Load = 7.4 mg/cm^2.

Since the PILs binder exhibited good dispersion ability and rate performance, which indicates that it may have advantages over traditional binders at higher loads. Therefore, we tested its cycling performance at a load of 7.4 mg/cm^2. As shown in Figure 44, The anodic half-cells using PVDF and PDADMATFSI as binders showed capacities of 322.13 mAh/g and 417.17 mAh/g, respectively, in the first cycle. The capacities of both decayed rapidly during the cycle. After 100 cycles, the capacity of the

anodic half-cell using PVDF as a binder was only 1.377 mAh/g, which was almost damaged. The capacity of the anodic half-cell using PDADMATFSI as a binder was still 90.477 mAh/g. This shows the advantage of PDADMATFSI as a binder under high loads.

Chapter 4 Conclusion

As a summarization, Figure 45 shows a graphic abstract of this work. Compared with commercial PVDF polymer, pyridine-based PIL PDADMATFSI showed higher performance as a hard carbon anode binder. Its better interaction with the active material and the conductive additive in the slurry facilitates the preparation of more uniform and consistent electrode sheets, and enables the battery cell to be activated faster, thus showing higher capacity in the initial cycle. XPS test shows the ion exchange of PDADMATFSI in electrode helps forming a composite SEI layer composed of NaCl and PDADMAC on the electrode surface. This composite SEI layer prevented the decomposition of the electrolyte and formed a thinner Na_2CO_3 SEI layer on the electrode surface. Based on the results of electrochemical impedance spectroscopy and equivalent circuit model simulation, the charge transfer resistance of the half-cell using PDADMAT-FSI as the anode binder was only 12.82% of that using PVDF as the binder. This may be due to the fact that the PIL with positive charges on the main chain accelerates the desolvation of sodium ions in the electrolyte through interact with anion, making the charge transfer process faster. These characteristics cumulatively lead to improved charge and discharge performance of the PDADMAT-FSI binder. The discharge capacity of the PDADMATFSI-based half-cell was observed to be about 391.1 mAh/g at a current density of 35mA/g, and the capacity retention was 81.3% after 300 cycles. In addition, it showed higher discharge capacity than PVDF at higher current density, indicating good stability. In contrast, due to the lower LUMO, the imidazolium based PIL, PEVIFSI binder as a hard carbon anode binder underwent more intense degradation during the electrochemical reaction, with an R_{SEI} of up to 13.07Ω, far exceeding other binders. In addition, this degradation was accompanied by a large fluctuation in its capacity during the cycle test and a stronger adhesion to the separator due to degradation. All these results indicate that PDADMATFSI is a potential alternative to PVDF as a binder in SIBs and suggest that the application of imidazolium PILs in battery cells may be very limited.

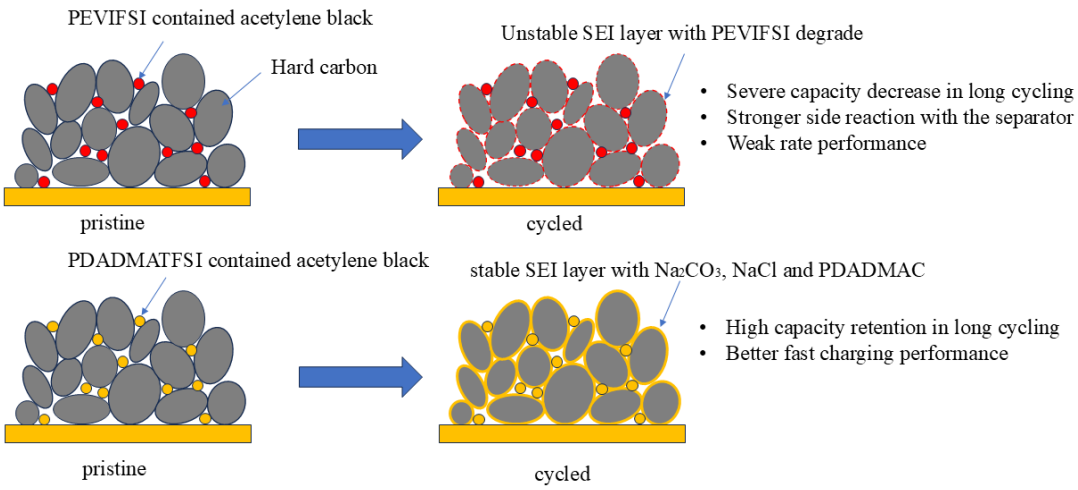

Figure 45. Graphic Abstract of this work.

REFERENCES

(1) Salkuti, S. R. Electrochemical Batteries for Smart Grid Applications. *IJECE* **2021**, *11* (3), 1849.

(2) Singh, A. N.; Islam, M.; Meena, A.; Faizan, M.; Han, D.; Bathula, C.; Hajibabaei, A.; Anand, R.; Nam, K. Unleashing the Potential of Sodium-Ion Batteries: Current State and Future Directions for Sustainable Energy Storage. *Adv Funct Materials* **2023**, *33* (46), 2304617.

(3) Zeng, X.; Peng, J.; Guo, Y.; Zhu, H.; Huang, X. Research Progress on Na3V2(PO4)3 Cathode Material of Sodium Ion Battery. *Front. Chem.* **2020**, *8*, 635.

(4) Xiao, Y.; Xiao, J.; Zhao, H.; Li, J.; Zhang, G.; Zhang, D.; Guo, X.; Gao, H.; Wang, Y.; Chen, J.; Wang, G.; Liu, H. Prussian Blue Analogues for Sodium-Ion Battery Cathodes: A Review of Mechanistic Insights, Current Challenges, and Future Pathways. *Small* **2024**, *20* (35), 2401957.

(5) Tan, S.; Yang, H.; Zhang, Z.; Xu, X.; Xu, Y.; Zhou, J.; Zhou, X.; Pan, Z.; Rao, X.; Gu, Y.; Wang, Z.; Wu, Y.; Liu, X.; Zhang, Y. The Progress of Hard Carbon as an Anode Material in Sodium-Ion Batteries. *Molecules* **2023**, *28* (7), 3134.

(6) Wu, X.; Lan, X.; Hu, R.; Yao, Y.; Yu, Y.; Zhu, M. Tin-Based Anode Materials for Stable Sodium Storage: Progress and Perspective. *Advanced Materials* **2022**, *34* (7), 2106895.

(7) Zhang, R.; Yang, X.; Zhang, D.; Qiu, H.; Fu, Q.; Na, H.; Guo, Z.; Du, F.; Chen, G.; Wei, Y. Water Soluble Styrene Butadiene Rubber and Sodium Carboxyl Methyl Cellulose Binder for ZnFe2O4 Anode Electrodes in Lithium Ion Batteries. *Journal of Power Sources* **2015**, *285*, 227–234.

(8) Chen, L.; Wu, H.; Ai, X.; Cao, Y.; Chen, Z. Toward Wide-temperature Electrolyte for Lithium–Ion Batteries. *Battery Energy* **2022**, *1* (2), 20210006.

(9) Tian, Z.; Zou, Y.; Liu, G.; Wang, Y.; Yin, J.; Ming, J.; Alshareef, H. N. Electrolyte Solvation Structure Design for Sodium Ion Batteries. *Advanced Science* **2022**, *9* (22), 2201207.

(10) Jie, Y.; Ren, X.; Cao, R.; Cai, W.; Jiao, S. Advanced Liquid Electrolytes for Rechargeable Li Metal Batteries. *Adv Funct Materials* **2020**, *30* (25), 1910777.

(11) Gao, L.; Chen, J.; Chen, Q.; Kong, X. The Chemical Evolution of Solid Electrolyte Interface in Sodium Metal Batteries. *Sci. Adv*. **2022**, *8* (6), eabm4606.

(12) Hernández, G.; Mogensen, R.; Younesi, R.; Mindemark, J. Fluorine-Free Electrolytes for Lithium and Sodium Batteries. *Batteries & Supercaps* **2022**, *5* (6), e202100373.

(13) Nayak, P. K.; Yang, L.; Brehm, W.; Adelhelm, P. From Lithium-Ion to Sodium-Ion Batteries: Advantages, Challenges, and Surprises. *Angew Chem Int Ed* **2018**, *57* (1), 102–120.

(14) Yabuuchi, N.; Kubota, K.; Dahbi, M.; Komaba, S. Research Development on Sodium-Ion Batteries. *Chem. Rev*. **2014**, *114* (23), 11636–11682.

(15) Hwang, J.-Y.; Myung, S.-T.; Sun, Y.-K. Sodium-Ion Batteries: Present and Future. *Chem. Soc. Rev*. **2017**, *46* (12), 3529–3614.

(16) Huang, Y.; Zheng, Y.; Li, X.; Adams, F.; Luo, W.; Huang, Y.; Hu, L. Electrode Materials of Sodium-Ion Batteries toward Practical Application. *ACS Energy Lett*. **2018**, *3* (7), 1604–1612.

(17) Ni, Q.; Bai, Y.; Wu, F.; Wu, C. Polyanion-Type Electrode Materials for Sodium-Ion Batteries. *Advanced Science* **2017**, *4* (3), 1600275.

(18) Wang, L. P.; Yu, L.; Wang, X.; Srinivasan, M.; Xu, Z. J. Recent Developments in Electrode Materials for Sodium-Ion Batteries. J. *Mater. Chem. A* 2**015**, *3* (18), 9353–9378.

(19) Xie, F.; Xu, Z.; Guo, Z.; Titirici, M.-M. Hard Carbons for Sodium-Ion Batteries and Beyond. *Prog. Energy* **2020**, *2* (4), 042002.

(20) Fan, X.; Kong, X.; Zhang, P.; Wang, J. Research Progress on Hard Carbon Materials in Advanced Sodium-Ion Batteries. *Energy Storage Materials* **2024**, *69*, 103386.

(21) Zeng, Y.; Yang, J.; Yang, H.; Yang, Y.; Zhao, J. Bridging Microstructure and Sodium-Ion Storage Mechanism in Hard Carbon for Sodium Ion Batteries. *ACS Energy Lett*. **2024**, *9* (3), 1184–1191.

(22) Liu, L.; Tian, Y.; Abdussalam, A.; Gilani, M. R. H. S.; Zhang, W.; Xu, G. Hard Carbons as Anodes in Sodium-Ion Batteries: Sodium Storage Mechanism and Optimization Strategies. *Molecules* **2022**, *27* (19), 6516.

(23) Zhang, W.; Dahbi, M.; Komaba, S. Polymer Binder: A Key Component in Negative Electrodes for High-Energy Na-Ion Batteries. *Current Opinion in Chemical Engineering* **2016**, *13*, 36–44.

(24) Zou, F.; Manthiram, A. A Review of the Design of Advanced Binders for High-Performance Batteries. *Advanced Energy Materials* **2020**, *10* (45), 2002508.

(25) Li, R.-R.; Yang, Z.; He, X.-X.; Liu, X.-H.; Zhang, H.; Gao, Y.; Qiao, Y.; Li, L.; Chou, S.-L. Binders for Sodium-Ion Batteries: Progress, Challenges and Strategies. *Chem. Commun*. **2021**, *57* (93), 12406–12416.

(26) Zhong, X.; Han, J.; Chen, L.; Liu, W.; Jiao, F.; Zhu, H.; Qin, W. Binding Mechanisms of PVDF in Lithium Ion Batteries. *Applied Surface Science* **2021**, *553*, 149564.

(27) Grillet, A. M.; Humplik, T.; Stirrup, E. K.; Roberts, S. A.; Barringer, D. A.; Snyder, C. M.; Janvrin, M. R.; Apblett, C. A. Conductivity Degradation of Polyvinylidene Fluoride Composite Binder during Cycling: Measurements and Simulations for Lithium-Ion Batteries. *J. Electrochem. Soc*. **2016**, *163* (9), A1859–A1871.

(28) Takahashi, K.; Higa, K.; Mair, S.; Chintapalli, M.; Balsara, N.; Srinivasan, V. Mechanical Degradation of Graphite/PVDF Composite Electrodes: A Model-Experimental Study. *J. Electrochem. Soc*. **2016**, *163* (3), A385–A395.

(29) Song, J.; Xiao, B.; Lin, Y.; Xu, K.; Li, X. Interphases in Sodium-Ion Batteries. *Advanced Energy Materials* **2018**, *8* (17), 1703082.

(30) Mogensen, R.; Brandell, D.; Younesi, R. Solubility of the Solid Electrolyte Interphase (SEI) in Sodium Ion Batteries. *ACS Energy Lett*. **2016**, *1* (6), 1173–1178.

(31) Dahbi, M.; Nakano, T.; Yabuuchi, N.; Ishikawa, T.; Kubota, K.; Fukunishi, M.; Shibahara, S.; Son, J.-Y.; Cui, Y.-T.; Oji, H.; Komaba, S. Sodium Carboxymethyl Cellulose as a Potential Binder for Hard-Carbon Negative Electrodes in Sodium-Ion Batteries. *Electrochemistry Communications* **2014**, *44*, 66–69.

(32) Dugas, R.; Ponrouch, A.; Gachot, G.; David, R.; Palacin, M. R.; Tarascon, J. M. Na Reactivity toward Carbonate-Based Electrolytes: The Effect of FEC as Additive. *J. Electrochem. Soc*. **2016**, *163* (10), A2333–A2339.

(33) Von Zamory, J.; Bedu, M.; Fantini, S.; Passerini, S.; Paillard, E. Polymeric Ionic Liquid Nanoparticles as Binder for Composite Li-Ion Electrodes. *Journal of Power Sources* **2013**, *240*, 745–752.

(34) Jayakumar, T. P.; Badam, R.; Matsumi, N. Allylimidazolium-Based Poly(Ionic Liquid) Anodic Binder for Lithium-Ion Batteries with Enhanced Cyclability. *ACS Appl. Energy Mater*. **2020**, *3* (4), 3337–3346.

(35) Chauque, S.; Oliva, F. Y.; Cámara, O. R.; Torresi, R. M. Use of Poly[Ionic Liquid] as a Conductive Binder in Lithium Ion Batteries. *J Solid State Electrochem* **2018**, *22* (11), 3589–3596.

(36) Zhang, J.; Chen, Z.; Zhang, Y.; Dong, S.; Chen, Y.; Zhang, S. Poly(Ionic Liquid)s Containing Alkoxy Chains and Bis(Trifluoromethanesulfonyl)Imide Anions as Highly Adhesive Materials. *Advanced Materials* **2021**, *33* (30), 2100962.

(37) Lee, J.-S.; Sakaushi, K.; Antonietti, M.; Yuan, J. Poly(Ionic Liquid) Binders as Li+ Conducting Mediators for Enhanced Electrochemical Performance. *RSC Adv*. **2015**, *5* (104), 85517–85522.

(38) Santiago, A.; Robles-Fernández, A.; Soria-Fernández, A.; Lopez-Morales, J. L.; Castillo, J.; Fraile-Insagurbe, D.; Casado, N.; Armand, M.; Garcia-Suarez, E. J.; Carriazo, D. Polymeric Ionic Liquid as Binder: A Promising Strategy for Enhancing Li S Battery Performance. *Journal of Energy Storage* **2024**, *80*, 110285.

(39) John, W.; Buckley, C.; Jacobs, E. SYNTHESIS AND USE OF POLYDADMAC FOR WATER PURIFICATION.

(40) Liao, J.; Ye, Z. Quaternary Ammonium Cationic Polymer as a Superior Bifunctional Binder for Lithium–Sulfur Batteries and Effects of Counter Anion. *Electrochimica Acta* **2018**, *259*, 626–636.

(41) Yang, B.; Li, C.; Zhou, J.; Liu, J.; Zhang, Q. Pyrrolidinium-Based Ionic Liquid Electrolyte with Organic Additive and LiTFSI for High-Safety Lithium-Ion Batteries. *Electrochimica Acta* **2014**, *148*, 39–45.

(42) Pont, A.-L.; Marcilla, R.; De Meatza, I.; Grande, H.; Mecerreyes, D. Pyrrolidinium-Based Polymeric Ionic Liquids as Mechanically and Electrochemically Stable Polymer Electrolytes. *Journal of Power Sources* **2009**, *188* (2), 558–563.

(43) Asha, S.; Vijayalakshmi, K. P.; George, B. K. Pyrrolidinium-based Ionic Liquids as Electrolytes for Lithium Batteries: A Computational Study. *Int J of Quantum Chemistry* **2019**, *119* (22), e26014.

(44) Galiński, M.; Lewandowski, A.; Stępniak, I. Ionic Liquids as Electrolytes. *Electrochimica Acta* **2006**, *51* (26), 5567–5580.

(45) Kazemiabnavi, S.; Zhang, Z.; Thornton, K.; Banerjee, S. Electrochemical Stability Window of Imidazolium-Based Ionic Liquids as Electrolytes for Lithium Batteries. *J. Phys. Chem. B* **2016**, *120* (25), 5691–5702.

(46) Kim, J.-K.; Matic, A.; Ahn, J.-H.; Jacobsson, P. An Imidazolium Based Ionic Liquid Electrolyte for Lithium Batteries. *Journal of Power Sources* **2010**, *195* (22), 7639–7643.

(47) Nakamura, K.; Saiwaki, T.; Fukao, K.; Inoue, T. Viscoelastic Behavior of the Polymerized Ionic Liquid Poly(1-Ethyl-3-Vinylimidazolium Bis(Trifluoromethanesulfonylimide)). *Macromolecules* **2011**, *44* (19), 7719–7726.

(48) Vauthier, S.; Alvarez-Tirado, M.; Guzmán-González, G.; Tomé, L. C.; Cotte, S.; Castro, L.; Guéguen, A.; Mecerreyes, D.; Casado, N. High-Performance Pyrrolidinium-Based Poly(Ionic Liquid) Binders for Li-Ion and Li-Air Batteries. *Materials Today Chemistry* **2023**, *27*, 101293.

(49) Schmitz, P.; Jakelski, R.; Pyschik, M.; Jalkanen, K.; Nowak, S.; Winter, M.; Bieker, P. Decomposition of Imidazolium-Based Ionic Liquids in Contact with Lithium Metal. *ChemSusChem* **2017**, *10* (5), 876–883.